ABSTRACT

Title of dissertation: Low Temperature
                          Scanning Tunneling Microscope Development:
                          Investigations of Au(111)
                          and Ultra-slow Vortex Dynamics of NbSe$_2$

                          Jonghee Lee, Doctor of Philosophy, 2007

Dissertation directed by: Professor Ellen D. Williams
                          Department of Physics

We report the development of a scanning tunneling microscope (STM), operating at 4.2 K, high magnetic field, and ultra-high vacuum (UHV), and the measurements of Au(111) and NbSe$_2$ with/without magnetic fields. The STM showed horizontal and vertical scan-ranges of $1.0 \times 1.0 \ \mu m^2$ and 270 nm, respectively. As of now, STM measurements have been carried out in a field up to 1 T. The UHV facility for tip/sample preparation in clean environment was integrated into the STM system. The nominal pressure of $\sim 10^{-10}$ mbar in UHV chambers was achieved. However, the data of Au(111) and NbSe$_2$ were taken before installation of the UHV system. We observed the standing wave of surface state electron of Au(111) by carrying out a conductance map. We found an effective mass of surface state electron of $m^* = 0.24 m_e$, where m_e is the mass of a free electron. We also observed the motion of Au steps when the STM continued scanning. As steps moved, the patterns of herringbone reconstruction on the surface also changed in a complex way. This atomic motion probably resulted from the tip-sample interaction in a stressed film. Using

pristine NbSe$_2$, we observed the charge density wave (CDW) and superconducting states simultaneously at 4.2 K via topographic/spectroscopic measurements. The well-known 3×3 superstructure of CDW state was revealed in topography. Furthermore, we deliberately introduced two additional phases ($\sqrt{13} \times \sqrt{13}$ and amorphous) by changing a bias voltage from $1 - 100$ mV to $5 - 10$ V. This *in situ* surface modification can be used in studying the competition between superconducting and CDW states. Lastly, we show that the study of vortex dynamics on the nano-meter scale was achieved by utilizing an extremely slow decay of the magnetic field in the superconducting magnet as the driving source. The field decay rate of $\sim$ nT/s caused vortices to move at $\sim$ pm/s so that the temporal resolution of our STM was sufficient to image these slowly moving vortices. Furthermore, this vortex driving mechanism can be utilized to study vortex dynamics of various superconductors on the nano-meter scale in STM experiments.

Low Temperature Scanning Tunneling Microscope Development:
Investigations of Au(111)
and Ultra-slow Vortex Dynamics of NbSe$_2$

by

Jonghee Lee

Dissertation submitted to the Faculty of the Graduate School of the
University of Maryland, College Park in partial fulfillment
of the requirements for the degree of
Doctor of Philosophy
2007

Advisory Committee:

Professor Ellen Williams, Chair
Doctor Barry Barker, Advisor
Professor Chris Lobb
Professor Fred Wellstood
Professor Steven Anlage
Doctor Danilo Romero
Professor Ichiro Takeuchi

DEDICATION

To Jungwha, my sister,

Bok-Nim Ahn, my mother, & Sangtae Lee, my father

ACKNOWLEDGMENTS

First, my thanks to my advisor, Barry Barker, who gave me a chance of building a low temperature scanning tunneling microscope system from scratch. In addition, he always guided me to think on my own, and stimulated me to explore physics independently. Without his support and supervision, I could not have accomplished what I am presenting in this Thesis.

Second, I owe much to Michael Dreyer and Hui Wang. Whenever I ran into obstacles, which seemed beyond my capability, Michael always gave me a hint to solve, or a work-around to make it easy. Indeed, without his tremendous efforts of programming softwares for the analysis of my experimental data, my work would be less polished than now. I too, am so indebted to Hui for always being with me to assist me on my experiments. Hui also helped me to savor other aspects in life, which would have been neglected without him. Moreover, when I was completely exhausted after I had taken so much data of vortex dynamics, he took over my task and continued doing more experiments on my behalf. It was he that finally proved that the motion of vortex was caused by the decaying magnetic field.

I cannot say "thank you" too much to my committee members. Ellen, my academic advisor, has always been kind and supportive to me like my mother. I always have been inspired by Chris's critical sense in physics. Fred has been a good role model, a passionate and a hard working physicist. I wish I could assimilate

his strong passion for life as a physicist. Steven was the first person who helped me to look at our vortex dynamics data from a different perspective, a chaotic phenomenon. I do remember that Ichiro asked me a question, "Why is the density of state so asymmetric"?. This stimulated me to start to think that whatever I am measuring is not just for plotting a graph or showing a good image, but for understanding physics. Danilo always had friendly discussions of physics and life with me at the LPS. He also gave us the pristine $NbSe_2$ crystals for our experiments.

Many scientists in the Quantum computing program at the LPS always inspired and cheered me up. Marc Manheimer was always generous to me in everything. Bruce Kane is a good role model as a hard working physicist. Ben Palmer was so friendly to help me take a break. Kevin Osborn gave fruitful advices to me about my future. Keith Schwab, now at Cornell, was always happy to discuss physics with me, and gave me good tips in life as a physicist.

I also appreciate all LPS staffs in the machine shop, electronic shop, and front desk. Especially, thanks to J.B. Dottellis not only for being the only smoker buddy at the LPS but also for always making machine parts quickly for me. I also thank Ramona Cruz, Miriam Diaz, and Butch Bilger (now retired) for their kindness and invisible efforts to make the lab cozy.

During my stay (1997-2000) at the City College of New York as a graduate student, I owe much to the entire faculty and staffs in the Physics department. I would like to express thanks to Maria Tamargo, who allowed me to leave her MBE group for my adventure to Maryland. I am grateful to Timothy Boyer for having advised me during my course work at the CCNY and his concern about my leaving

TABLE OF CONTENTS

LIST OF TABLES

LIST OF FIGURES

ix

Chapter 1

Development of Low Temperature Scanning Tunneling Microscope

1.1 Introduction

The low temperature scanning tunneling microscope (LT-STM) development project at the Laboratory for Physical Sciences (LPS) was initiated near the end of the year of 2002, directed by my advisor, Dr. Barry Barker. The major goal of this project was to implement an integrated STM system that operates at low temperatures (≤ 4.2 K) in high magnetic fields (up to ~ 10 T). The samples under study should be well prepared under ultra-high vacuum (UHV) environment ($\lesssim 10^{-10}$ mbar) via annealing, sputtering, evaporating processes, *etc.* A prepared sample should be transferred to the STM at low temperatures, without being exposed to atmospheric pressure. In addition, the liquid helium holding time of the system should be maximized to make very long measurements possible.

The STM is renowned for its high spatial resolution and is used to characterize the surfaces of conducting materials down to the atomic level. In the paper announcing the development of the STM, Binnig, *et al.* directly determined the 7×7 reconstruction of Si [1]. Although not discussed in this work, one can also manipulate atoms on the surface with a STM [2]. Since STM experiments are very sensitive to the STM tip and the sample surface, UHV facilities are often used with STM systems to prepare the tip and sample in a clean environment. Recently, many

groups have explored the unsolved puzzle of high temperature superconductivity [3], atom manipulations [2, 4], and determination of the chemical contents of a sample via inelastic scattering [5] by using various LT-STM systems. Anchoring the STM at low temperature allows one to carry out very long measurements; our STM can measure a specific area repeatedly over a week. Our system also has a superconducting magnet, allowing us to vary the magnetic field.

In this chapter, I will review the principle of STM operation, the design concept we used for LT applications integrated with UHV, the procedure for getting data at LT, and the performance of LT-STM in general.

1.2   Principles of Scanning Tunneling Microscopy

1.2.1   Simple Model: One Dimensional Tunneling

Classically, a particle cannot penetrate an energy barrier unless the kinetic energy of the particle is larger than the barrier height. Quantum mechanically, an electron can penetrate into the barrier and can be found on the other side with some probability. Fig. 1.1 shows the schematic of one dimensional tunneling in a STM setup. A sample and a tip are separated by a vacuum gap, d. The work function of the sample is denoted as ϕ. In the figure, the sample is negatively biased at $-V$ with respect to the tip (*i.e.* the tip is grounded). If $V = 0$, no net tunneling current flows, because the current from the tip to the sample and that from the sample to the tip cancel each other. If $V < 0$ as in Fig. 1.1, the Fermi level at the tip is lowered by $e|V|$ with respect to the Fermi level at the sample (e is the charge of an

electron). Then the electrons at the occupied states of the sample, close to its Fermi level, tunnel through the vacuum gap, and fill up the empty states of the tip (the tunneling current flows from the tip to the sample). On the other hand, if $V > 0$, the Fermi level at the tip is raised by eV. Therefore the electrons at the occupied states of the tip tunnel through the vacuum gap, and fill up the empty states of the sample (the tunneling current flows from the sample to the tip).

When $V < 0$, the probability to find electrons of the nth state of the sample within the tip, is given by

$$P \propto |\psi_n(0)|^2 e^{-2\kappa d} , \tag{1.1}$$

where $\psi_n(0)$ is the probability amplitude at the sample surface of the nth state of the sample,

$$\kappa = \frac{\sqrt{2m\phi}}{\hbar} , \tag{1.2}$$

the decay constant of the tunneling electrons of the sample in the barrier region, and ϕ, the work function of the sample. By including all possible states of the sample between E_F and $E_F + eV$, the tunneling current is expressed as

$$I \propto \sum_{E_n=E_F+eV}^{E_F} |\psi_n(0)|^2 e^{-2\kappa d} . \tag{1.3}$$

Then let us introduce the local density of states (LDOS) of the sample,

$$\rho_S(z, E) \equiv \lim_{\epsilon \to 0} \frac{1}{\epsilon} \sum_{E_n=E-\epsilon}^{E} |\psi_n(z)|^2 . \tag{1.4}$$

3

Substituting Eq. 1.4 into Eq. 1.3, the tunneling current is expressed as

$$I \quad \propto \quad V \cdot \rho_{\mathrm{S}}(0, E_{\mathrm{F}}) \cdot e^{-2\kappa d} \qquad (1.5)$$

$$\approx \quad V \cdot \rho_{\mathrm{S}}(0, E_{\mathrm{F}}) \cdot e^{-1.025\sqrt{\phi}\cdot d} \ , \qquad (1.6)$$

where ϕ is in eV, and d, in Å. The work function of a metal is typically $\phi \approx 5$ eV. Substituting $\phi \approx 5$ eV into Eq. 1.6, the tunneling current decays by $e^{2.292} \approx 9.9$ times as the distance between the tip and the sample, d, is increased by 1 Å. This exponential sensitivity of I vs. d is the key feature of a STM to resolve the atomic corrugation of a conducting sample. However, since a tunneling gap is on the order of $1 - 10$ Å while typical floor vibration is on the order of μm/s from 0 to 1 kHz, a vibration isolation scheme is essential to achieve atomically resolved data, which I will discuss in Sec. 1.3.7.
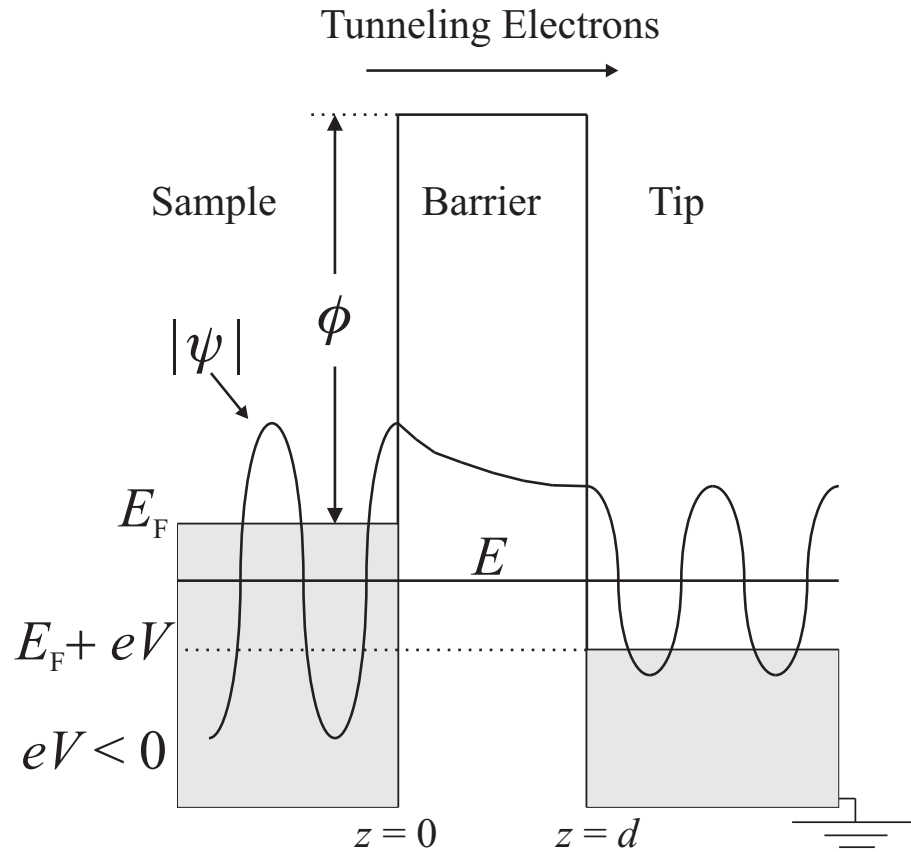
Figure 1.1: **One Dimensional Tunneling.** E_F: Fermi energy, E: energy of an tunneling electron, V: bias voltage, d: distance between the sample and the tip, ϕ: work function of the sample, ψ: wave function of a tunneling electron. Adapted from Ref. 6.

1.2.2 Operation of STM and Topography

By combining the excellent current sensitivity with a raster capability over a sample surface (XY scan) and a feedback between the tunneling current and the vacuum gap, a STM operation is realized (Fig. 1.2). A tip is mounted on a XYZ piezoelectric transducer (PZT[1]) scanner (simplified as a tripod in the figure). The XYZ PZT scanner gives three degrees of motion of the tip via voltages of V_x, V_y, and V_z. The voltages of V_x and V_y gives the horizontal motion (XY raster), and the voltage of V_z adjusts the tunneling gap (z).

First, the tunneling between the tip and the sample is achieved under a set current (I_0) and a bias voltage of V by adjusting the distance (z). While the tip scans over the surface, the feedback loop reads the error signal of $I - I_0$ and adjusts the z via V_z such that the error signal is minimized. This is called the constant current mode operation of a STM. In this mode, usually $I(x,y)$ and $z(x,y)$ are recorded ($z(x,y)$ is called topography.).

In a constant current mode, when the tip crosses over a step on the surface (A in Fig. 1.2), I increases. Therefore, the feedback loop withdraws the tip by adjusting V_z to keep I constant at I_0. If the tip passes over an inhomogeneous area with high density of states (B in Fig. 1.2), the tip also withdraws. Therefore, the tip trace (purple dashed line) reflects not only the surface geometry but also the electronic structure of the sample. Due to the finite response time of the feedback, I is not perfectly constant in a constant current mode. Therefore, in a constant

---

[1]PZT is not the acronym of piezoelectric transducer. It is the abbreviation of "lead zirconium titanate" ($\mathbf{Pb}[\mathbf{Zr}_x\mathbf{Ti}_{1-x}]O_3$, $0 < x < 1$).

current mode, complete information is achieved by topography ($z(x, y)$ or $V_z(x, y)$) together with $I(x, y)$. The drawback of this mode is that the scan-speed is limited by the feedback response time.

To overcome the feedback response time, a constant height mode can be utilized. Ideally, in this mode, V_z is fixed at a given bias voltage, and the tip scans fast over the surface with the feedback turned off. As the tip moves over the surface, I is recorded. This mode is good for studying dynamic process on atomic scale because of its fast scan-speed. However, the downside of this mode is that the tip can run into the surface, or the tunneling contact can be lost. Therefore, to achieve $I(x, y)$ in this mode, a small area with an atomically flat surface is required. In practice, this mode is usually realized by reducing the feedback and increasing the scan-speed.
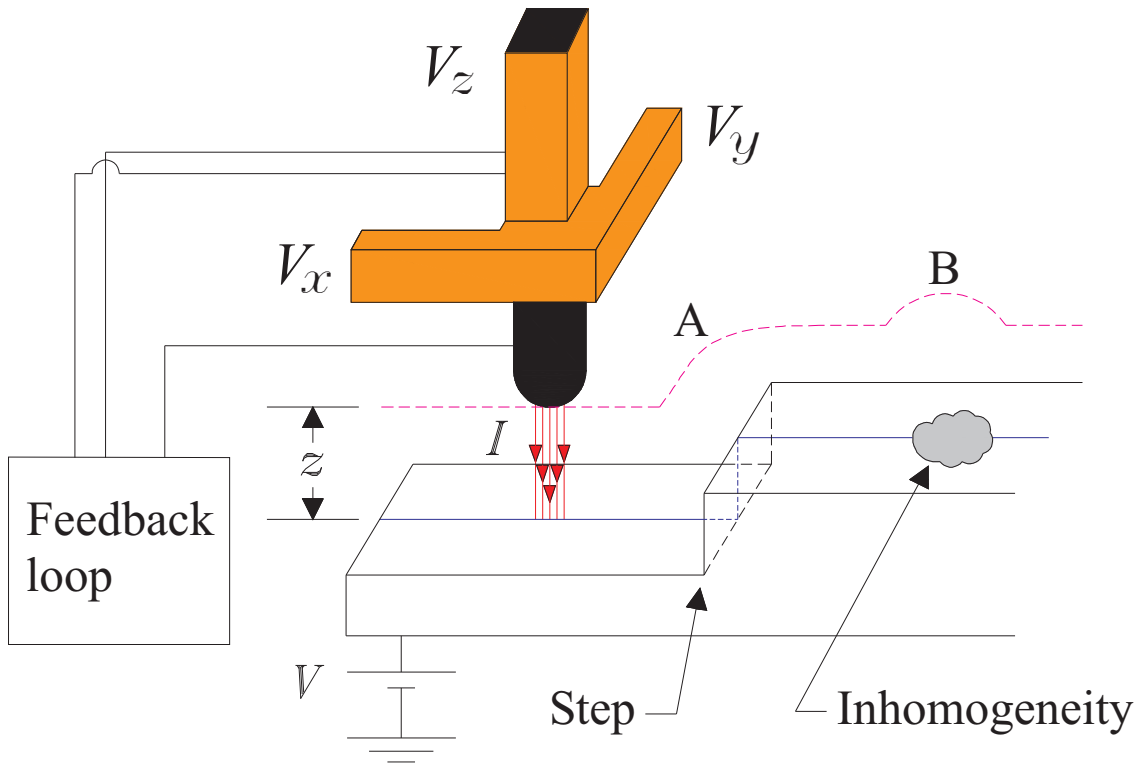
Figure 1.2: **STM Operation.** A tunneling condition is achieved by choosing a tunneling current (I_0) and a bias voltage (V) between the tip and a sample. The tip, mounted on a piezo scanner, moves over the surface of the sample, while the feedback loop tries to minimize $|I - I_0|$ by adjusting V_z. This is called a constant current mode operation of a STM. In this mode, I and V_z are recorded. Adapted from Ref. 7.

1.2.3 Scanning Tunneling Spectroscopy

In addition to topography discussed in the previous section, one can measure the LDOS of the surface of a sample with high spatial and energy resolution. The measurement of the LDOS using a STM is called scanning tunneling spectroscopy (STS). This is a very powerful feature in STM experiments, because one can study the electronic structure of superconductors, semiconductors, and conductors with high spatial and energy resolutions.

The following shows how to relate the LDOS of a sample to the experimentally measurable quantities [6,8]. At a finite temperature, the total tunneling current with a bias voltage can be expressed as

$$
\begin{aligned}
I \;=\; & \frac{4\pi e}{\hbar} \int_{-\infty}^{\infty} [f(E_{\mathrm{F}} - eV + E) - f(E_{\mathrm{F}} + E)] \\
& \times \rho_{\mathrm{S}}(E_{\mathrm{F}} - eV + E) \cdot \rho_{\mathrm{T}}(E_{\mathrm{F}} + E) \cdot |M|^2 dE,
\end{aligned}
\tag{1.7}
$$

where

$$\rho_{\mathrm{S}} \quad : \quad \text{the density of states (DOS) of the sample}$$

$$\rho_{\mathrm{T}} \quad : \quad \text{the DOS of the tip}$$

$$
f(E) \;=\; \{1 + \exp[(E - E_{\mathrm{F}})/k_{\mathrm{B}}T]\}^{-1}
\tag{1.8}
$$

$$
M_{\mu\nu} \;=\; -\frac{\hbar^2}{2m} \int_{\Sigma} (\chi_{\nu}^* \nabla \psi_{\mu} - \psi_{\mu}^* \nabla \chi_{\nu}) \cdot d\mathbf{S} \;.
\tag{1.9}
$$

The tunneling matrix element, $M_{\mu\nu}$, is a surface integral over a separation surface, Σ, between the tip and the sample. ψ is the wave function of the sample and χ is

9

that of the tip. $f(E)$ is the Fermi-Dirac (FD) distribution.

Assuming the temperature is absolute zero and the tunneling matrix element is constant, the tunneling current is proportional to the convolution of the sample DOS and the tip DOS [9]

$$I \propto \int_0^{eV} \rho_S(E_F - eV + E) \cdot \rho_T(E_F + E)dE. \tag{1.10}$$

Taking one more assumption that the tip DOS is constant, Eq. (1.10) implies

$$\frac{dI}{dV} \propto \rho_S(E_F - eV). \tag{1.11}$$

In other words, a differential conductance, dI/dV, measurement at a given bias voltage and a given location over the sample surface gives the LDOS of the sample surface, assuming the tip DOS to be constant. Otherwise, the conductance measurement shows mixed information of the tip DOS and the sample DOS, since the tunneling current is proportional to the convolution of both LDOS (Eq. (1.10)). Therefore, it is necessary to characterize and know the DOS of a tip before measuring spectroscopic data of a sample to interpret properly the LDOS of a sample. I will discuss this method in Sec. 1.3.

From an experimental point of view, the $dI/dV \approx \Delta I/\Delta V$ is realized through the following steps: first, the tip is positioned at a given location of the surface of a sample under study. Biasing the sample at V with respect to the tip (the tip is grounded), the Fermi level of the the sample is shifted by eV (Fig. 1.3). In this

figure, $V > 0$, the Fermi level of the sample is lowered by $e|V|$ with respect to that of the tip. Therefore, electrons in the occupied states of the tip tunnel to the unoccupied states of the sample at eV above the Fermi level of the sample. Adding a small ac voltage of $\Delta V = V_{\mathrm{mod}} \sin(2\pi f_{\mathrm{mod}} t)$ to V, the response of the tunneling current, ΔI, is measured by a lock-in amplifier. This response, ΔI, is proportional to the area of the LDOS of the sample at eV above the Fermi level of the sample. By extracting $\Delta I/\Delta V$ for $V > 0$, one can map out the unoccupied LDOS of the sample. If $V < 0$, $\Delta I/\Delta V$ reflects the occupied LDOS of the sample. Therefore, given a range of V, one can extract the LDOS of the sample at a given position.

One can extract the dI/dV curves over the surface, by repeating the above procedure after moving the tip from one position to next. This is called a conductance map, which enables the study of the electronic structure on the atomic scale. Carrying out a conductance map takes very long time to complete. For example, suppose that the map is going to be done over an area with 256×256 pixels, and it takes just 1 s to complete a single dI/dV curve at a given pixel. Then it takes about 18 hr to complete the entire map. Obviously, a conductance map can easily take several days with increased spatial or energy resolution. This requires very low thermal drift and long stability, which can be achieved by operating at low temperature.

Sample LDOS   Tip DOS

$E_{\mathrm{F}}\,(\,eV\,)$

$E_{\mathrm{F}} - eV\,(\,0\,)$

eV_{mod}

eV
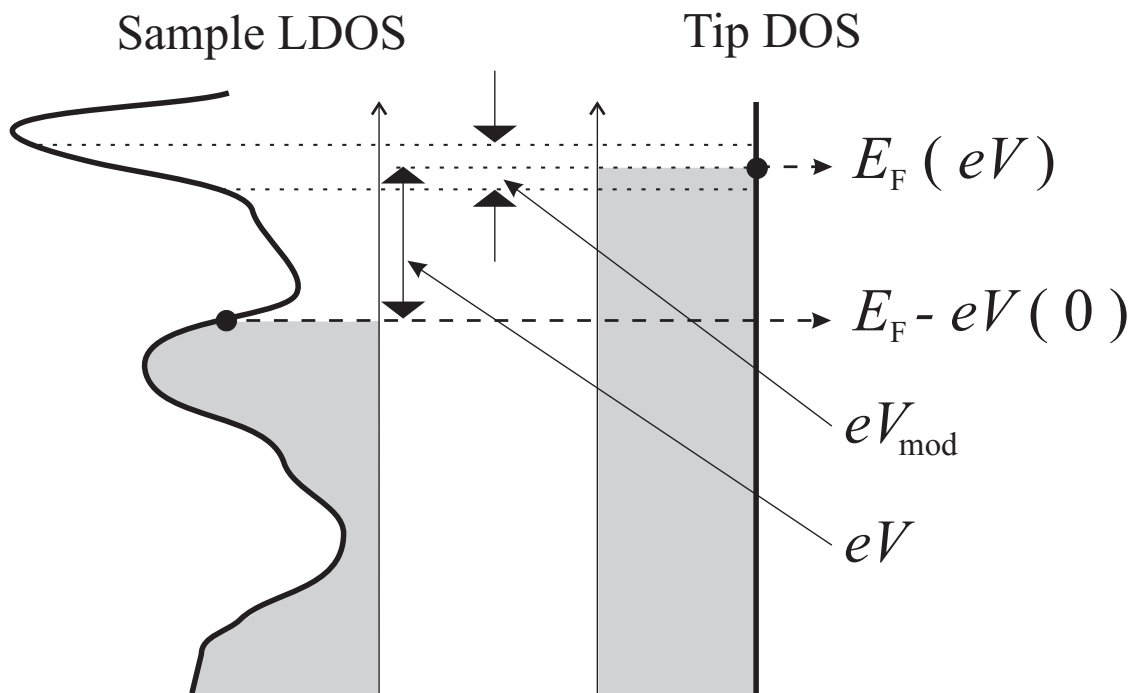
$V > 0$ with tip grounded

Figure 1.3: *dI/dV* **as local density of states.** The sample biased at a voltage, V, causes the Fermi level of the sample to be lowered by $e|V|$ with respect to that of the tip. Electrons close to the Fermi level of the tip tunnel to the unoccupied states of the sample. By adding a small *ac* voltage, V_{mod}, to V with a modulation frequency, f_{mod}, the LDOS of the sample in the unoccupied states can be measured via $\Delta I / \Delta V$, assuming that the DOS of the tip is constant. On the other hand, if the polarity of V is changed (*i.e.* $V < 0$), the LDOS of the occupied states in the sample can be measured.

1.3 Instrumentation of Low Temperature STM System

1.3.1 Design Consideration of LT-STM

Fig. 1.4a shows a computer model of the LT-STM system. The entire STM system stands on the ground floor (a-8) with a pit (a-9) for storage of the dewar. In the figure, the dewar (a-7) is lowered to the bottom of the pit. For the STM operation at LT, the dewar is raised and a sample under study is prepared in the preparation chamber (a-4). To insert the prepared sample into the STM, the sample is moved to the transfer chamber (a-3) using the horizontal transfer rod (a-2). Then it is brought to the STM (Fig. 1.4c) installed at the 4 K probe (Fig. 1.4b) using the vertical transfer rod (a-1). Since it takes several days to prepare samples under UHV, we also planned to have a storage chamber (a-5), next to the preparation chamber, dedicated for protecting prepared samples and tips in a clean environment. To isolate the environmental vibration, the whole STM system sits on top of an optical table (a-6) that is floated on four air springs when the STM operates whether at room temperature or at low temperature.
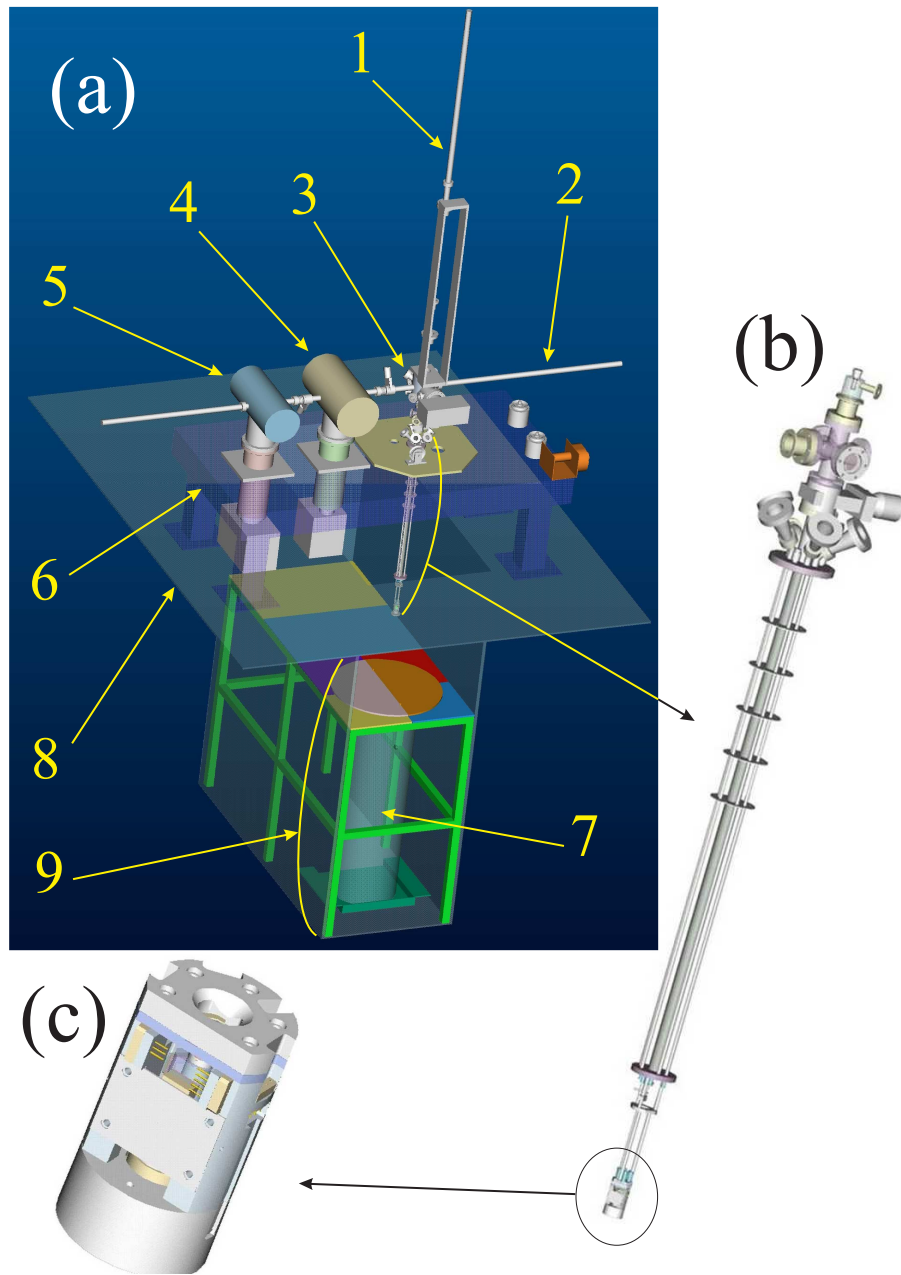
Figure 1.4: **Perspective view of a completed LT-STM system. a) LT-STM system.** 1, 2: Vertical and horizontal transfer rods respectively; 3, 4, 5: Transfer, preparation, and storage chambers respectively; 6: Optical table; 7: Dewar; 8: Ground floor, 9: Pit. **b) STM with 4 K probe. c) STM.**

1.3.2 STM Design

Currently we have two working STMs (STM I, STM II) in our group. Fig. 1.5 shows a schematic diagram (top and cross section view) of our STM and real pictures (top and front view). The overall dimension of the STM is an outer diameter of 1.5 in and a height of 2 in. The small geometry was chosen to minimize the volume to be cooled and permit insertion into a superconducting solenoid magnet. The main body (1) of the STM was machined out of one block of Macor (machinable ceramic). Having many pieces of a system can cause different thermal contractions at low temperatures. In addition, Macor was used due to its relatively good thermal conductivity at low temperatures, non-magnetic properties, and its machinability.

A ⌀ 0.25 in PZT tube scanner (2) is glued onto the scanner holder (3). This tube scanner allows a tip to move horizontally and vertically in topographic and spectroscopic modes. I will discuss the principle of the PZT tube scanner in Sec. 1.3.4. This tube scanner assembly of (2) and (3), is screwed to the sapphire prism (4). This configuration allows for different scan-ranges using a single STM body, just by choosing different sizes of PZT tube scanner in the scanner assembly.

A tip (5) sits inside the hole of a tip cup (6). The tip receptacle (7) is glued inside the PZT tube scanner. The tip cup with a tip sits in the hole of tip receptacle and is held by friction provided by three thin (~ 0.001 in) tungsten wires inside the tip cup receptacle hole. This feature will allow us to perform *in situ* tip exchange in the future. The key hole on the top plates (8) allows for *in situ* the sample exchange discussed in Sec. 1.3.1. The sample stud (9), with a sample attached (16), is locked in

place under the pressure provided by a BeCu spring plate (10) sandwiched between the two plates (8). With this configuration, the surface of a sample faces down toward to the tip. This allows to cryogenically cleave a sample.

The coarse approach mechanism of the tip toward sample, uses six stacks of shear PZT assemblies (11). Four stacks are glued down inside the STM body and two stacks are glued down on a piece of Macor, which is pressed down by a spring plate (12) at front side of the STM. Each PZT assembly consists of four plates of shear PZTs glued together and an alumina pad glued on top. The sapphire prism (4), which holds the scanner assembly, is held under the pressure of the spring plate (12).

To tell whether or not the scanner assembly is moving during the coarse approaching process, two cylindrical copper conductors (14), (15) are attached to the scanner assembly and the base (17), respectively. Thus, the capacitance change between the two conductors can also be utilized to determine the walking step size and estimate the tip-sample distance.

Figure 1.5: **Schematic and pictures of the home-built 4 K STM.** (1) Macor body, (2) tube scanner (control the motion of a tip in XYZ directions), (3) scanner holder, (4) sapphire prism, (5) tip (red), (6) tip cup, (7) tip cup receptacle, (8) top plates, (9) sample stud, (10) BeCu spring plate, (11) shear PZT stacks, (12) alumina pad (yellow), (13) front spring plate (made out of BeCu), (14) inner copper conductor, (15) outer copper conductor, (16) sample (blue), (17) base, and (18) ruby ball.

1.3.3 Coarse Approach at Low Temperatures

Nowadays there are many commercial RT-STM systems associate with UHV facilities. Also several variable temperature and LT-STM are available in the market. In most commercial LT-STM systems, a STM sits inside a UHV chamber, and the temperature of the STM typically remains at RT while a sample is cooled by cold fingers attached to a cryogen dewar. In this design, there are several benefits. First, the turn around time is very quick, because the sample-tip preparation is well controlled via optical windows and UHV manipulators. Second, the approaching time of a tip to a sample is significantly shortened, since one can see how far the tip is away from the sample via a charge-coupled device (CCD) camera during the coarse approaching process. However, this kind of design is not ideal for ≤ 4.2 K experiments, due to the heat load produced by these ancillary systems. On the other hand, a LT-STM system with our design shows better temperature performance, since the STM is directly anchored to 4.2 K. However, the coarse approach is done without being watched by an operator. Furthermore, in our system, the tip preparation is done *in situ* under less control. Currently, when a tip gets severely damaged at 4 K, we have to lower the dewar, warm up the STM to RT, and replace the damaged tip with a new one[2]. Then start cooling the system again. This process usually takes about two days in our current LT-STM system. Therefore, it is essential to implement a reliable mechanism of the coarse approach as well as a mechanism for measuring the tip-sample distance.

We chose the Pan style coarse approaching mechanism [10], which has been

---

[2]The *in situ* tip exchange of the LT-STM has not been tested at LT as of now.

known for the reliability of its approach mechanism at low temperatures. Fig. 1.6 shows the principle of this approach mechanism using four PZT stacks. In this schematic, four high voltage pulses are applied to the four shear PZT stacks respectively. Each pulse follows the previous one by $\sim 70~\mu$s. During each step, the prism is held in place because of the friction provided by three stationary stacks while one stack slips. As the four voltages decay together, all PZT stacks relax together. This synchronized relaxation makes a step toward the sample. Continuing to apply this series of voltage pulses, the tip will approach the sample, close enough to have a finite tunneling current. By changing the polarity of the voltage pulses, the reverse motion occurs.
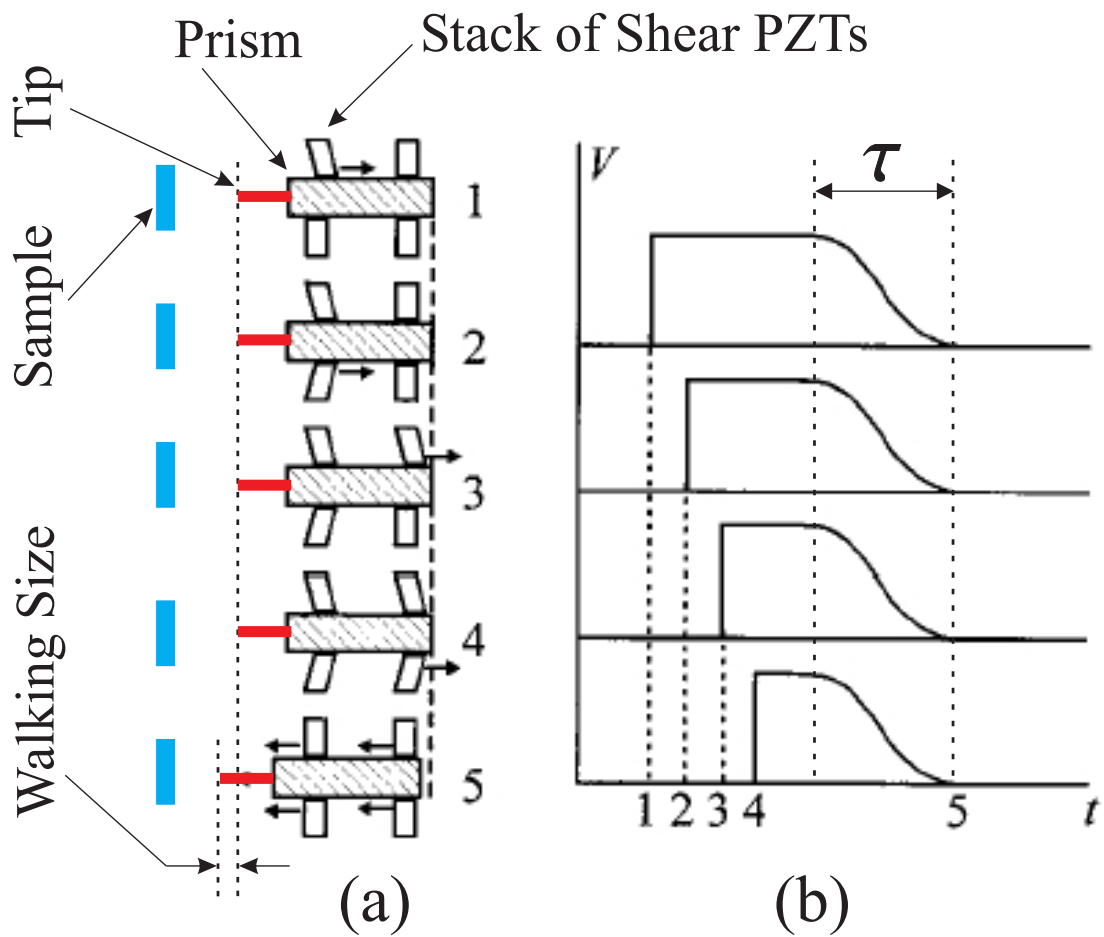
Figure 1.6: **Principle of Walker steps. a) The sequence of shear PZT stack movements. b) The sequence of voltages applied to move each stack.** The prism is actuated when all stacks of shear PZTs relax together during the time of τ. Adapted from Ref. 10.

This slip-stick mechanism not only allows for reliable coarse approach at LT, but also produces a constant walking step size regardless of the orientation of a STM with respect to gravity, in principle. Therefore, this mechanism sometime is called the non-inertial coarse approach mechanism. However, in practice, I found that the size of walking against gravity is a bit smaller than that toward it, which I will show in the end of this section.

Given a PZT shear plate $(l \times l \times h)$, the amount of shear,

$$\Delta l = d_{15} \times \frac{V}{h} \times h = d_{15} \times V \ , \tag{1.12}$$

occurs when a voltage of V is applied between the top and bottom plates, where d_{15} is the relevant piezoelectric coefficient of the shear PZT plate (Fig. 1.7a). The arrow (red) indicates the shear direction when the top is positively biased with respect to the bottom. The PZT plate used in the STM was a plate of $0.3 \times 0.3 \times 0.02$ in^2 with $d_{15} = 330 \times 10^{-12}$ m/V at RT. Substituting these numbers into Eq. 1.12 when $V = 250$ V is applied,

$$\Delta l \approx 82.5 \text{ nm at RT.} \tag{1.13}$$

This size decreases substantially, as the temperature goes down to 4 K. By increasing V, the walking step can be increased according to Eq. 1.12a. However, above a certain voltage, the PZT material will depolarize, and it will not shear. To overcome this problem and increase a step size at a given V, multiple plates of PZT can be stacked together such that the polarities of shear direction of the adjacent plates

become opposite (Fig.1.7b).

$$\Delta l_{\text{stack}} = d_{15} \times V \times n \, , \tag{1.14}$$

where n is the number of shear PZT plates. Therefore, given the same voltage V applied, the amount of shear in the stack of two plates becomes twice as large as that in Fig. 1.12. Since I used four plates in each stack in our STM,

$$\Delta l_{\text{stack}} = 4 \times \Delta l \tag{1.15}$$

$$\approx 330 \text{ nm at RT}, \tag{1.16}$$

when $V = 250$ V is applied. However, notice that this value is the ideal case without any load to be actuated by the shear motion. In reality, it is smaller than this estimated size of a walking step due to friction. If the front spring plate is too tight (friction is too high), the scanner will not move. On the other hand, if it is too loose, it does not support the weight of the scanner assembly. Therefore, the degree of tightening the front spring plate should be empirically optimized between the two extreme cases to maximize the walking step size.

To actuate the motion of the prism, where the scanner assembly is attached, a home-built walker controller was used. Because one step is completed by the six stacks of four shear PZT plates in our STM, the walker controller should produce a series of six voltage pulses. Fig. 1.8 shows a series of voltage pulses at 325 V of the LT-STM walker controller. Each following pulse is delayed by 70 μsec. As discussed

earlier, all six pulses decay together, 0.35 msec after the first pulse is applied.

After the walker assembly was finished, walking tests were carried out. Using inner and outer Cu cylinder conductors, the change of the capacitance was measured after taking steps toward (forward step) or away from (reverse step) a sample (Fig. 1.9). One can clearly see the linear behavior of both forward and reverse direction. The sizes of forward steps are

$$\left.\frac{\Delta C}{\Delta N}\right|_{\text{fwd}} = -0.22 \text{ fF/step} \tag{1.17}$$

$$\left.\frac{\Delta C}{\Delta N}\right|_{\text{rev}} = +0.28 \text{ fF/step} \tag{1.18}$$

respectively, where ΔN is the number of steps taken.

Assuming the capacitance change (ΔC) and the travel distance (Δz) are linear to each other, one can estimate the forward/reverse walking step size using Eq. 1.17 and Eq. 1.18, respectively as following.

$$
\begin{aligned}
S_{\text{fwd}} &= \left.\frac{\Delta C}{\Delta N}\right|_{\text{fwd}} \times \left(\frac{dC}{dz}\right)^{-1} \\
&= -0.22 \text{ fF/step} \times (1.07 \text{ fF/}\mu\text{m})^{-1} \approx 210 \text{ nm/step} \tag{1.19} \\
S_{\text{rev}} &= \left.\frac{\Delta C}{\Delta N}\right|_{\text{rev}} \times \left(\frac{dC}{dz}\right)^{-1} \\
&= +0.28 \text{ fF/step} \times (1.07 \text{ fF/}\mu\text{m})^{-1} \approx 260 \text{ nm/step} \tag{1.20}
\end{aligned}
$$

for $V = 250$ V at RT, where $dC/dz = 1.07$ fF/μm is calculated in Appendix A.

At 250 V, the measured walking step size in either direction is smaller than the estimated one, 330 nm (Eq. 1.16). The size of forward walking (against gravity)

is smaller by ~ 40 % than the estimated value, and that of reverse walking (toward gravity), smaller by ~ 20 %. The estimated 330 nm is based on the assumption that friction is zero when a PZT stack shears (slip) and it is infinite when the stack is stationary (stick). However, this assumption is an approximation of the real situation. In the actual slip process, there exists small friction while there exists small slipping when a PZT stack is stationary. Therefore, the walking step sizes are smaller than the estimation. In addition, the forward walking is smaller than the reverse one by ~ 20 %. The front spring plate, when it is optimally[3] pressing the scanner assembly, can sustain a weight of $400 - 500$ g ($3.9 - 4.9$ N) With this configuration, a forward walking was possible with a load of up to ~ 100 g (0.98 N) at $V = 250$ V and RT.

In addition to the RT test, I also tested walking step size at 77 and 4.2 K using the same walker voltage, 250 V (Table 1.1). From RT to 77 K, the size decreases by a factor of ~ 1.5. From RT to 4.2 K, it decreases by a factor of ~ 2.8.

Direction	RT	77 K	4.2 K
Forward	210 nm/step	150 nm/step	80 nm/step
Reverse	260 nm/step	160 nm/step	90 nm/step

Table 1.1: Walking size at RT, 77 K, and 4.2 K. A walker controller voltage of 250 V was used for all tests.

---

[3]We find the optimal condition by adjusting tightening four screws on the front spring plate such that the forward walking step size becomes $1/4 - 1/3$ of the Z scan range of the PZT tube scanner (Table. 1.2).
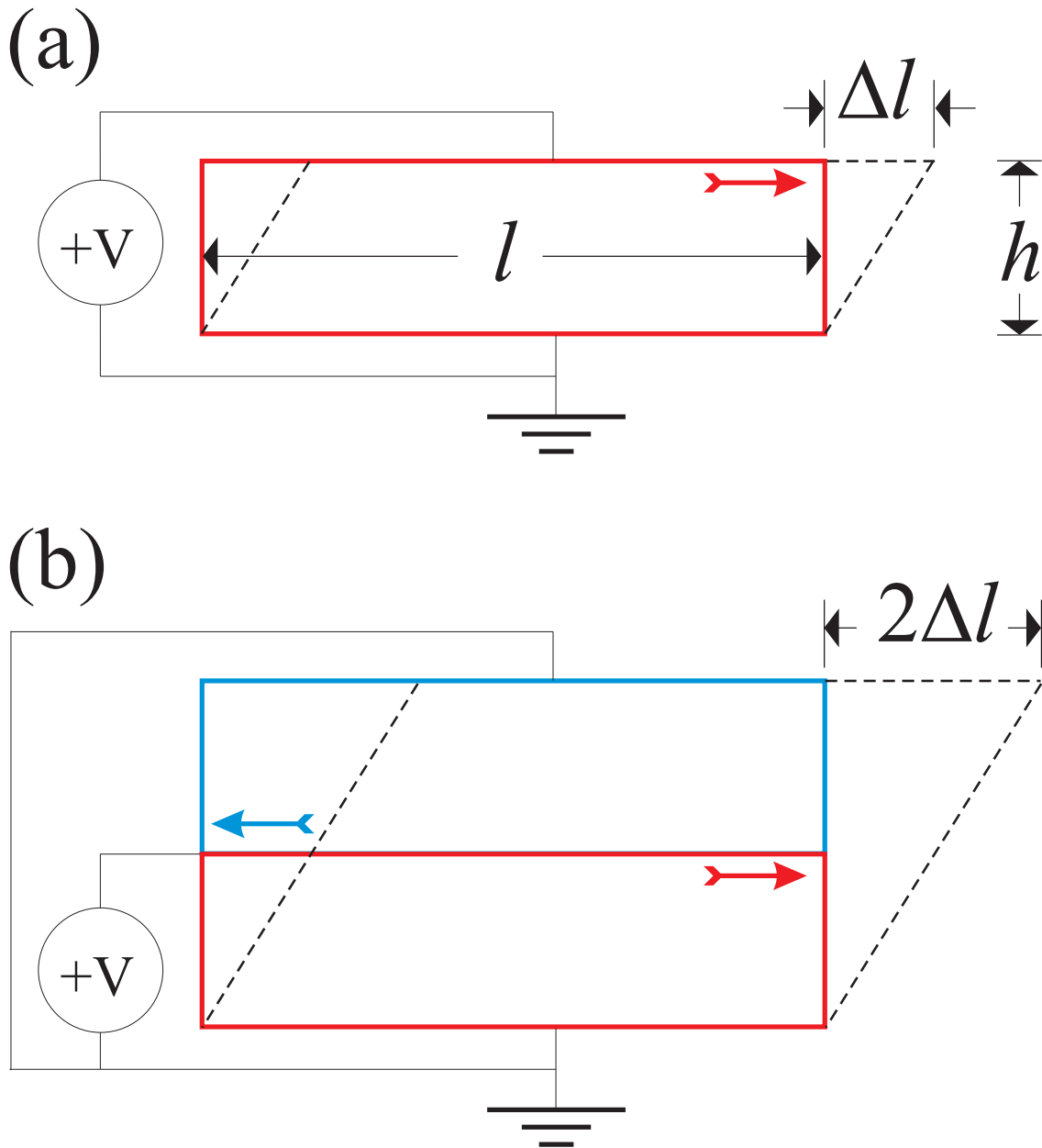
Figure 1.7: **a) Single shear PZT plate.** The arrow indicates the shear direction when $+V$ is applied to the top with respect to the bottom. Δl, l, and h are the amount of shear, length, thickness of the plate respectively. **b) A stack of two shear PZT plates.** $+V$ is applied to a stack of two PZT shear plates such that the polarities of two plates are opposite at the interface when $+V$ is applied to it with respect to the ground (top and bottom grounded). The amount of shear is doubled in this configuration at the same applied voltage used in **a)**.
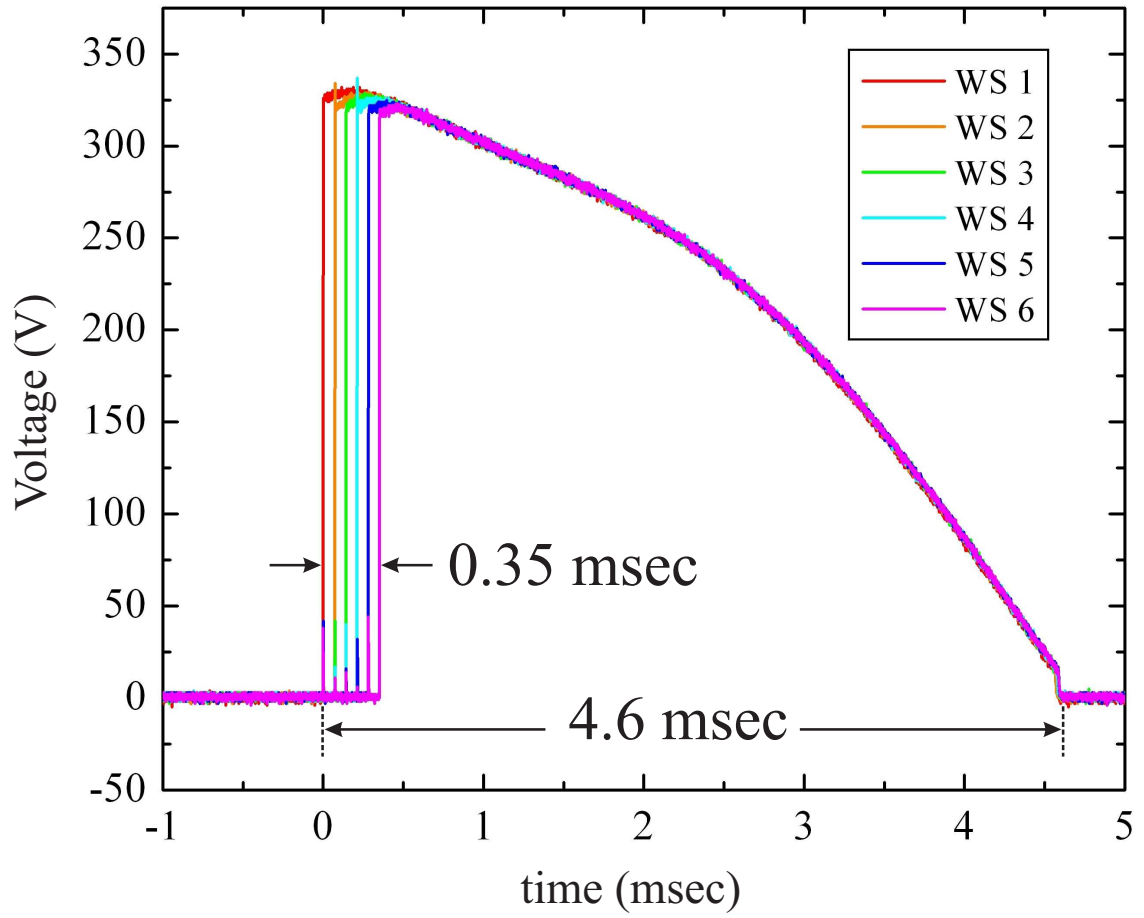
Figure 1.8: **Six voltage pulses at** $V = 325$ **V.**
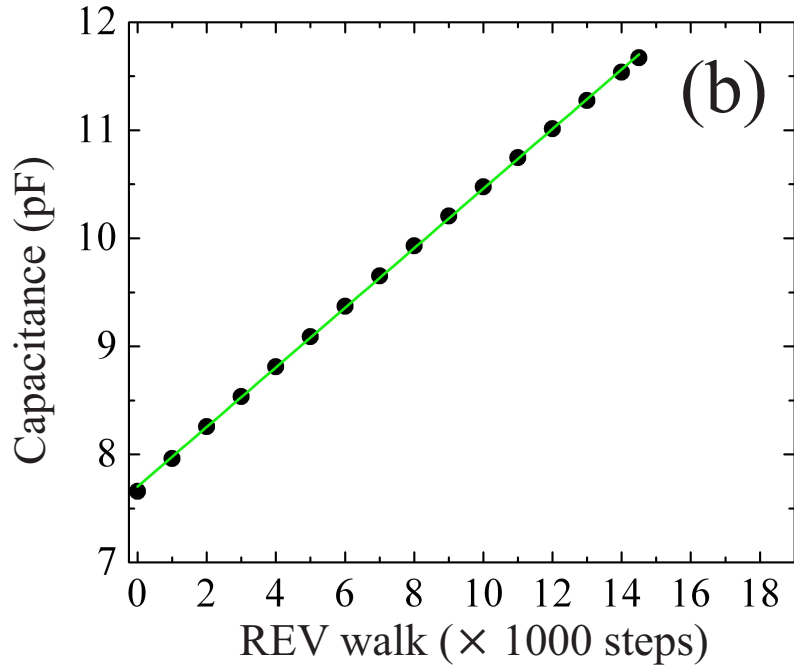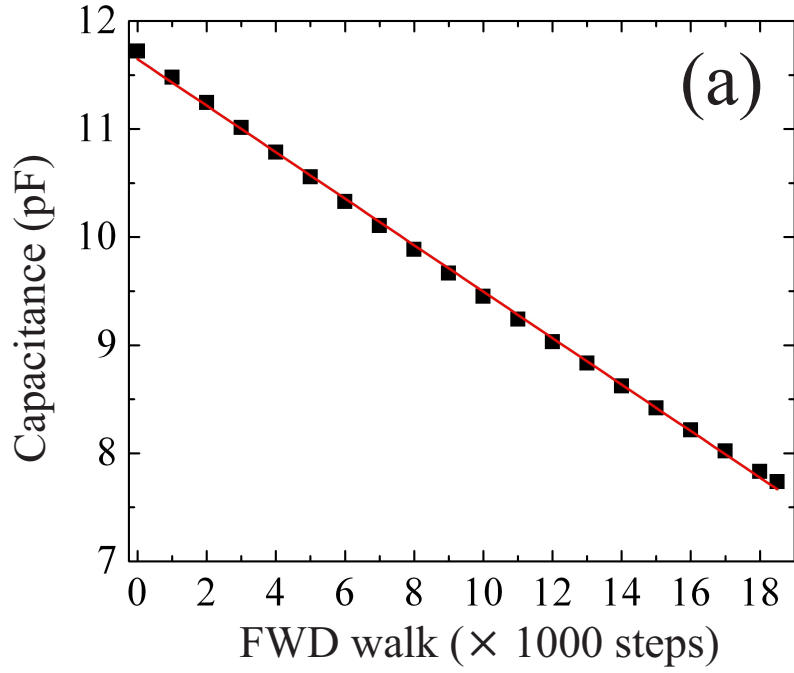
Figure 1.9: **Capacitance vs. walking steps.** When $V = 250$ V is applied to the six stacks of the shear PZT plates, **a) Forward steps.** $\Delta C/\Delta N|_{\text{fwd}} = -0.22$ fF/step **b) Reverse steps.** $\Delta C/\Delta N|_{\text{rev}} = +0.28$ fF/step

1.3.4 PZT Tube Scanner

By mounting a tip on a tube PZT, the three dimensional motion of the tip is realized (Fig. 1.10). A tube PZT has four electrodes at the outer surface and one electrode, at the inner surface. The tip moves along the x-axis (y-axis) by changing $\pm V_x$ ($\pm V_y$) with V_z and $\pm V_y$ ($\pm V_x$) fixed. To move the tip vertically, vary V_z while $\pm V_x$ and $\pm V_y$ are fixed. Quantitatively, the lateral and vertical motions are determined by

$$\delta x = \frac{2\sqrt{2}}{\pi} \times d_{31} \times \frac{\delta V_x}{t} \times \frac{L^2}{\phi} \tag{1.21}$$

$$\delta z = d_{31} \times \frac{\delta V_z}{t} \times L \ , \tag{1.22}$$

where $d_{31} = 95 \times 10^{-12}$ m/V, L, t, and ϕ are the relevant piezo electric coefficient, the length, the thickness, and the inner diameter of the tube. The tube PZT of the STM II has $L = 0.5$ in, $t = 0.02$ in, and $\phi = 0.210$ in. Each voltage, provided by the STM electronic control unit, varies from -220 to $+220$ V. Therefore, the estimated maximum ranges are $\approx 2.2 \times 2.2$ μm^2 in XY motion, and ≈ 1.0 μm in Z motion at RT.

Table. 1.2 shows the actual scan ranges at RT and 4.2 K after calibrating XYZ at the given temperature by using topography of graphite and Au[4]. The XYZ ranges at RT reasonably agree well with the previous estimated values. The XY range at RT decreases by a factor of 2.7 at 4.2 K, while the Z range at 4.2 K decreases by a

---

[4]According to atomically resolved topographic data (uncalibrated) of graphite and Au, the XY range was calibrated based on the known lattice constant vs. V_x and V_y. The Z range was calibrated by the step size of these materials vs. V_z by using a large area topography.

factor of 4.8. Apparently, the XY scan range of the PZT tube behaves similarly as the walking step size of the six stacks of PZT plates decreases by a factor of ~ 2.8 from RT to 4.2 K as discussed in the previous section. In contrast, the Z range decreases more than by a factor of 3 at 4.2 K. However, notice that the motion of a PZT tube is actuated by expansion and contraction, which is different from that of a shear PZT plate. According to the expressions of δx (δy) and δz, the former depends on L^2/ϕ while the latter depends on L. Therefore, δx (δy) and δz show different behavior at low temperatures.

Scan Range	RT	4.2 K
XY	$2.7 \times 2.7 \ \mu\text{m}^2$	$1.0 \times 1.0 \ \mu\text{m}^2$
Z	$1.3 \ \mu\text{m}$	270 nm

Table 1.2: XYZ scan ranges of STM II at RT and 4.2 K.
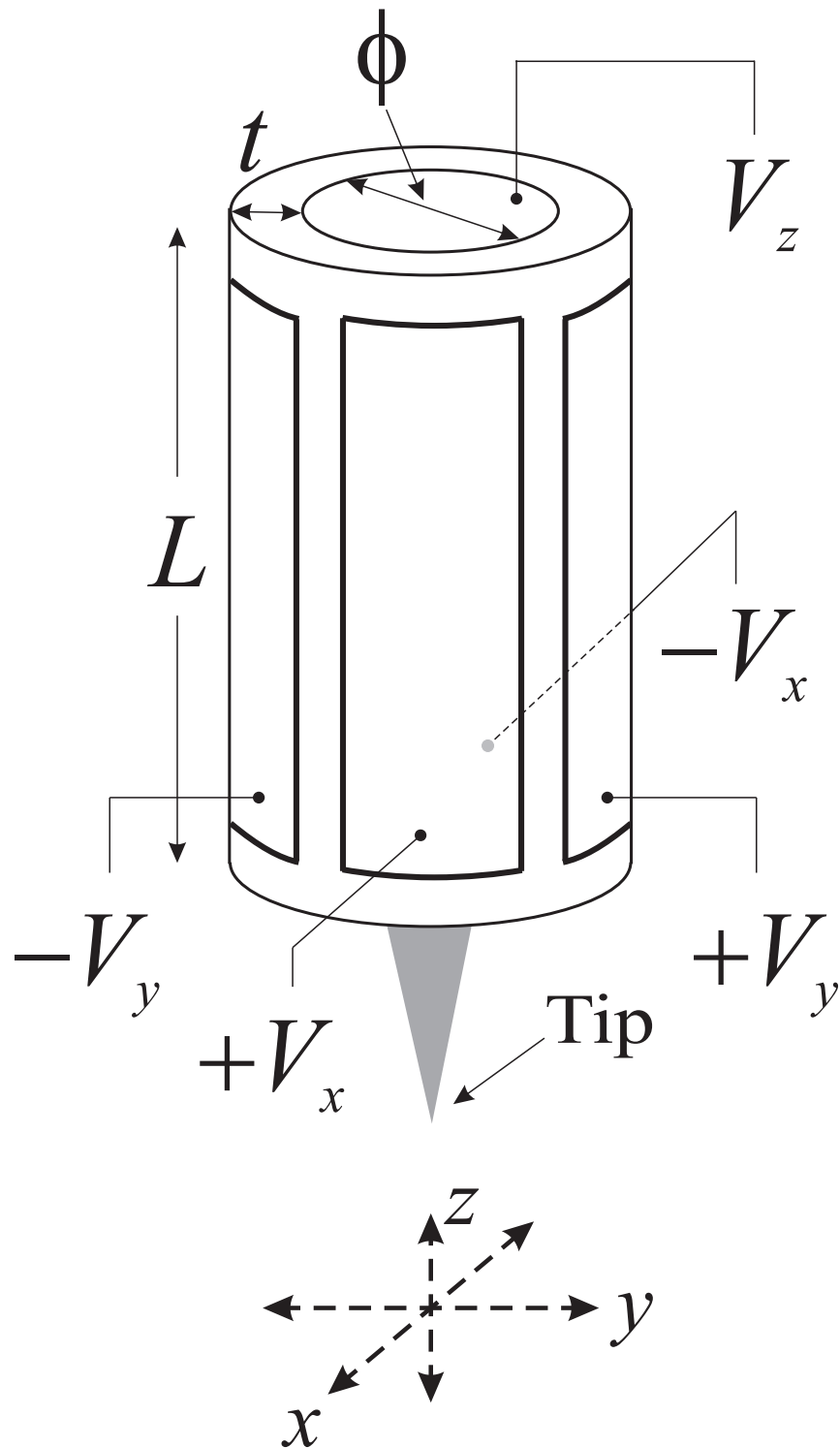
Figure 1.10: **Scanner tube PZT.** This tube PZT enables the tip to move in three dimensions. $\pm V_x$, $\pm V_y$, and V_z are the high voltages applied to the corresponding electrodes. L, t, and ϕ are the length, the thickness, and the inner diameter of the tube, respectively.

1.3.5 4 K Probe

I designed and built a 4 K probe according our experimental needs such as UHV, low temperature, high magnetic field compatibilities, and *in situ* sample/tip exchange. Fig. 1.11 shows pictures of the probe when the wiring was in progress. To minimize the liquid helium boil-off, thin walled tubing of stainless steel (SS) 304 was chosen. The center tubing ($\varnothing$ 1.0 in) was used for *in situ* sample/tip exchange and evacuating gas from the probe. Electrical wires between the STM and the electronics at RT run through five tubes ($\varnothing$ 0.25 in) around the center one. Conflat flanges (CF) were used for UHV electrical feedthroughs between vacuum and air (see Fig. B.2 for the assignment of electrical feedthroughs to the STM components and thermometers).

Since STM experiments require clean sample surfaces and high quality tips, we ruled out the usage of exchange gas to speed up the cooling time of the experiments. Therefore good thermalization to the STM should be realized via gold-plated oxygen free high conductivity (OFHC) copper. Three OFHC copper rods were attached between the top plate of the vacuum can and the precooling/electrical stage. Three more OFHC rods were connected between the precooling/electrical stage to the STM mounting plate. Six heat sinks for the electrical wires were bolted under the top plate, and six more were mounted on top of the STM mounting plate.

Coaxial cables (core: solid CuNi/shieding: braid CuNi) were used to access tip, bias, scanner, and inner/outer capacitors, to minimize the cross-talk. Furthermore, one small tube ($\varnothing$ 0.25 in) was exclusively dedicated for the tip cable to electrically

protect the tunneling signal from the rest. To access other components, I used manganin wires to minimize liquid helium boil-off due to their low thermal conductance. In addition to the electrical shielding using coax cables, I pushed in small pieces of SS mesh together with the coaxial cables to suppress the motion of wires inside the tubes. Because of the UHV compatibility need, lead-based solder was not allowed in making electrical contacts due to potential outgassing during UHV-bakeout. Therefore, I used UHV-compatible conducting epoxy (HD-21, Epotek) to make electrical connections.

Fig. 1.12 shows the completed 4 K probe with the STM attached to the mounting plate. For the feedthroughs, SMA and military multipin type connectors were used. Notice that the sample transfer rod (1), the differential pumping port (2), and the six-way cross (3) were implemented temporarily to carry out STM experiments before the UHV facility was implemented.

To measure the temperature, two thermometers (Cernox HD, Lakeshore) were placed inside the vacuum can. One is located at the precooling/electrical stage, and the other is under the bottom of the STM. One benefit of using Cernox HD thermometers is that the temperature can be read continuously from RT to 1 K. Using the implemented thermalization scheme as I described previously, it takes $7 - 8$ hours to cool down the probe (with the STM installed) from RT to 4.2 K (Fig. 1.13). The precooling with liquid nitrogen takes ~ 6 hr (A), and the cooling from 77 to 4.2 K, ~ 1.5 hr (B).

(a) (b) (c)
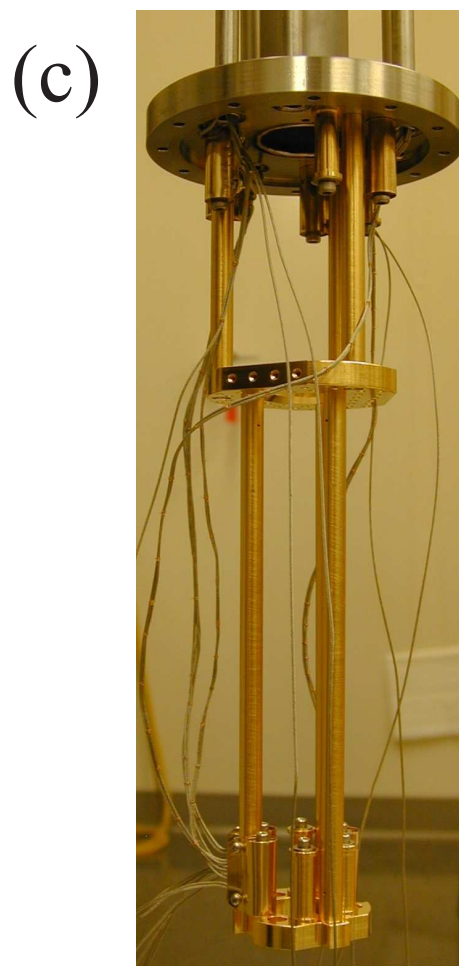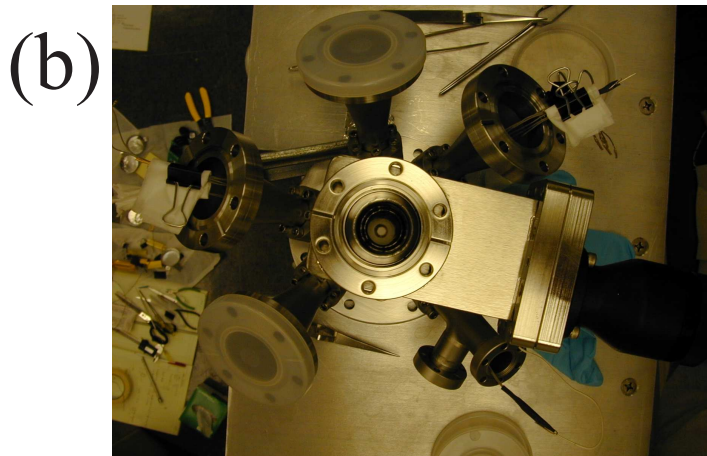
Figure 1.11: 4 K probe in progress of wiring.
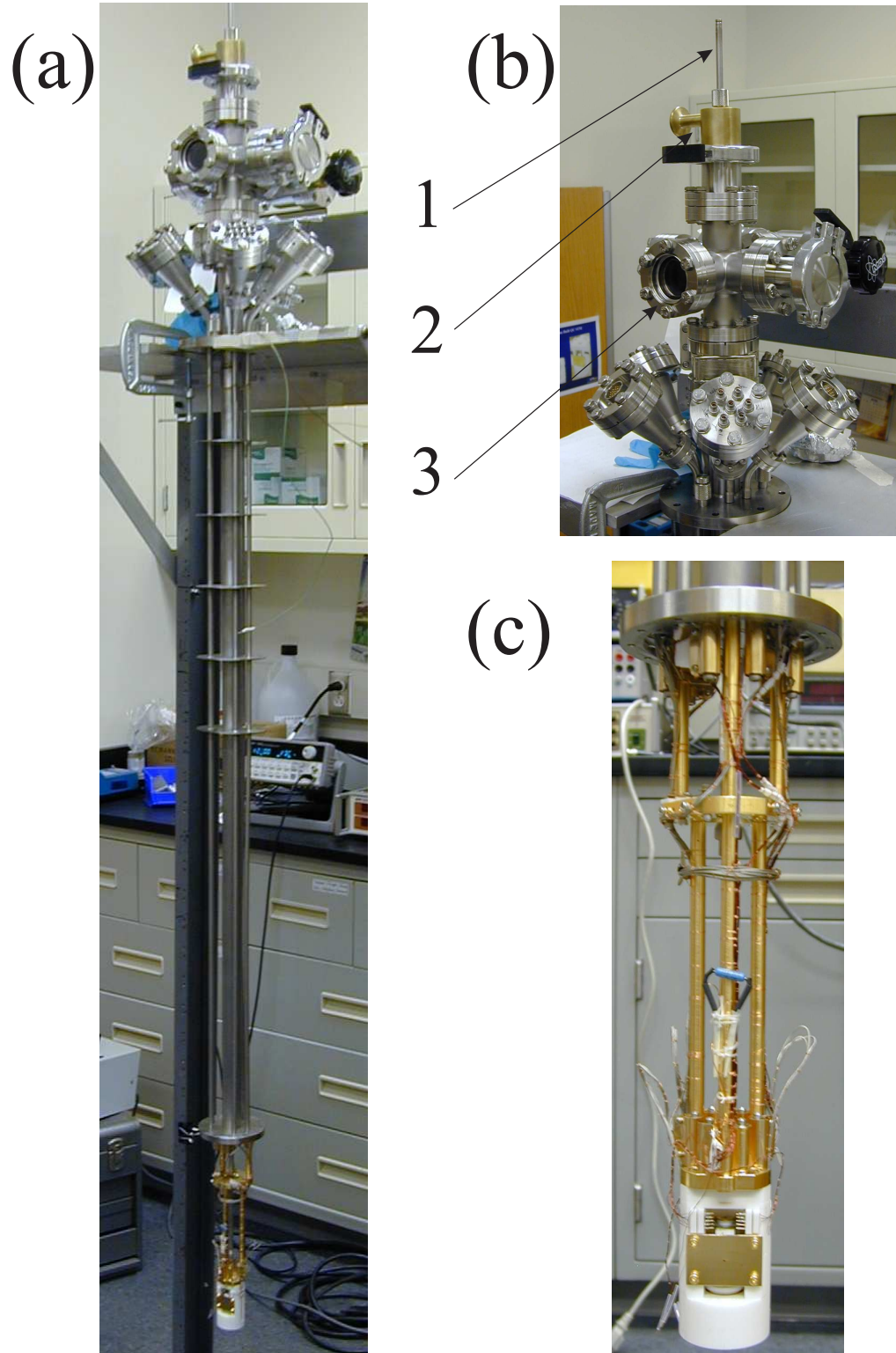
Figure 1.12: **Completed 4 K probe with STM.** This STM setup was used before UHV facility was implemented. 1: sample transfer rod, 2: differential pumping port, 3: six way cross.
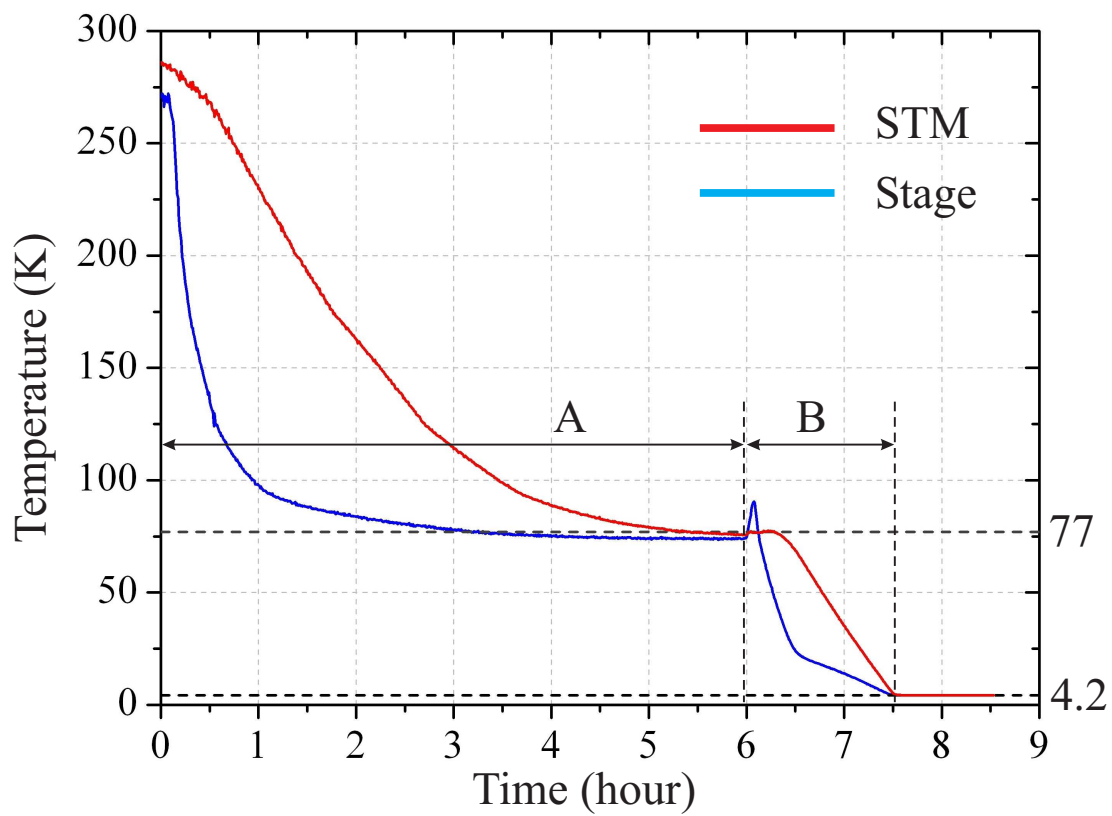
Figure 1.13: **Cool-down from RT to 4.2 K.** A: Precoolding with liquid nitrogen, B: Cooling with liquid helium.

1.3.6 Superconducting Magnet Dewar

Fig. 1.14 shows the 2-axis superconducting magnet dewar. The magnet was manufactured by the American Magnetics Inc. (Oak Ridge, Tennessee, USA) and the dewar custom-built by the Kadel Engineering Co. (Danville, Indiana, USA).

Our superconducting magnet, operating at 4 K, can produce a field up to 9 T vertically, or 2 T horizontally through the use of two independent solenoids. In addition to the independent magnet operation, a vector field of 1 T can be produced by simultaneously operating two magnets. In this operation, the vertical and horizontal magnets are energized to 0.71 T to produce a field of 1.0 T while the persistent heat switches are heated.

When the probe is inserted in the dewar with the STM installed, the liquid helium holding time is $\sim$ 7 days after the dewar is fully filled. This means that a measurement can be taken over a week, without being interrupted. Indeed, we took advantage of this maximum holding time to investigate the vortex motions in $NbSe_2$ in magnetic fields, which I will discuss in Chapter 5.

Figure 1.14: **Two axis superconducting magnet dewar.**

1.3.7 Vibration Isolation

Typically, a STM can resolve up to ~ 0.1 Å features. Therefore, perturbations from the environment should be suppressed to ~ 1 pm at the tunneling junction, unless the mechanical resonance frequency of the tunneling assembly is more than two orders of magnitude higher than the frequencies at which the vibration amplitude exceeds ~ 0.1 Å [11].

The mechanical vibration varies from place to place and time to time. Usually vibrations from 0 to 1 kHz are dominant. However, the resonance frequency of the tunneling assembly falls in the range of $1 - 10$ kHz, which mainly depends on the resonance frequency of the PZT scanner. Therefore, a vibration isolation scheme for a STM system should be implemented to resolve atomic features. This can be realized by attaching another mass (called isolation stage) to the tunneling assembly (Fig. 1.15a). The resonance frequency of the isolation stage should be at least two orders magnitude lower than that of the tunneling assembly. The coupled system gives a band rejection filter between f_{tunnel} and $f_{\text{isolation}}$ (Fig. 1.15b).

In our case, we adapted a custom-built optical table (TMC Inc., Peabody, MA, USA) as the vibration isolation (Fig.1.16). The $f_{\text{isolation}}$ of this table is $0.8 - 1.7$ Hz (the vertical natural frequency), when it is floated by four air springs.
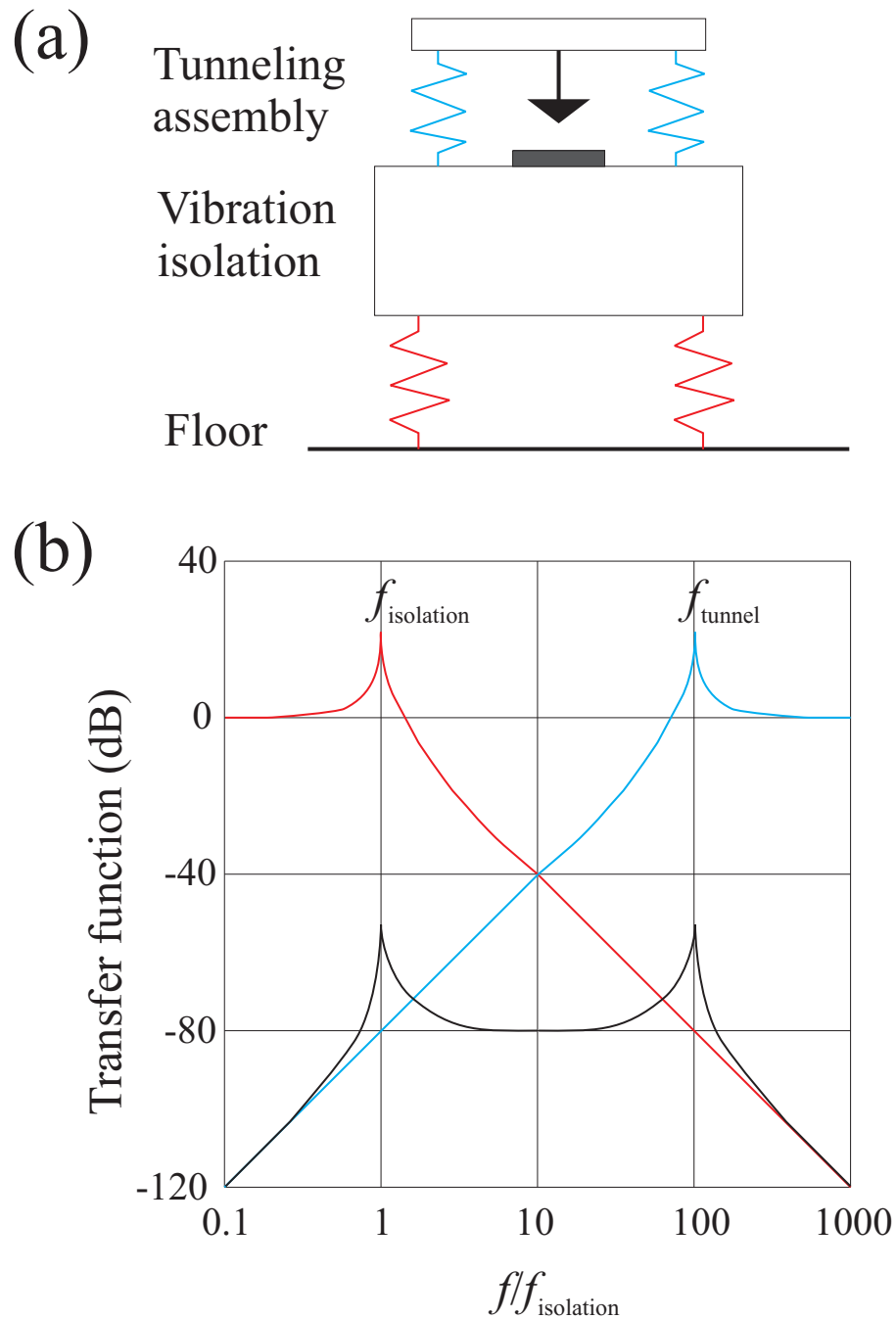
Figure 1.15: **Vibration isolation scheme. a) a coupled system.** A tunneling assembly is attached to an isolation stage which is attached to the floor. **b) Comparison of transfer function before/after the isolation scheme is applied.** Adapted from Ref. 11.
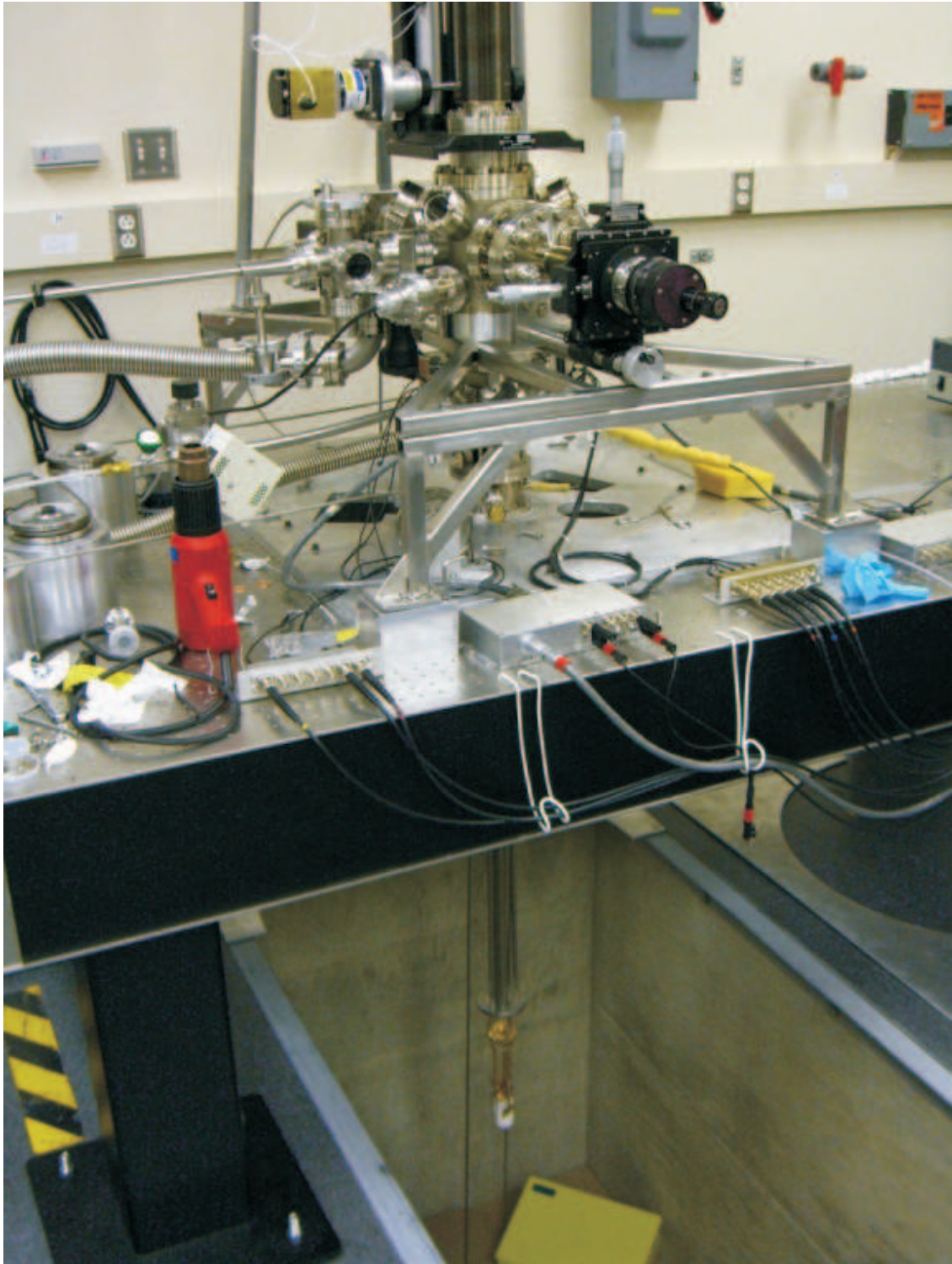
Figure 1.16: **Custom-built optical table.** The vertical natural frequency falls in a range of $0.8 - 1.7$ Hz and the horizontal natural frequency falls in a range of $1 - 1.9$ Hz when the table is floated by four air springs.

1.3.8 Ultra High Vacuum and Current Status of LT-STM

The UHV facility of our LT-STM system was built on top of the optical table (Fig. 1.17). The transfer chamber (1) is placed on top of the 4 K probe. Next to the transfer chamber, the sample preparation chamber (2) is placed. This preparation chamber is equipped with a Ar^+ sputter gun (7), evaporators (6), and a heater (located inside the chamber) to prepare clean surfaces. The fast entry lock chamber (11) is connected to the back of the preparation chamber for loading a sample into the chamber/unloading it from the chamber.

The transfer and preparation chambers are equipped with a set of a titanium sublimation pump (TSP, 3) and an ion getter pump (IGP, 4) for each to maintain UHV. The nominal pressure of $\sim 10^{-10}$ mbar in the transfer/preparation chambers is maintained by the operation of IGP and TSP. The fast entry lock chamber has a small turbo pump (10) for quick sample loading/unloading.

The horizontal translation of a sample inside UHV is accomplished by the horizontal manipulators (8) and XYZ stages (5). The vertical translation, required to transfer a sample from UHV to the STM, or vice versa, is realized by a vertical translator (9).

Fig. 1.18 shows the current status of the LT-STM associated with the UHV facility. We are now (as of November of 2007) in the phase of optimizing the performance of the UHV sample preparation (heating, sputtering, and evaporating materials) in parallel with STM measurements at LT.
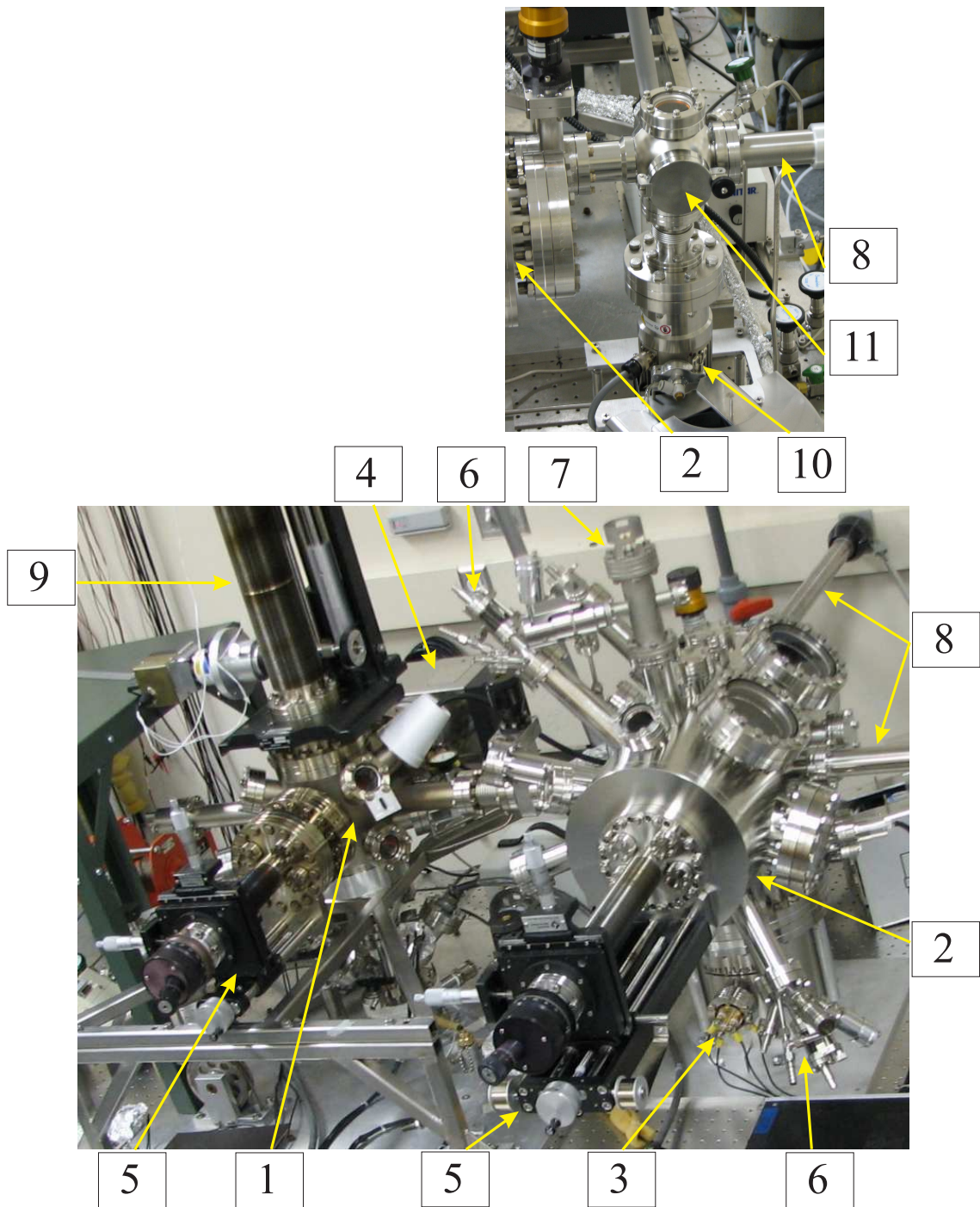
Figure 1.17: **UHV facility.** 1: Transfer chamber; 2: Preparation chamber; 3: TSP; 4: Ion getter pump; 5: XYZ stage; 6: Evaporator; 7: Sputter; 8: Horizontal translator; 9: Vertical translator; 10: Turbo pump; 11: Fast entry lock chamber.

UHV facility

Control unit
for LT, UHV, & Magnet

LT-STM
& Superconducting magnet

Vibration isolation

STM Control Unit
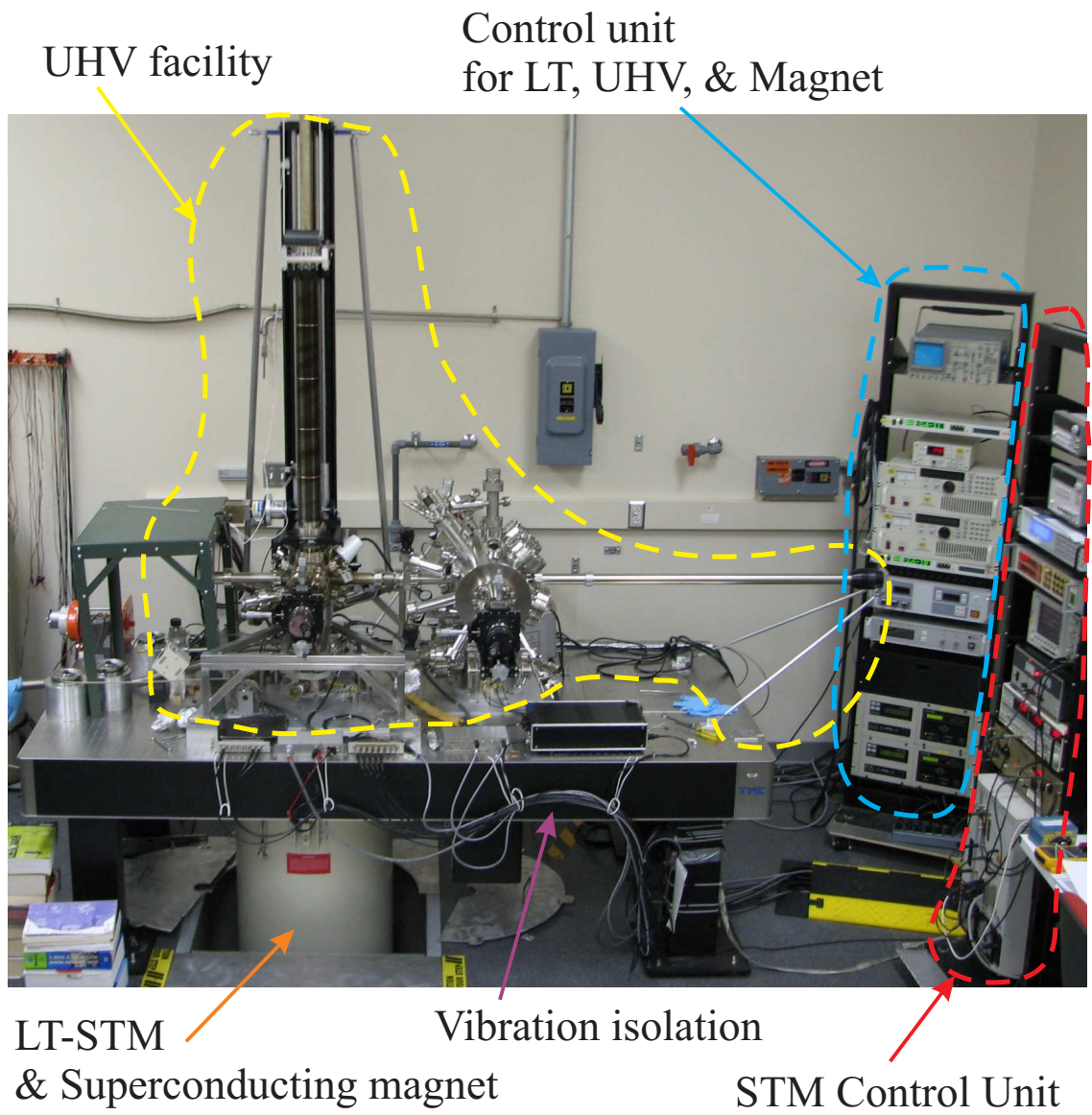
Figure 1.18: *In situ* Integrated LT-STM system at LPS as of November of 2007.

1.4 What Have We Done with the LT-STM?

After I completed the implementation of the LT-STM and the 4 K probe, we focused on tuning the performance of the STM by investigating several materials (Graphite, Gold, $NbSe_2$, *etc.*) at different temperatures with/without a magnetic field applied. Parallel with STM measurements, we also have been integrating the UHV facility to the LT-STM system. Therefore, we could not prepare samples under UHV condition until the current setup (Fig. 1.18) was established recently. The samples which I will discuss in this Thesis were prepared either in ambient pressure or by cleaving under high vacuum conditions.

In the following chapters, instead of presenting and discussing a single experiment using the LT-STM, I will present three different investigations on two different materials, to demonstrate the performance of the LT-STM in various applications.

In Chapter 2, data taken on surfaces of Au(111) is presented. Here, I will show a conductance map of the Au(111) surface, which was taken over several days to extract electronic information over the entire field of view. In addition, I observed moving steps while the STM continued scanning, which is not a common phenomenon at 4.2 K.

Chapter 3 covers the investigation of $NbSe_2$ without a magnetic field applied. I will show the coexistence of superconducting and charge density wave states at 4.2 K via topographic and spectroscopic measurements. Furthermore, the surface of this material can be modified deliberately, which resulted in a mixture of three different phases.

Chapter 4 is a brief overview of vortex dynamics in type II superconductor for the following chapter. In Chapter 5, I will present and discuss the magnetically driven motion of vortices in $NbSe_2$ at $\sim$ pm/s in moderately high magnetic fields.

Chapter 2

Investigations of Au(111)

2.1 Introduction

In this chapter, I will demonstrate the performance of the LT-STM, by showing the measurements done on Au(111) at 4.2 K. In general, the spatial resolution and the performance of vibration isolation can be checked by the quality of topographic data. For example, atomically resolved topography will ensure both aspects. In addition, a conductance map taken over days will be a measure of the stability of the STM.

We chose Au(111) for several reasons as following.

1. It is inert in air. Therefore, the sample preparation can be done without UHV condition.

2. It has been extensively studied in STM experiments since the birth of the STM. It is a well characterized material.

3. There is interesting physics to look at such as surface reconstruction and standing waves at low temperatures.

4. One can easily purchase it from the market at a reasonable price.
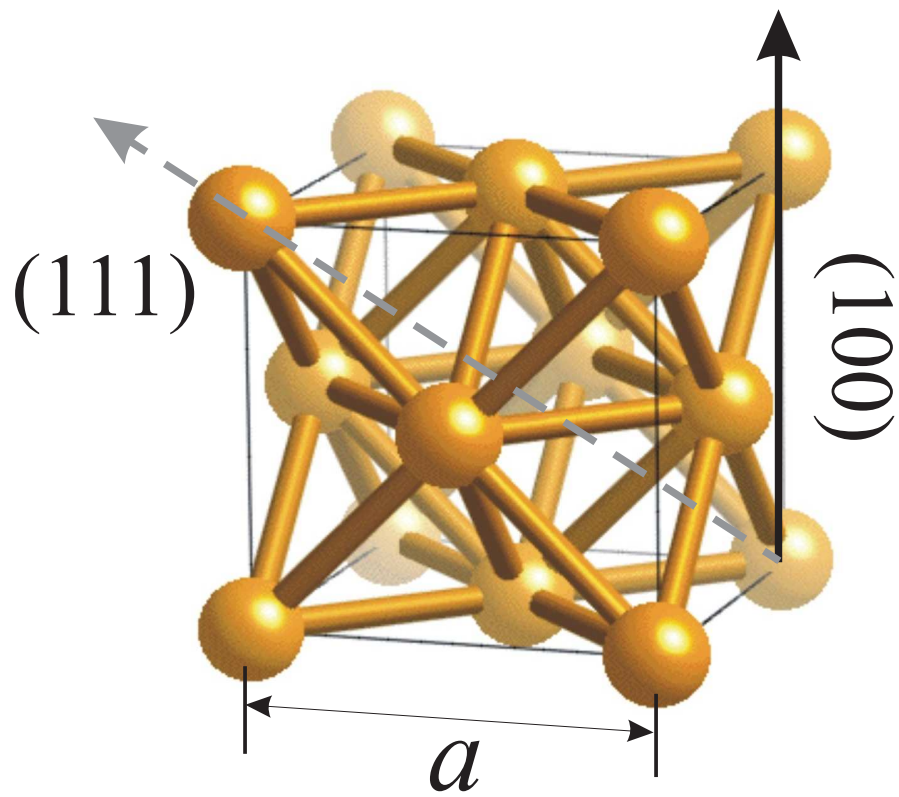
Figure 2.1: **Face-centered-cubic (fcc) structure of Au.** $a = 4.08$ Å

2.2 *In situ* Tip Preparation

Once a sample is selected to study, a tip is prepared *in situ* by using high voltage field emission (HVFE). Since the implementation of tip exchange mechanism is still on the way, a tip should be prepared at 4.2 K.

First, a tip approaches the surface of an Au single crystal (~ 1 mm thick) at 4.2 K by the coarse approaching process. Second, set the distance between the sample and the tip on the order of 100 nm with the feedback turned off. In this range of tip-sample distance, tunneling does not occur but a current due to field emission can be observed. Third, increase the bias voltage between the tip and the sample slowly, and monitor the current output at the current amplifier. Above a certain voltage (usually above ~ 100 V), instability of the current is observed due to local heating at the tip front end. Fourth, by continuously increasing the bias voltage, the current reaches up to $\sim \mu A$, and suddenly drops to zero. This indicates that some material at the tip front end is ripped off the tip, which are likely oxide layers. However, during this process, the tip end is likely to be blunt. Therefore, it is necessary to repeat the tip cleaning process.

To check the quality of the cleaned tip, there are two steps to be done. First, the $I - V$ characteristics and the work function measurement show how metallic the tip is. A good metallic tip shows the linear behavior in $I - V$, and a work function of $1 - 5$ eV. Second, the smallest feature in topography of Au indicates how sharp the tip is. A sharp tip means that the tip can resolve features on the Å scale or less. If either checking is not satisfactory, the *in situ* cleaning process is repeated until a

metallic and sharp tip is achieved.

We typically use either platinum-iridium (Pt-Ir) or tungsten (W) tips. The Pt-Ir tip is good for ambient condition because it does not oxidize. Therefore, the tip does not require an *in situ* cleaning process mentioned above. However, since it is relatively softer than the W tip, it is not feasible for long measurements such as conductance map, which requires stability for long time. In contrast to the Pt-Ir tip, the W tip oxides in air. Therefore, tip cleaning is necessary. For this Au study, I used a commercial tungsten tip [12].

2.3   Au(111) Preparation in Ambient condition

I used a commercial Au(111) film deposited on mica [13]. Au was prepared by flame-annealing for a minute or so in ambient condition. This annealing process will remove water layer on the surface. Simultaneously the heat energy will reconstruct the surface.

After the flame-annealing, the sample was put in the fast entry load lock chamber. Immediately, the chamber was pumped out by a turbo pump at its full speed of 38 kRPM. When the sample proceeded from the fast entry lock chamber to the sample transfer chamber, the nominal pressure of $\sim 10^{-7}$ mbar was maintained. Using the vertical transfer manipulator, the sample was loaded into the STM at 4.2 K.

2.4 Atomically Resolved Topography & $22 \times \sqrt{3}$ Reconstruction

Fig. 2.2 shows an unfiltered height image and a low pass filtered current image of Au(111) at 4.2 K. In the current image, Au atoms and surface defects are resolved. This confirms the spatial resolution of our STM and success of the vibration isolation.

Other than atomically resolved features, non-straight bright stripes at larger scale appear in the topography. These features result from the surface reconstruction (Fig. C.1) of top layers of atoms.

It has been verified, by various methods such as low energy electron diffraction (LEED), transmission electron microscopy (TEM), helium-atom diffraction, and STM, that Au is the only metal for which the (111) surface reconstructs [8]. In STM images of an Au(111) surface, one typically observes that two wide bright stripes enclose one narrow dark strip in parallel within a $22 \times \sqrt{3}$ unit cell (Fig. 2.3a), which manifest the surface strain. Often these stripes are called the herringbone reconstruction.

The surface strain causes the top layers of atoms to stack differently than the underlying layers. Since Au crystal has a face-centered-cubic (fcc) unit cell, the way of stacking layers of atoms along the (111) direction follows ABCABC... sequence (Fig. 2.4a) in the bulk. However, the atoms of the top layer of the surface tend to release the strain. This tendency causes the atoms on the topmost layer to contract uniformly along the [1$\bar{1}$0] direction (Fig. 2.3b). As a result, the energetically favorable fcc unit cell in the bulk switches to the hexagonal-close-packed (hcp) unit

cell in atoms over the ABAB-type stacking area, which leads to the superstructure of $22 \times \sqrt{3}$. Refer to Refs. $14, 15$ for more detailed STM studies of the $22 \times \sqrt{3}$ reconstruction of Au(111).
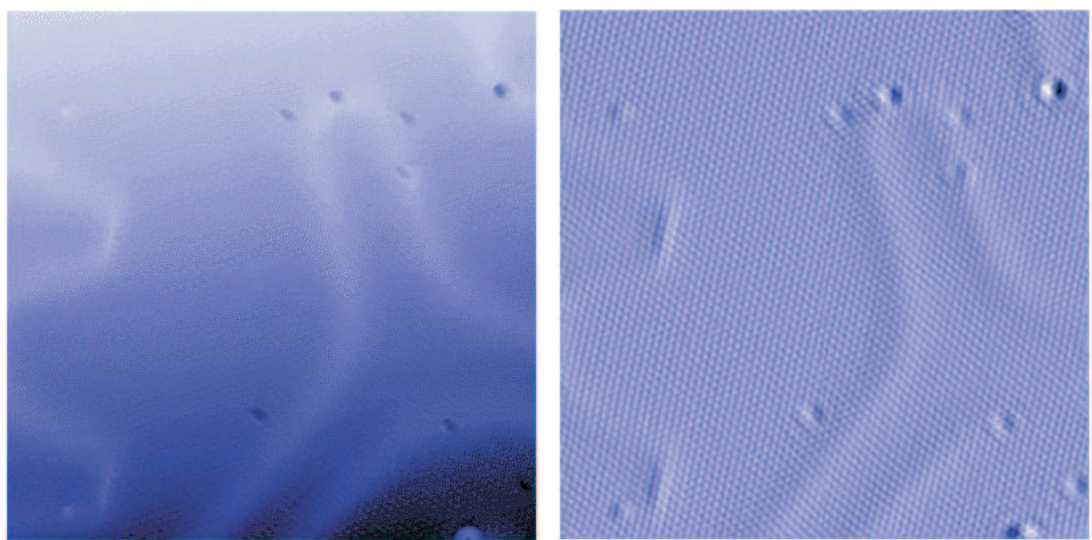
(a) Height   (b) Current

Figure 2.2: **Topography of Au (111).** Au atoms are resolved in the current image. Topography shows the herringbone reconstruction and surface defects. 20×20 nm^2, $I = 8.0$ nA, $V = 50.0$ mV.

(a)

20 Å

(b)

F   H   F

[11$\bar{2}$] (y)

1   3   5   7   9   11 13 15 17 19 21 23

[1$\bar{1}$0] (x)
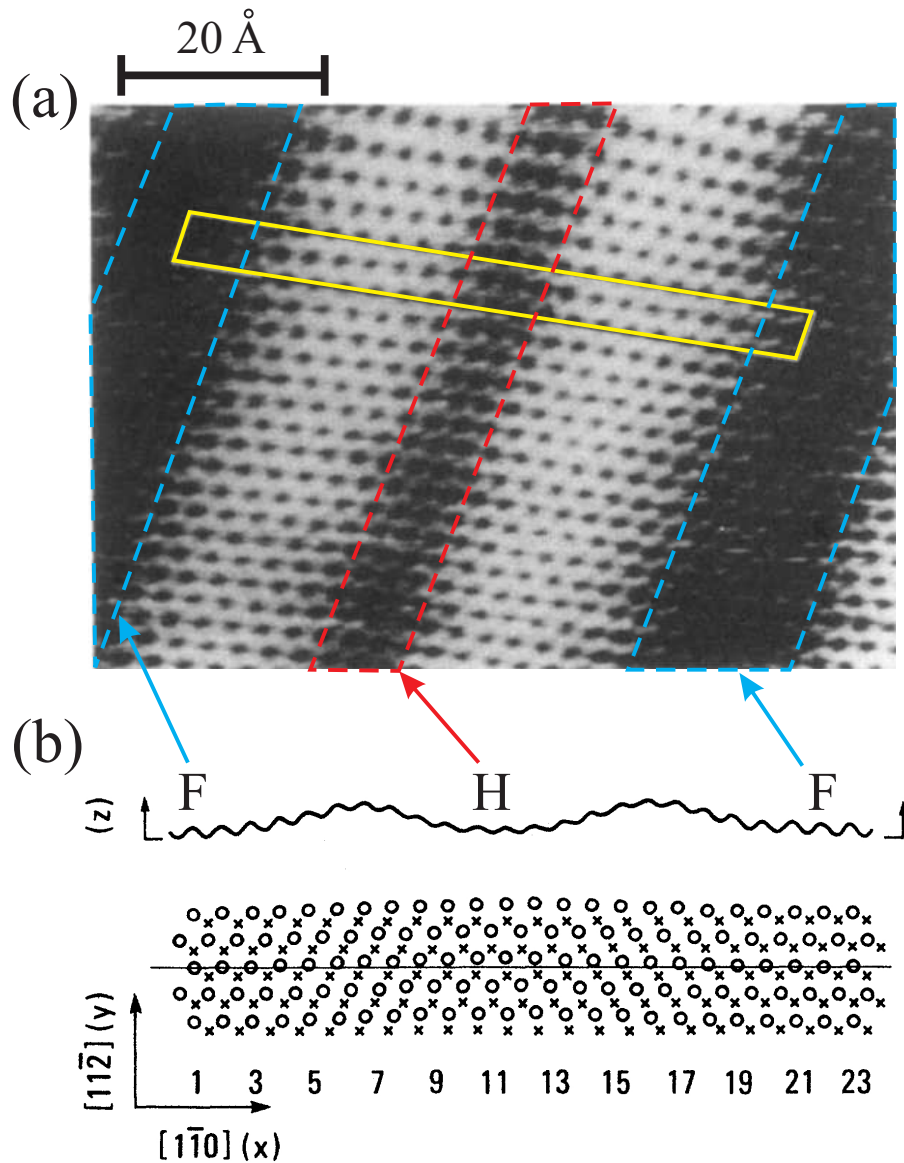
Figure 2.3: **Past studies of** $22 \times \sqrt{3}$ **reconstruction.** a) The yellow box indicates the unit cell of $22 \times \sqrt{3}$ due to the reconstruction of Au(111) surface. Measured at RT. Adapted from Ref. 14. b) In the region of F, the unit cell is fcc, while it is hcp in the region of H. "∘" denote the atoms on the topmost layer, and "×" denote the atoms underneath the top layer. Compare this with the top views of fcc and hcp in Fig. 2.4. Adapted from Ref. 15.

53

Side View   Top View

(a)

fcc   (111)

$$\frac{a}{\sqrt{2}}$$

(b)

hcp   (111)
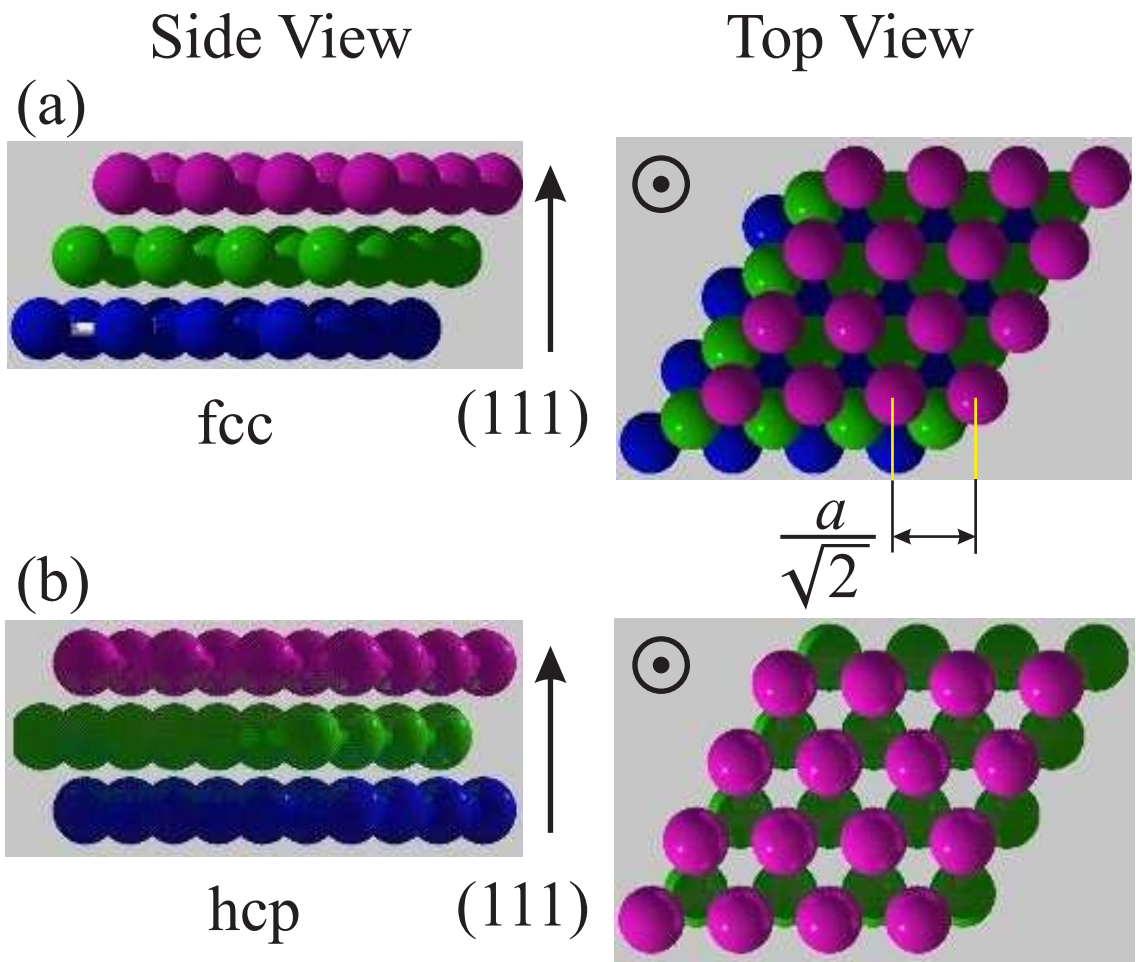
Figure 2.4: **Stacking ways of fcc and hcp unit cells.**

2.5   Conductance Map & Standing Wave

In addition to achieving atomically resolved topography of Au(111) as presented previously, mapping out LDOS over an area via a conductance maps was an important test of the stability of our STM.

First, we checked the surface condition in an area of 38×38 nm^2 with 256×256 pixels (Fig. 2.5). One can see two steps running from top to bottom in the field of view, herringbone reconstructions, and several impurities on the surface. Therefore, we expected to see the standing waves of electrons scattered by the impurities and steps in the conductance map.

The conductance map was realized by the following procedure.

1. Set the tunneling current to $I = 0.5$ nA at a bias voltage of $V = 1000$ mV with the feedback control on (*i.e.* constant current mode operation).

2. Move the tip to a position in constant current mode, park the tip there, and turn the feedback control off.

3. As the bias voltage step-wise changes from 1000 to -1000 mV at a voltage step of 40 mV, measure the tunneling current response (ΔI) by adding an *ac* voltage ($\Delta V = V_{\mathrm{mod}} = 40$ mV at $f_{\mathrm{mod}} = 1973$ Hz) to the bias voltage. Therefore, a single trace of $\Delta I / \Delta V$ vs. V with 51 data points is expected.

4. After the measurement is done, turn back on the feedback control.

5. Repeat steps 2, 3, and 4 until the tip completes scanning over the area.

6. This procedure produces 256×256 traces of $\Delta I / \Delta V$ vs. V in the area of 38×38 nm^2, giving us a measure of $\Delta I / \Delta V(x, y, V)$.

The images on the left in Fig. 2.6 show three layers of the conductance map at $V = +320, 0, -320$ mV (from top to bottom). One can see "ripples" in each layer, which are a manifestation of standing waves of electrons at the surface state at the given energy. Although it is not easy to determine the periodicity of standing waves in conductance data, the Fast Fourier transformation (FFT) of a layer of the conductance map on the right in the figure shows a ring shape feature the radius of which determines the periodicity of the standing wave. However, there exists a slight asymmetry of the ring in FFT data due to creep of the tube scanner. To determine the magnitude of wave vector of ripples, k^{ripple}, at a given bias voltage, we used the average of $k_{\text{max}}^{\text{ripple}}$ and $k_{\text{min}}^{\text{ripple}}$,

$$k^{\text{ripple}} \equiv \frac{2\pi}{\lambda^{\text{ripple}}} = \frac{k_{\text{max}}^{\text{ripple}} + k_{\text{min}}^{\text{ripple}}}{2} \,, \qquad (2.1)$$

where $k_{\text{max}}^{\text{ripple}}$, $k_{\text{min}}^{\text{ripple}}$, and λ^{ripple} are the maximum, minimum radii of the ring, and the periodicity of ripples, respectively. Therefore, the magnitude of the wave vector of standing wave is $k = \frac{1}{2}k^{\text{ripple}}$, because $\lambda = 2\lambda^{\text{ripple}}$, where λ is the periodicity of the standing wave[1]. The collection of energy $E \ (= eV)$ vs. k gives the dispersion relation of the surface state electrons of Au(111).

To find the dispersion relation, one can use a two dimensional free-electron-like

---

[1] The tunneling current is proportional to $|\psi|^2$, not to ψ, where ψ is the wave function of an electron.

model

$$E = \frac{\hbar^2 k^2}{2m^*} + E_0 \ , \tag{2.2}$$

where $\hbar = 1.05 \times 10^{-34}$ J·s, m^* is the effective mass of electron, and E_0, the binding energy. By fitting the data of (k, E), extracted from the conductance map, to Eq. 2.2, we calculated an effective mass of $0.24m_e$, where $m_e = 9.1 \times 10^{-31}$ kg (Fig. 2.7).

Fig. 2.7 also shows two sets of data from other groups for comparison with our measurement. Hasegawa *et al.* [16] extracted the period of the standing waves at RT in their STM experiment, and they found $m^* = 0.15m_e$. Kevan *et al.* [17] carried out photoemission experiments to find $m^* = 0.28m_e$, which is an averaged surface measurement.

Our value of m^* is close to that measured by Kevan *et al.* while it appears different from that measured by Hasegawa *et al.*. In our STM experiment, we determined the k by measuring the LDOS modulations due to standing waves in a local area of the sample. In photoemission measurement, Kevan *et al.* directly measured the k of standing waves over the entire surface. Presumably, the slight difference between our m^* and that of Kevan *et al.* is because the former was calculated from an indirect measurement of k in a local region while the latter was calculated from a direct measurement of k over the entire surface. On the other hand, the m^* of Hasegawa *et al.* deviates from ours by ~ 40 %. Hasegawa *et al.* extracted the k by measuring the modulation of LDOS close to a step edge. In this case, the potential, seen by surface state electrons, at the step edge is different from

that away from the step edge. Therefore the m^* of Hasegawa *et al.* was affected by the influence of the step, which lead to a smaller value than ours or that of Kevan *et al.*.
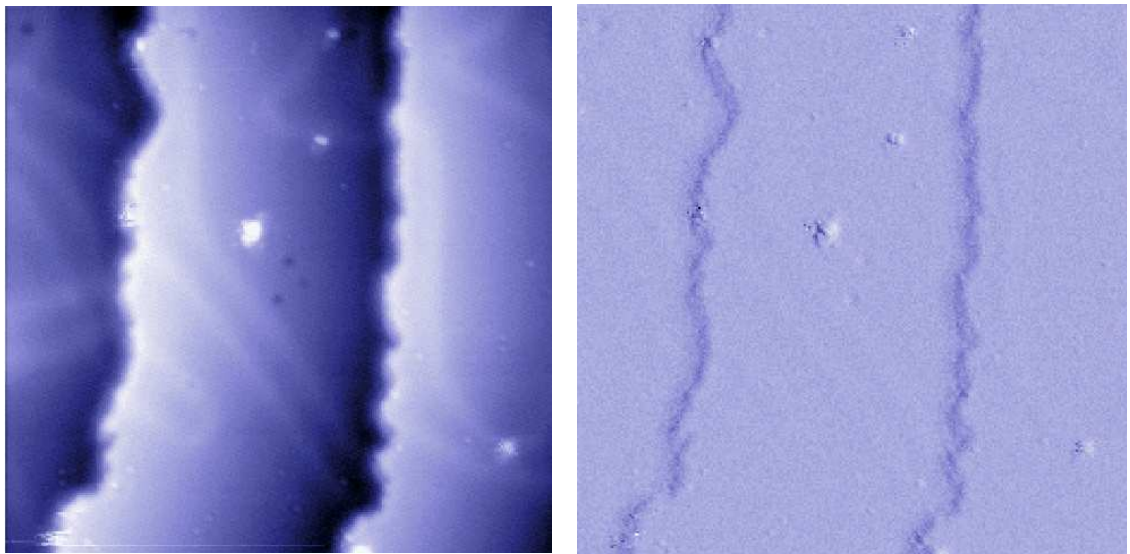
(a) Height   (b) Current

Figure 2.5: **Topography of Au(111) for a conductance map.** An area of 38×38 nm^2 was selected for the conductance map in Fig. 2.6. $I = 0.5$ nA, $V = 1000$ mV.
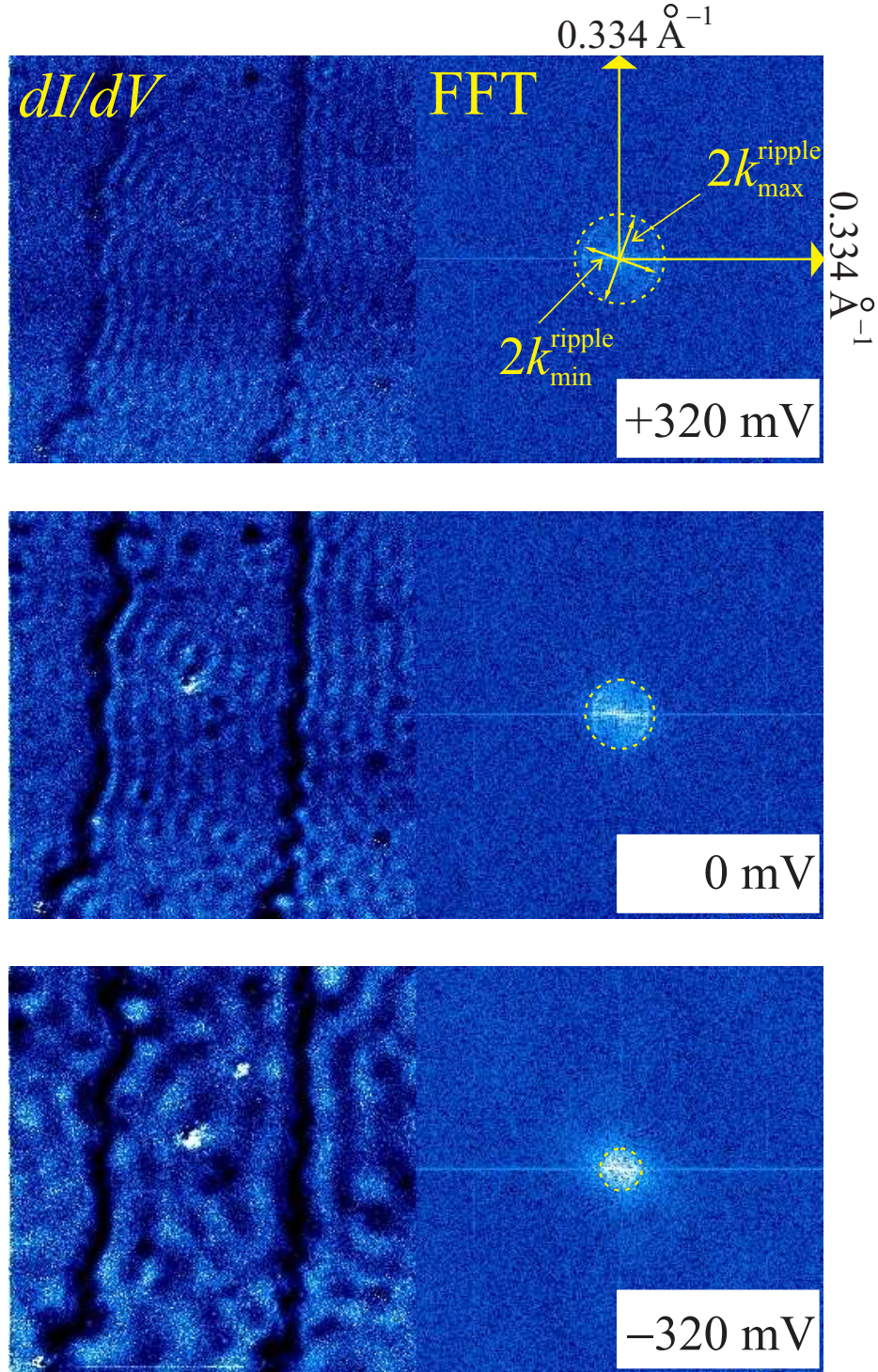
Figure 2.6: **Conductance map and FFT. Left:** Three layers of a conductance map at +320, 0, and −320 mV, from top to bottom, over the same area in Fig. 2.5. The periodicity of ripples is hard to determine by directly using a dI/dV data. **Right:** Their corresponding FFTs. A ring manifests the periodicity of wiggled feature in its corresponding dI/dV data. $k_{\text{max}}^{\text{ripple}}$ and $k_{\text{min}}^{\text{ripple}}$ are the maximum and minimum radii of a ring, respectively. $I = 0.5$ nA, $V = 1000$ mV.
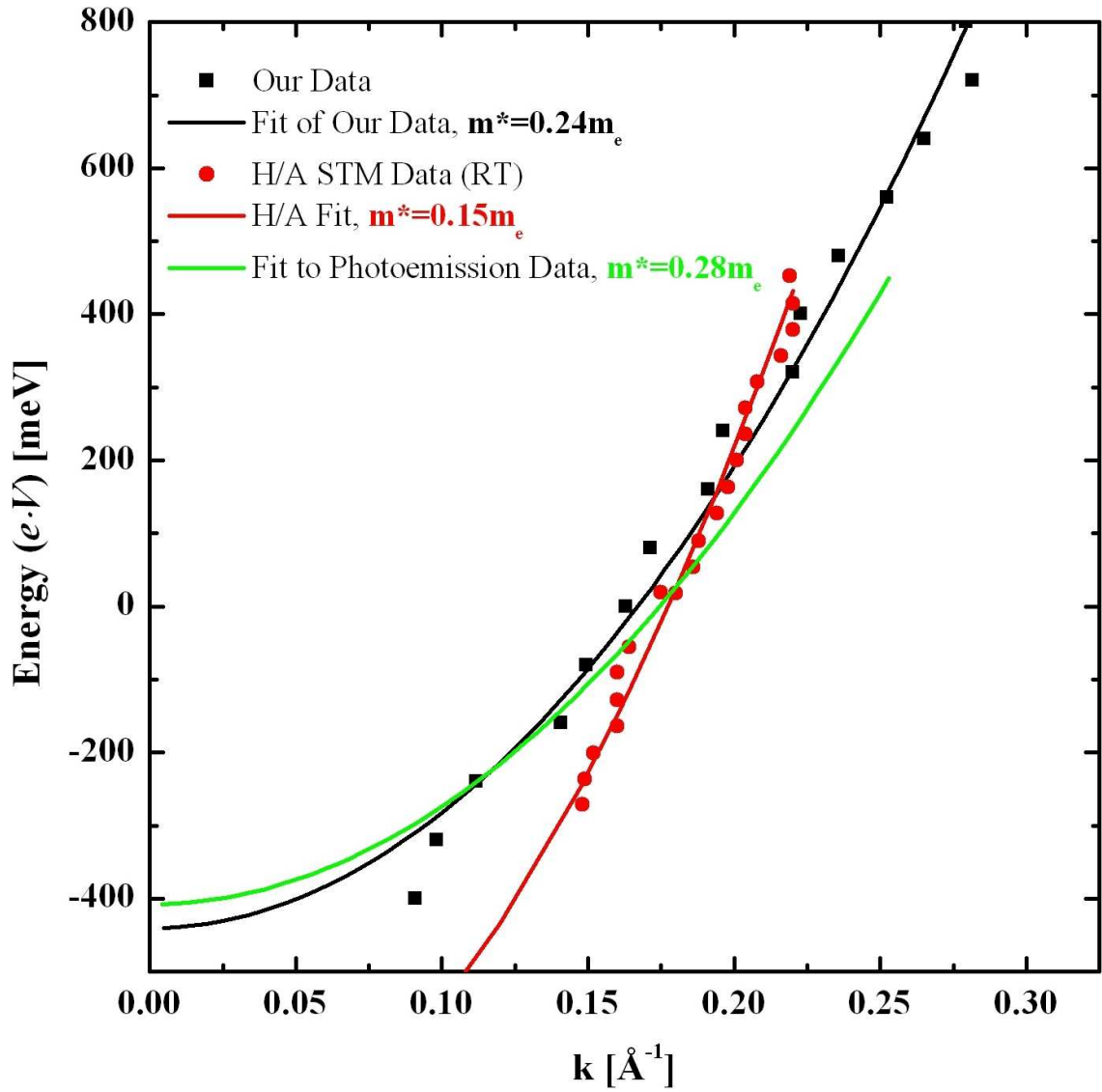
Figure 2.7: **Dispersion of surface state electrons of Au(111).** Data of another STM measurement [16] (red) and photoemission measurement [17] (green) are plotted for comparison with our data.

2.6 Moving Steps at 4.2 K

Although the flame-annealing was good enough for achieving atomically resolved topography of Au(111) without an UHV facility, this process usually left adsorbates and residual "dirt" on the surface, because it was done in ambient conditions. When a tip landed on a dirty area, we exchanged the sample with a new one, or kept scanning over a larger area until the tip swept away the "dirt" on the surface. Often, the latter method was good enough to get atomically resolved topography after continuous scanning for a long time[2].

During the period when I was investigating topography and spectroscopy of Au(111) as presented previously, I observed unexpected dynamics of Au steps at 4.2 K (Fig. 2.8 and Fig. 2.9). As usual, I flame-annealed the surface of Au(111) on mica in ambient conditions, and transferred it to the STM at 4.2 K following the procedure described earlier (Sec. 2.3).

To remove the dirt on the surface from the field of view, I kept scanning over a large area [512×512 nm^2 (1024×1024 pixels)] overnight. I used a scan-speed of 150 nm/s with $I = 0.05$ nA and $V = 800$ mV. At this scan-speed, it took 2 hr 43 min to complete a scan over the area. The cleaning process continued over 30 hours, which produced 12 frames of topography in total. In Fig. 2.8, only every other frame is displayed (down-scans[3]). As scanning went on, the quality of topography

---

[2]The scanning for sweeping dirt on a surface usually continued for several hours. However, sometimes it continued for over a day.

[3]In a down-scan, a STM tip moves fast horizontally for a line scan. After finishing the line scan, the tip moves down to a next line for another line scan. Therefore, to complete a 2-dimensional topography in a down-scan, tip slowly moves from the top line to the bottom one. On the other hand, in an up-scan, the tip moves up to a next line after finishing a line scan. Therefore, the slow motion of the tip occurs from the bottom line to the top line.

got better. This indicates that the tip continued removing the residue or dirt. One can clearly see the overall changes of the surface during continuous scanning. For example, the straight edges of two steps (refer to green dashed line) change to non-straight ones. The size of an island (yellow dashed line) close to a step edge gets smaller. A pit (orange line) gets filled up during the continuous scanning. This sequential topography not only shows removal of material but also shows pile-up of material within the field of view. In other words, it shows a mass-transfer phenomena at this low temperature.

The first image in the figure shows most steps were lined up in one direction ($\sim 116°$ from the horizontal line) with screw dislocations crossing steps. The aligned direction of Au steps is likely to match the direction of mica steps because Au is a thin film (150 nm thick). The lattice mismatch between mica substrate and 150 nm thick Au film should influence the Au deposition process on mica. Furthermore, more stress can be built due to the difference of thermal contractions of Au and mica as the sample cools down to 4.2 K. As a result, one can observe lined-up steps and screw dislocations as shown in the first image. In other words, strong stress was built on the Au film in the first place due to the lattice mismatch and the different thermal contractions. The last image shows more complicated steps edges, which implies that the initial stress was relieved by the deformations of steps.

To see the detailed dynamics of the surface, I zoomed in to an area of 120×120 nm^2, where herringbone reconstructions were clearly visible in addition to steps, and continued to scan the area at a scan-speed of 300 nm/s (Fig. 2.9). This scan-speed gave a completion time of 5 min 30 sec per frame. Notice that the herringbone

reconstructions on the surface changed as the steps continued changing. As discussed earlier, herringbone reconstruction is caused by the layer stacking mismatch, which is one kind of relaxation due to stress. In other words, the shape of herringbone represents the distribution of strain in a material due to stress. Continuous removal and pile-up of material will relieve the initial stress, which will lead to different shapes of herringbone structures.

Although we do not understand the details of what caused the motion of Au steps at this low temperature, the motion was related to tip-sample interaction. For example, when I parked the tip overnight in an area, and scanned the same area the next day, I did not see any change on the surface based on the topography. We also carried out more experiments of 150 nm thick Au films at 4.2 K by varying scan parameters[4] after flame-annealing in ambient conditions. The material removal speed depended on the scan-speed. Qualitatively, the faster the scan-speed, the faster the removal speed. In addition, changing the polarity of bias voltage appeared not to affect the step motion. Reducing the scan-speed at $\sim$ 10 nm/s still induced steps to change. We did not find a threshold voltage above which the step motion does not occur.

Tip-induced material motions are well known phenomena in STM experiments. For example, Eigler *et al.* [2] demonstrated adsorbate atoms (Xe) on a metal surface (Ni) can be positioned at desired site by controlling the bias voltage at 4 K. Böhringer *et al.* [18] showed the lateral motion of adsorbed molecules (1-

---

[4]We used scan parameters of $I = 0.05 \sim 0.1$ nA, $V = -500 \sim +500$ mV, and scan-speed $= 10 \sim 300$ nm/s.

nitronaphthalene) on Au(111) at 10 and 50 K. Yin *et al.* [19] reported that finger

shape motion of steps of Au(111) at RT. To increase the tip-sample interaction and

induce the motion of materials, they used a higher tunneling current of $10-60$ nA [2],

an enhanced bias voltage of $+1.5$ V [18], or higher current and bias voltage together

$(30-50$ nA and $+1.5$ V) [19]. In contrast, we observed step motions of Au(111) at

4.2 K by using regular scan parameters, which was not reported previously to the

best of our knowledge.
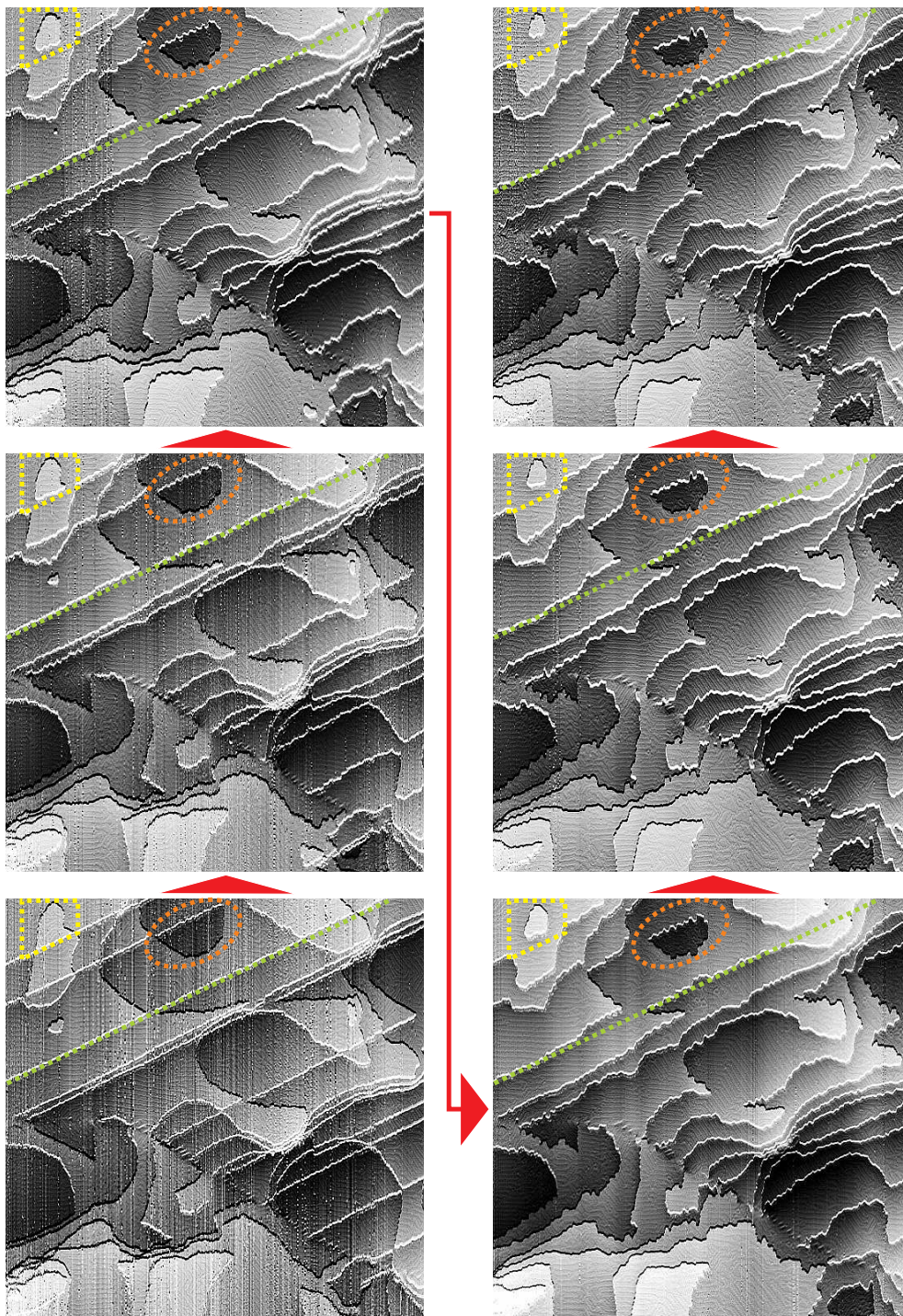
Figure 2.8: **Step motion of Au at 4.2 K.** The sequential topographies show the motion of Au steps while continuously scanning over an area of 512×512 nm^2 at a scan-speed of 150 nm/s. For example, see how the features referenced by yellow, green, and orange dotted lines change in sequence. Each topography (down-scan) took 2 hr 43 min to complete. Adjacent topographies are 5 hr 36 min apart. $I = 0.05$ nA, $V = 800.0$ mV.
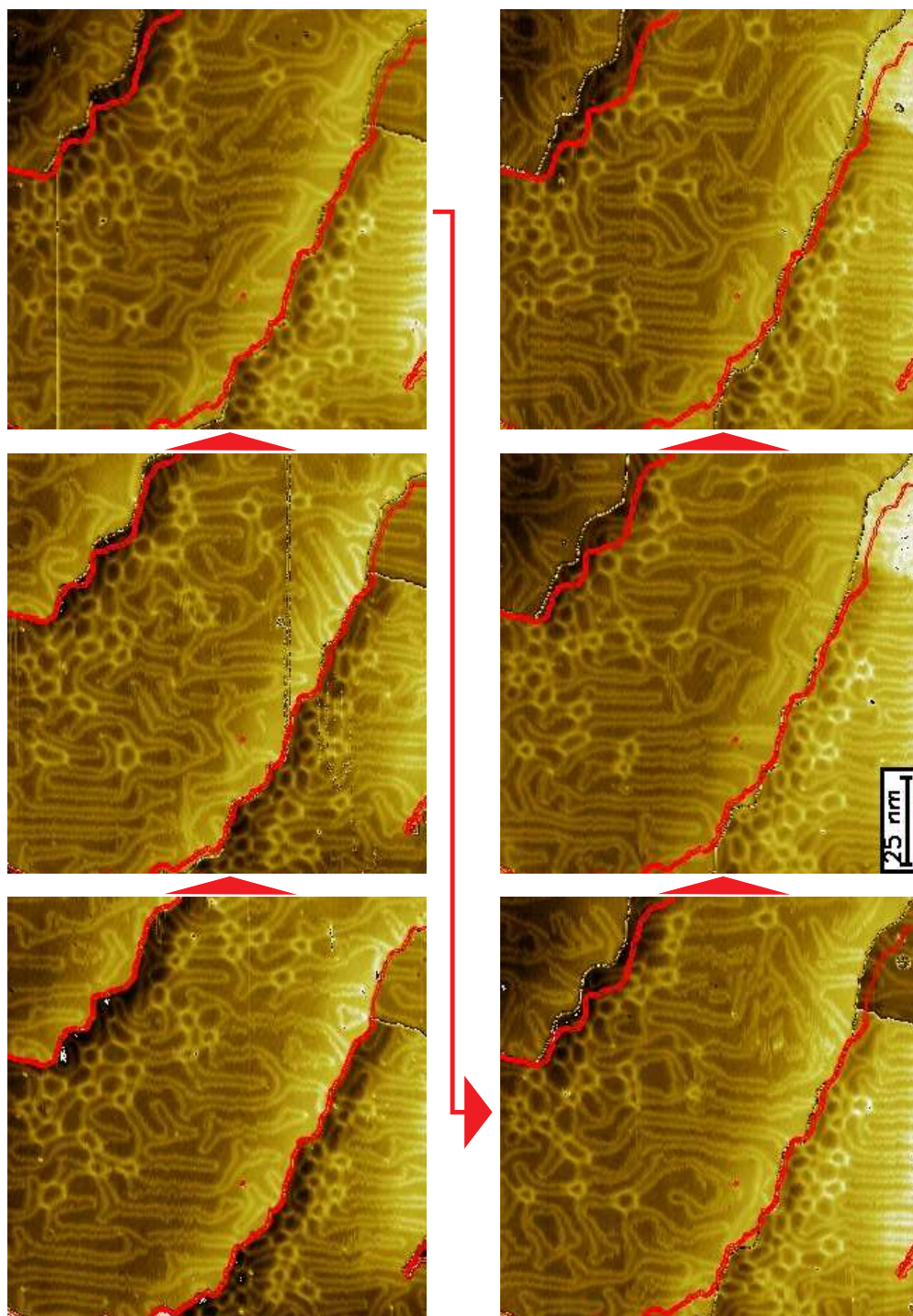
Figure 2.9: **Dynamics of herringbone reconstruction.** Red lines mark the initial boundary of steps. The sequential topographies show the dynamics of herringbone reconstructions as the steps change while continuously scanning over 120×120 nm^2 at a scan-speed of 300 nm/s. The completion time of a scan over the area was 5 min 30 sec. Adjacent topographies are 11 min apart. $I = 0.05$ nA, $V = 800.0$ mV.

Chapter 3

Investigations of NbSe$_2$ without Magnetic fields

3.1 Why NbSe$_2$ with STM?

NbSe$_2$ is a very popular material for low temperature STM experiments [10,20]. As the temperature goes down, it shows a charge density wave (CDW) transition below $T_c^{\mathrm{CDW}} = 32$ K, originating from the strong electron-phonon interaction [21]. Further down, below $T_c^{\mathrm{SC}} = 7.2$ K, it shows type II superconductivity. Since the operation temperature of our STM is 4.2 K, we could observe both states simultaneously at this temperature.

In addition to the coexistence of CDW and superconducting phases at 4.2 K, as an external magnetic field is raised above the lower critical field, the superconductivity of NbSe$_2$ switches from the Meissner state (complete diamagnetism) to the mixed state (the coexisting phase of superconducting and normal states), and remains in the mixed state until the applied field reaches the upper critical field. Above the upper critical field, it becomes normal. This kind of superconductor, type II superconductor, is distinct from the type I superconductor: a type I superconductor only shows the Meissner state below its critical field and becomes normal above it. In the mixed state of a type II superconductor, the threaded magnetic fields form a triangular lattice (or Abrikosov lattice, Ref. 22), which I will discuss in Chapters 4 and 5.

Not only does NbSe$_2$ have rich physics at low temperatures with/without magnetic fields, but also an atomically flat surface can be achieved by cleaving in vacuum since it is a layered material (Fig. 3.1). This allowed us to investigate this material without full operation of an UHV facility. I typically cleaved NbSe$_2$ under $\sim 10^{-7}$ mbar in the fast entry lock chamber at RT, and transferred it to the STM at 4.2 K.
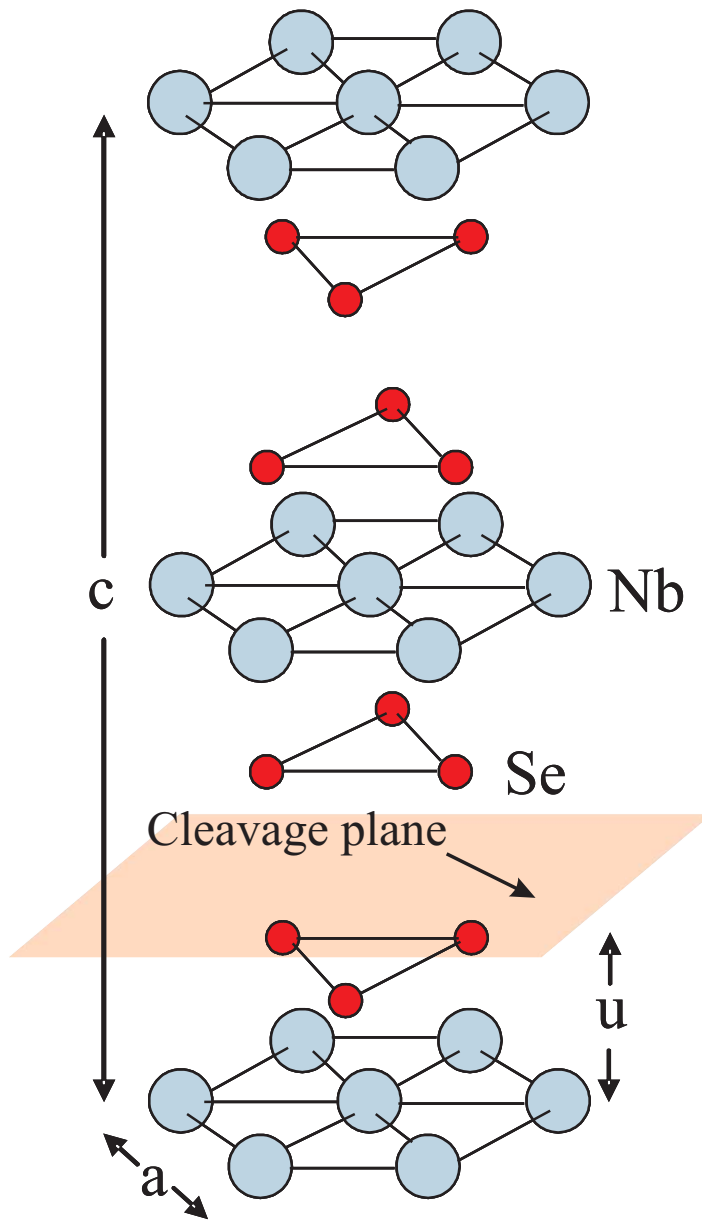
Figure 3.1: **Crystal structure of NbSe$_2$.** a = 3.45 Å, c = 12.54 Å, and u = 1.68 Å.

3.2   Charge Density Wave: 3×3 Phase

Low dimensional metals (1D or 2D) with highly anisotropic band structures, due to strong electron-phonon interactions, may experience a CDW transition at low temperatures [21, 23]. In the 1-D free electron model, without considering the electron-electron and electron-phonon interactions, the conduction band of a metal with a lattice constant a is filled up with electrons up to the Fermi energy at $T = 0$ K, showing a constant charge density of $\rho(x) = \rho_0$ (Fig. 3.2a). However, by taking into consideration the electron-phonon interaction, a more energetically favorable state develops by electron-hole pairs involving the wave vector of $q_{\mathrm{CDW}} = 2k_{\mathrm{F}}$ [23]. As a result, the electron density of the metal modulates spatially (Fig. 3.2b, $\rho(x) = \rho_0 + \rho_1 \cos(2k_{\mathrm{F}}x + \phi)$, where $\lambda_{\mathrm{CDW}} = 2\pi/k_{\mathrm{F}}$). This spatial modulation of charge density also accompanies its corresponding lattice distortion with the periodicity of $\lambda_{\mathrm{CDW}} = 2a$. Therefore, the STM topographic and spectroscopic measurements will reveal the spatial modulation and electronic characteristics, respectively.

Fig. 3.3 shows an atomically resolved topographic image of $NbSe_2$ in a flat area of 10×10 nm^2 at 4.2 K. One can clearly see the spatial modulation due to the CDW, showing that every third atom appears brighter than the other two in a given row of atoms. This modulation is commensurate with the underlying atoms of $NbSe_2$. The unit cell of the CDW forms a 3×3 superstructure (Fig. 3.6) in addition to the atomic structure. Precisely, this topography shows the superposition of both atomic and CDW signatures.

Together with the topographic data, I took point spectroscopic measurements

at four different places in the area. By averaging over four traces of dI/dV, I found

two gaps of $\Delta_{\text{CDW}} \approx 35$ mV and $\Delta_{\text{SC}} \approx 5$ mV (Fig. 3.4). The Δ_{SC} is broader than

the well known gap energy of ≈ 1 mV in NbSe$_2$ [20], because the energy resolution

of 2 mV/pt used in the dI/dV was too large to resolve such a narrow gap. However,

this coarse measurement clearly shows the coexistence of superconducting and CDW

states at 4.2 K below T_c^{SC} and T_c^{CDW}.

To exclusively resolve the superconducting gap better than 2 mV/pt, I carried

out another spectroscopic measurement below 4.2 K. Although our LT-STM was

designed to operate at the liquid helium temperature, the dI/dV measurement was

achieved by pumping the bath space of the dewar. After the dewar was fully filled

with liquid helium, overnight pumping lowered the temperature from 4.2 K to $\approx$

2 K. Fig. 3.5 shows the spectroscopic measurements taken at six different places at

2 K. Here, the energy resolution of 40 μV/pt used was good enough to resolve the

superconducting gap of $\Delta_{\text{SC}} = 1.6$ mV.
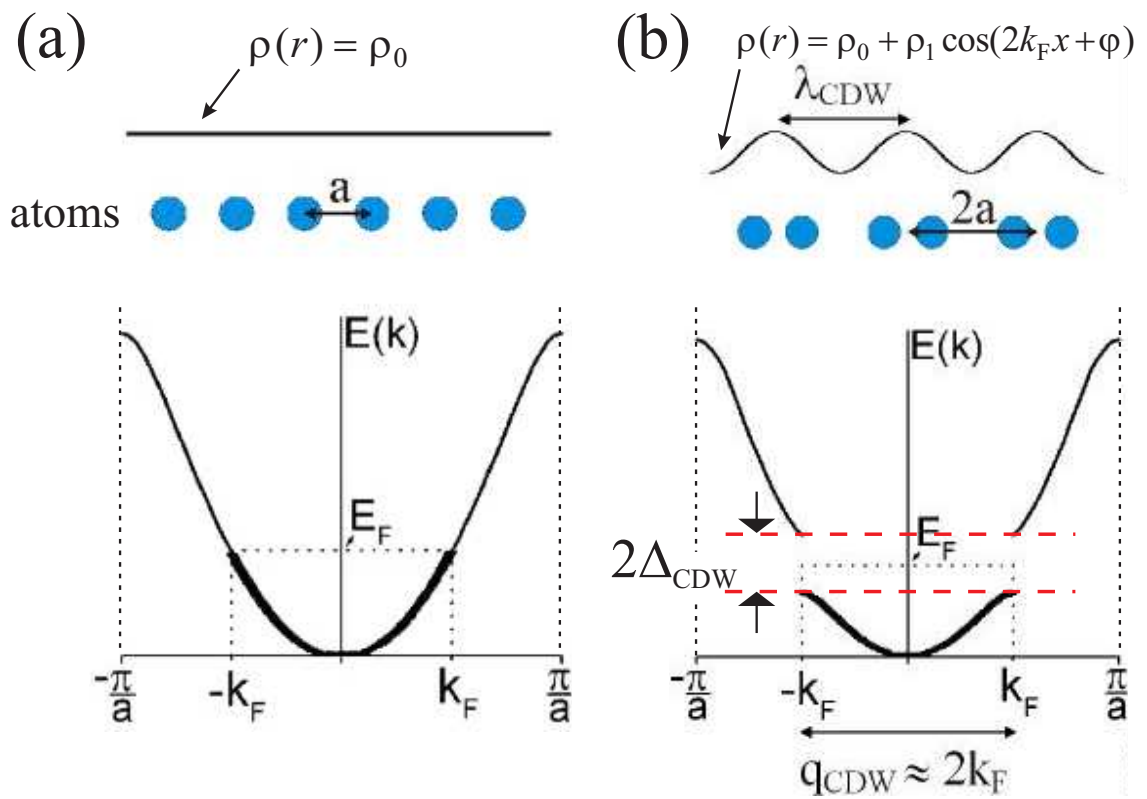
Figure 3.2: **1-D Charge density wave. a) Undistorted metal. b) Peierls insulator.** Adapted from Ref. 21.
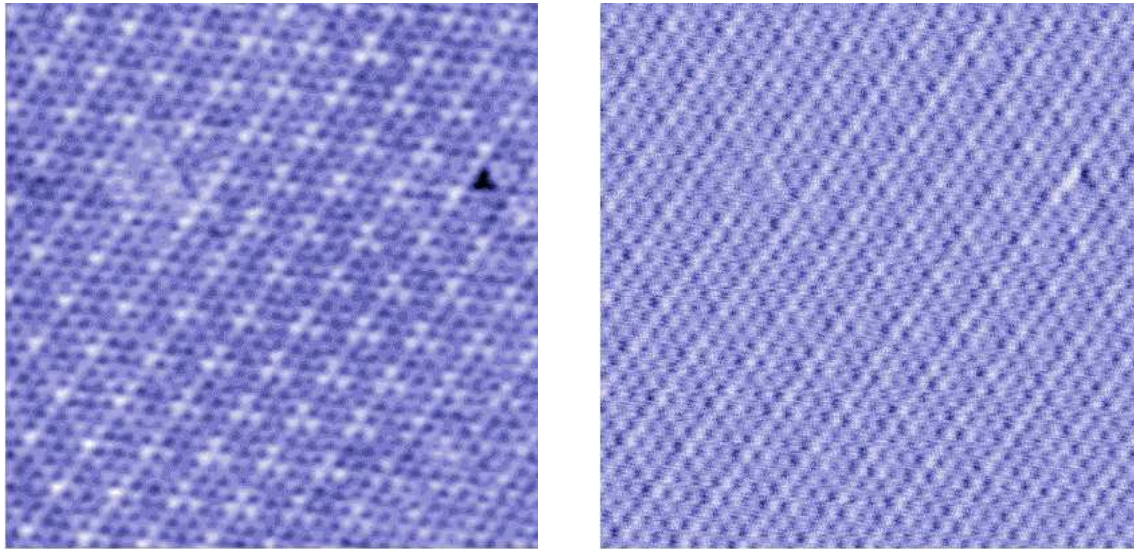
(a) Height   (b) Current

Figure 3.3: **Atomically resolved topography of NbSe$_2$ at 4.2 K.** This topography over 10×10 nm^2 shows the superposed information of atoms and 3×3 charge density waves in NbSe$_2$. $I = 0.1$ nA, $V = 35$ mV.
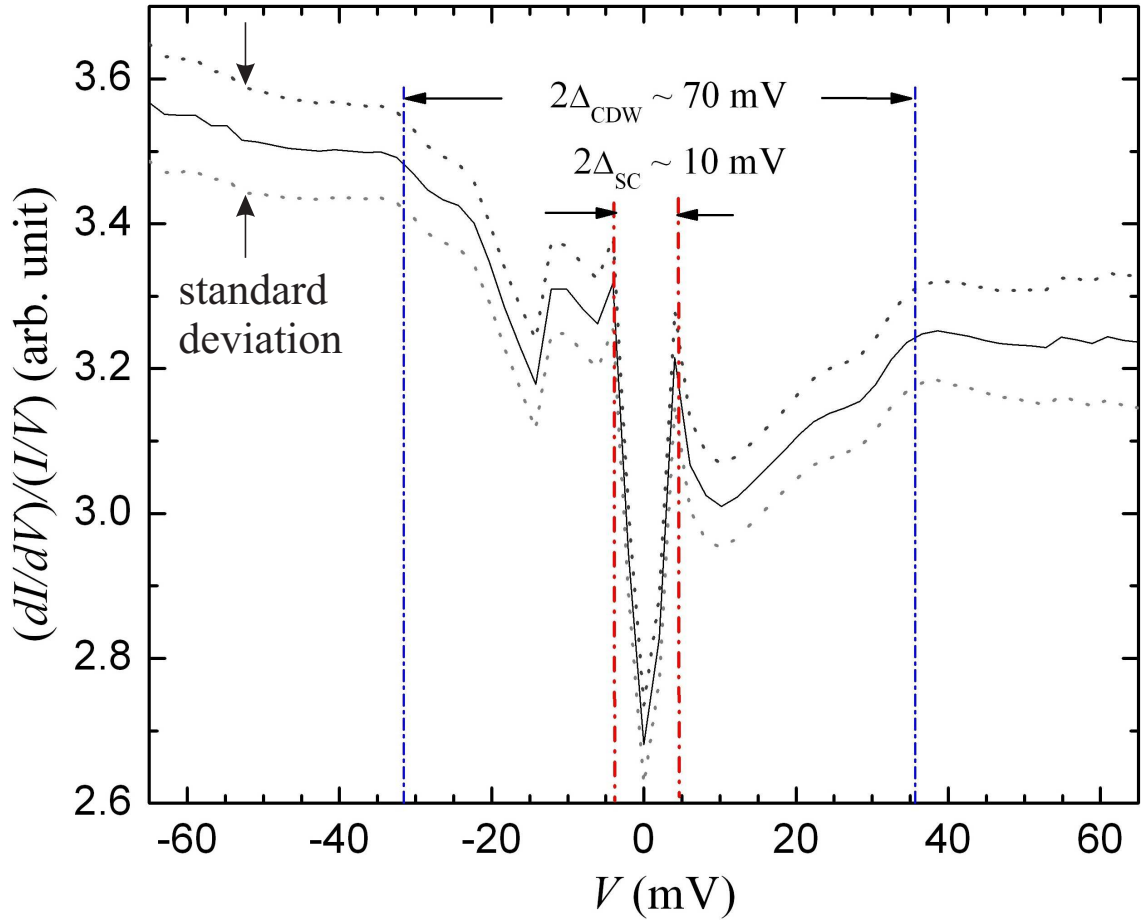
Figure 3.4: **Coexistence of charge density wave & superconductivity.** This plot was averaged over four different measurements of dI/dV at 4.2 K with an energy resolution of 2 mV/pt. and $V_{\mathrm{mod}} = 1$ mV. Tunneling conditions of $I = 0.4$ nA and $V = 35$ mV were used.
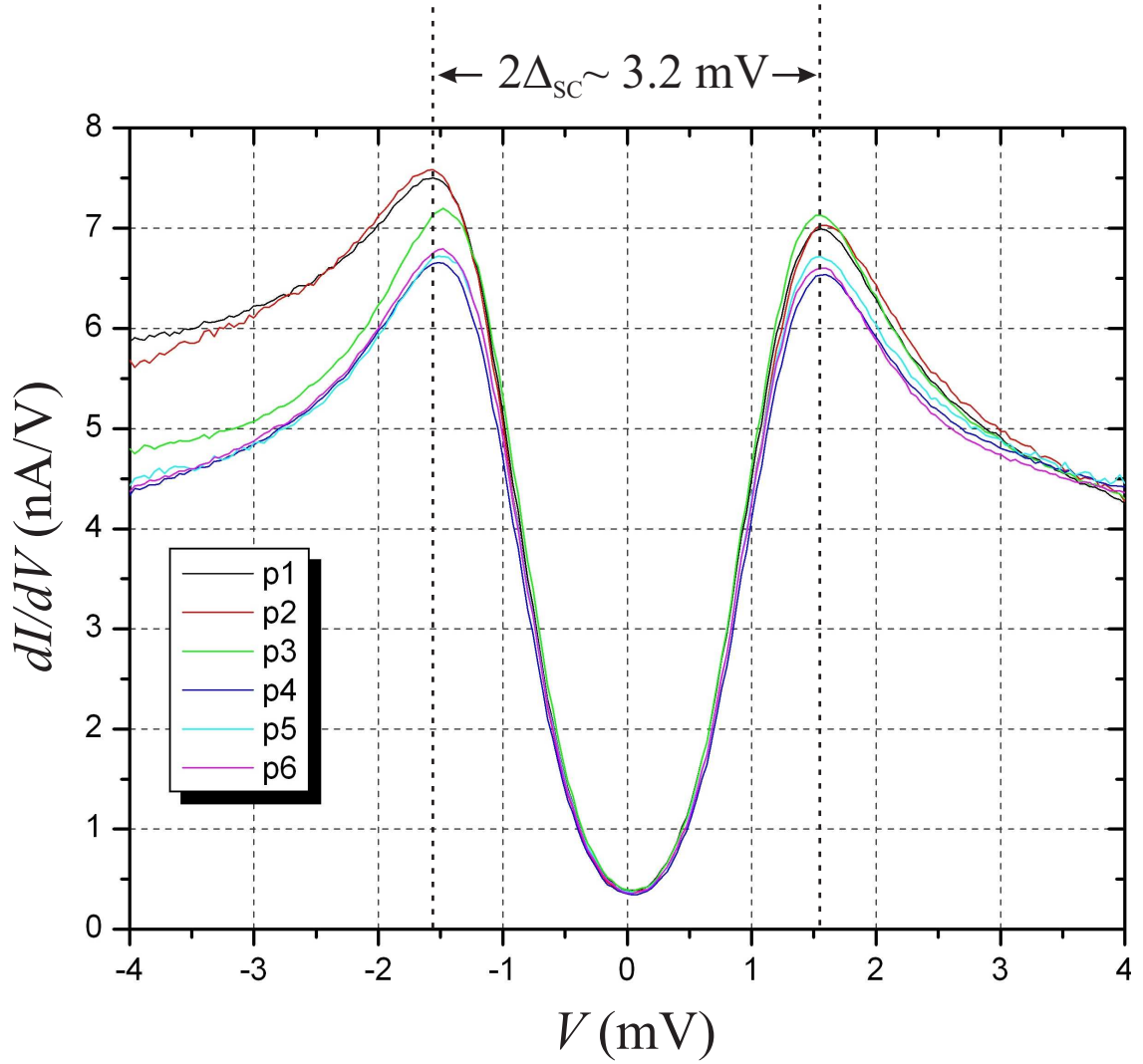
Figure 3.5: **Superconducting gap at ≈ 2 K.** dI/dV measured at six different locations with an energy resolution of 40 μV/pt. and $V_{\mathrm{mod}} = 38$ μV. Tunneling conditions of $I = 1$ nA and $V = 4$ mV (p1, p2, p3) or $V = -4$ mV (p4, p5, p6) were used.

3.3 Deliberate Surface Modification: $\sqrt{13}\times\sqrt{13}$ & Amorphous Phases

The previously described 3×3 superstructure is one type of CDW of NbSe$_2$, which naturally occurs below $T_c^{\text{CDW}} = 32$ K. However, depending on the details of strain in the material, one may also observe a CDW-like phase [24,25]. For example, Koslowski *et al.* [24] observed the $\sqrt{13} \times \sqrt{13}$ CDW-like phase in Ag-intercalated NbSe$_2$ (see Fig. 3.6 for the unit cells of 3×3 CDW phase and $\sqrt{13} \times \sqrt{13}$ CDW-like phase). Komori *et al.* [25] found two phases of 3×3 and $\sqrt{13} \times \sqrt{13}$ in pure NbSe$_2$. The $\sqrt{13} \times \sqrt{13}$ phase is believed to originate from an introduction of new layer stacking. However, it is not fully understood at this stage. In this section, instead of discussing what causes this CDW-like phase, I will demonstrate a method of introducing not only 3×3 and $\sqrt{13} \times \sqrt{13}$ but also an amorphous phase by deliberately modifying the surface of NbSe$_2$ *in situ*.

Fig. 3.7 shows a snapshot of the modified surface of NbSe$_2$ at 4.2 K. This modification was realized using the following procedure. First, scan over an area with typical tunneling condition of $I \sim 0.1$ nA and $V = 10 - 500$ mV. Second, change the bias voltage to $\sim 2 - 10$ V. This step causes the surface to be damaged and leaves a large pit ($\varnothing\ 150 - 300$ nm and 100 nm deep). Lastly, move the tip away from the center of the surface damaged area to avoid possible tip damage. This procedure caused two more phases (B, C) in addition to the original phase (A).

The most damaged area, close to where the bias voltage change was applied, shows the amorphous phase. The $\sqrt{13} \times \sqrt{13}$ phase appears in the area between the amorphous and 3×3 phases. In this area, there appear two different domains

of $\sqrt{13} \times \sqrt{13}$ CDW-like phase (yellow lines) and missing defects. The undamaged area shows the original 3×3 phase. Fig. 3.8 shows the zoomed-in view of an area of 15×15 nm^2, where the boundary between 3×3 and $\sqrt{13} \times \sqrt{13}$ exists. Since the corrugation of $\sqrt{13} \times \sqrt{13}$ overwhelms that of 3×3, one can not clearly see the atoms in the 3×3 phase area.

In contrast to previous work done by other groups, our method should be distinguished for the following reasons. First, our method can be used *in situ* to introduce three different phases of CDW and CDW-like together. Second, this is the first observation of the amorphous phase in NbSe$_2$, to the best of my knowledge. Furthermore, this method can be utilized to investigate the competition between superconductivity and charge density waves [26–30] in STM experiments.
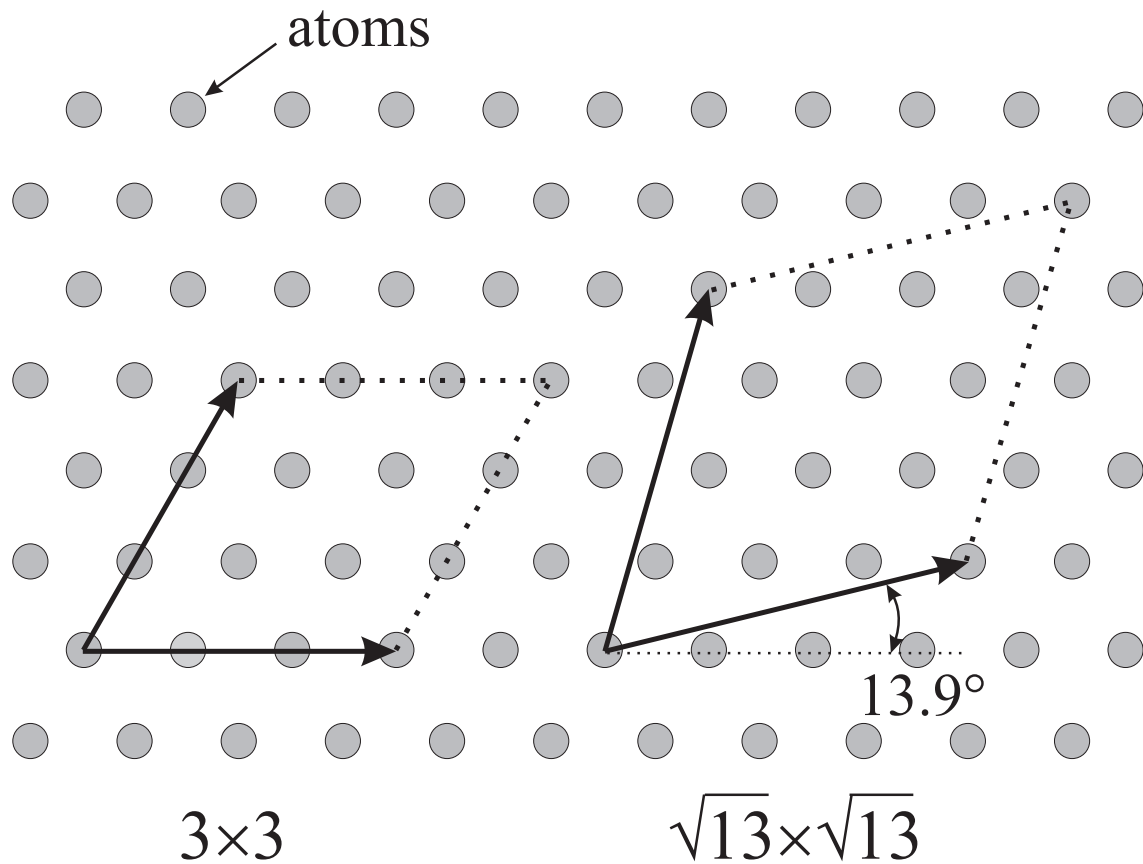
Figure 3.6: **Unit cells of CDW and CDW-like phases.** The 3×3 CDW phase (left) is commensurate with the underlying atoms, while the $\sqrt{13} \times \sqrt{13}$ CDW-like phase is incommensurate.
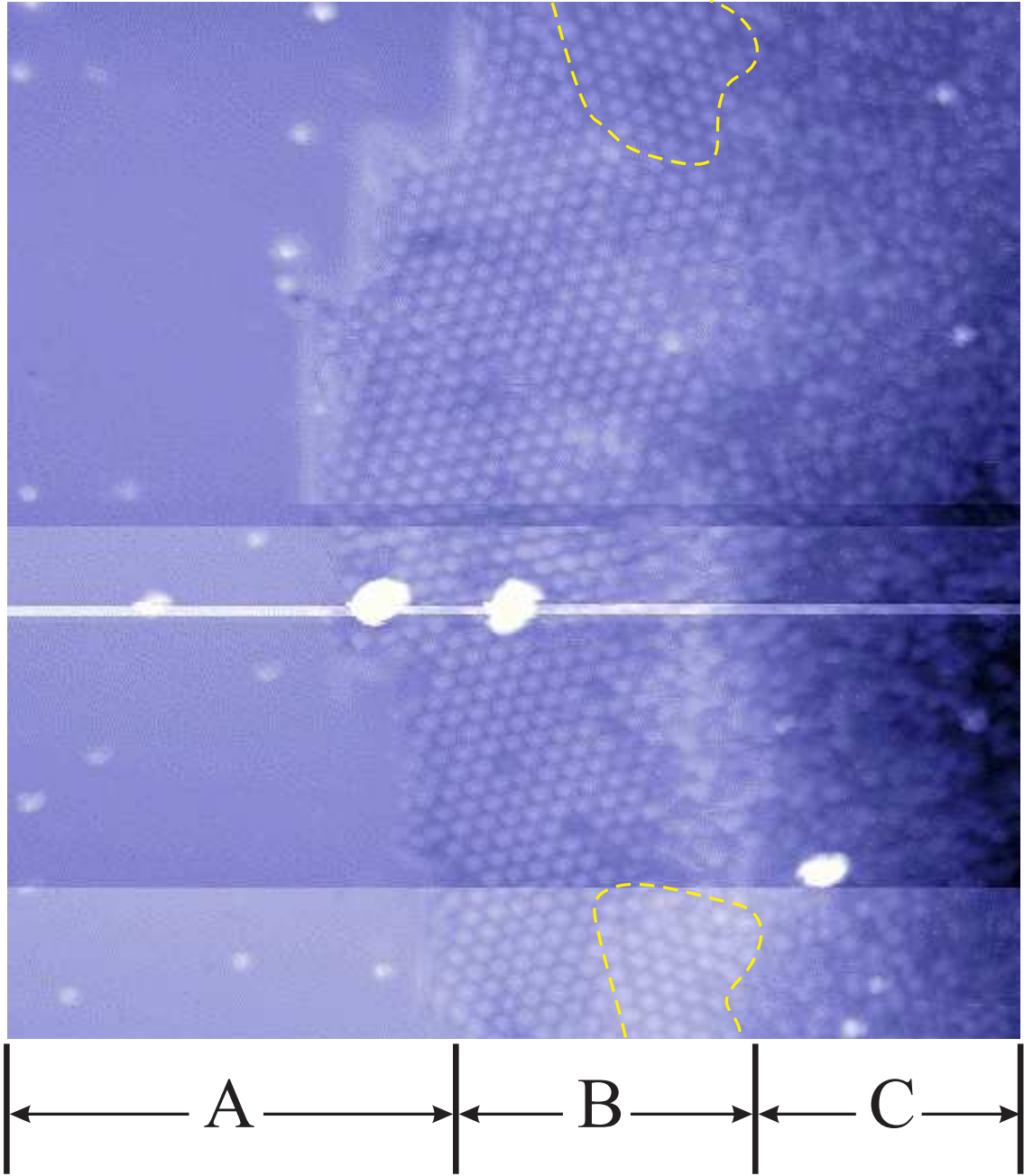
Figure 3.7: **Topography around a pit.** This topography over 60×60 nm^2 shows 3×3 CDW (A), $\sqrt{13} \times \sqrt{13}$ CDW-like (B), and amorphous (C) regions together. In the region where the $\sqrt{13} \times \sqrt{13}$ CDW-like phase exists, there are two different domains. The domain boundaries are marked by yellow dash lines.
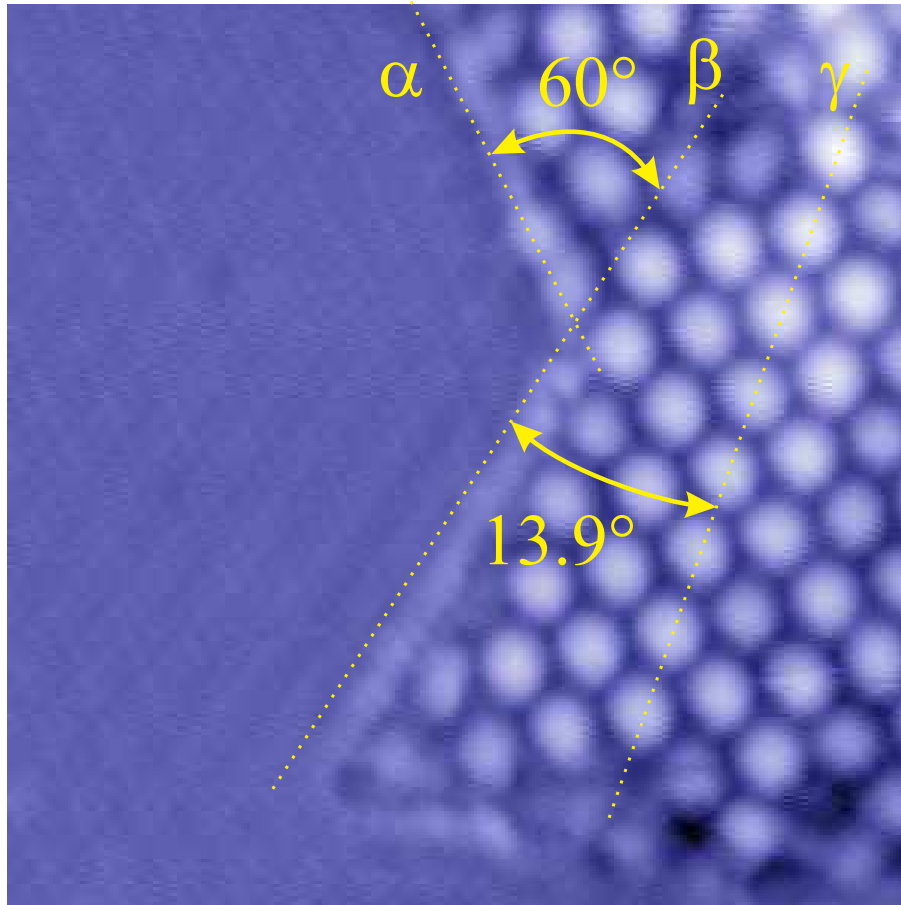
Figure 3.8: **The phase boundary of** 3×3 **&** $\sqrt{13} \times \sqrt{13}$ **phases.** 15×15 nm^2, $I = 0.15$ nA, $V = 100$ mV. The phase boundary formed along the principle axes of the underlying atoms and the 3×3 superstructure ($\angle\alpha\beta = 60°$). The orientation of the $\sqrt{13} \times \sqrt{13}$ superstructure is rotated by $13.9°$ ($\angle\beta\gamma$)with respect to the underlying atomic symmetry as Fig. 3.6 suggests.

Chapter 4

Overview of Vortex Dynamics

4.1 Introduction

This chapter contains a brief overview of vortex dynamics of type II supercon-ductor before I present and discuss the motion of vortices in Chapter 5. When we were investigating the LDOS of pristine NbSe$_2$ under magnetic fields, we observed the signature of moving vortices (Fig. 5.1b). This observation became the most intriguing subject in this Thesis. Therefore, the following introduction of vortex dynamics can be helpful in reading the next chapter. I will cover the basics of driv-ing mechanism of vortices, the factors which impede the motion, and the different regimes of vortex dynamics.

4.2 Abrikosov Lattice

When a magnetic field is applied to a type II superconductor, a filamentary magnetic field threads the superconductor (Fig. 4.1). The flux of each threaded magnetic field amounts to $\Phi_0 = 2.068 \times 10^{-15}$ Tm^2 (magnetic flux quantum). The superconductivity is suppressed within a radius ξ (coherence length), where normal electrons reside (normal core). Around the normal core, supercurrents circulate up to a distance, λ (London penetration depth). This structure is called a vortex.

Vortices of the same handedness (defined by direction of supercurrents) repel one another, and screening currents along the edge of a superconductor prevent vortices from leaving the sample (Fig. 4.2). As a result, vortices form a triangular lattice, which is energetically favorable away from the edge, with a lattice constant of

$$a(B) = \left(\frac{2}{\sqrt{3}} \right)^{\frac{1}{2}} \left(\frac{\Phi_0}{B} \right)^{\frac{1}{2}} \, , \tag{4.1}$$

where B is the magnetic field in the superconductor[1]. This lattice is called Abrikosov lattice [22] (often vortex lattice (VL) or flux line lattice (FLL) in the literature).

The VL is a good model system in condensed matter physics. Its lattice constant is highly tunable by adjusting the magnitude of an external field. Under external forces caused by magnetic field gradients, thermal activation, or transport currents, the VL shows rich dynamics and phases [31–33].

When vortices start moving, the normal electrons in the core dissipate heat, which can destroy the superconducting property. Therefore, from a technical point of view, preventing the motion of vortices plays a key role in developing a superconductor with a high critical current density. To achieve this goal, understanding the nature of vortex dynamics is essential.

---

[1]I would like to point out that B is not the applied (external) magnetic field. It is the field inside a material (the superconductor, in this case).
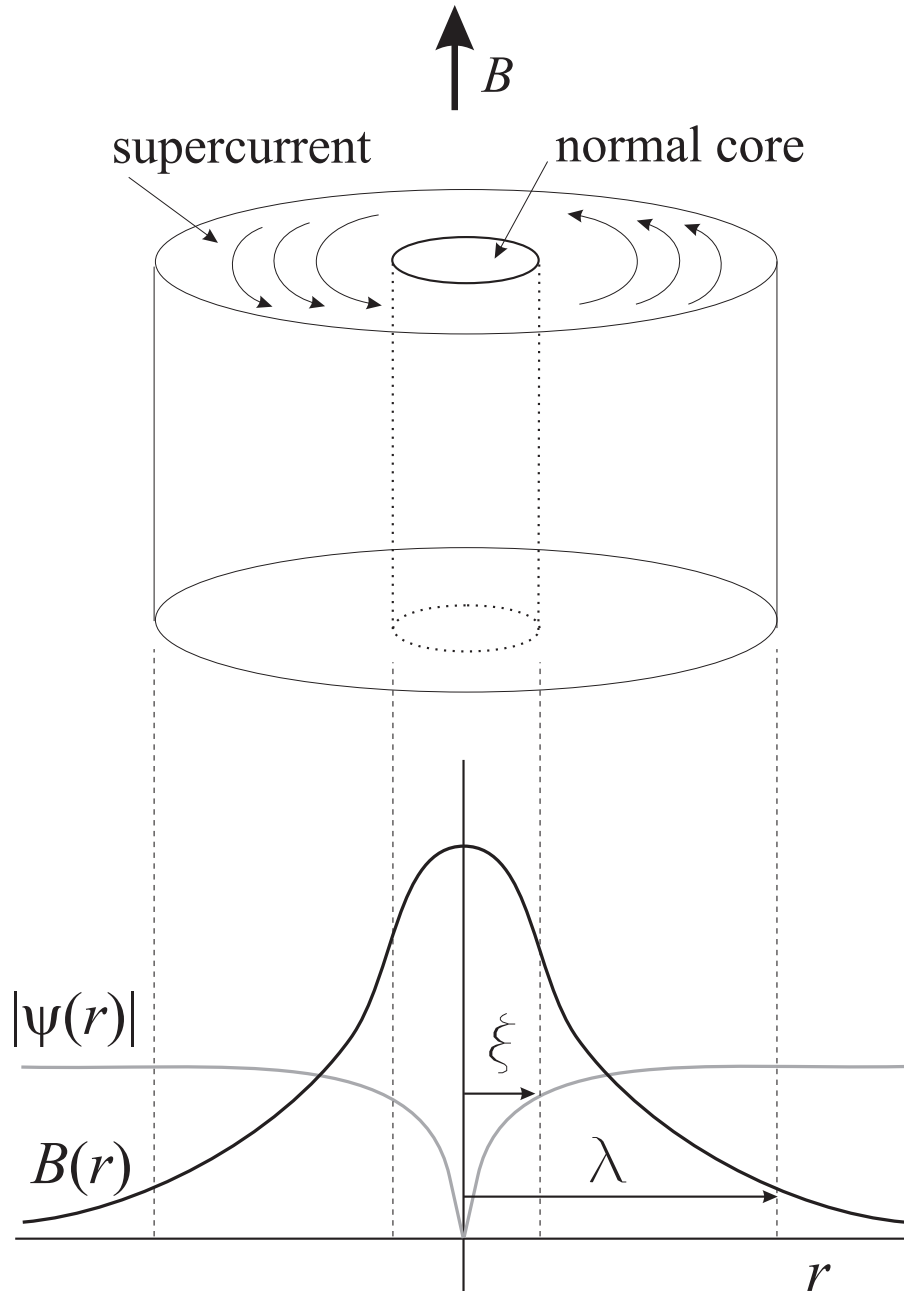
Figure 4.1: **Vortex structure. Top.** A vortex consists of a normal core and superconducting region where supercurrents circulate. **Bottom.** $\psi(r)$ $(= \sqrt{n_s})$ and $B(r)$ are the measure of superconductivity (called Ginzburg-Landau order parameter [34]) and the magnetic field of the vortex at a distance of r away from the center of the core, respectively, where n_s is the density of Cooper pair electrons.
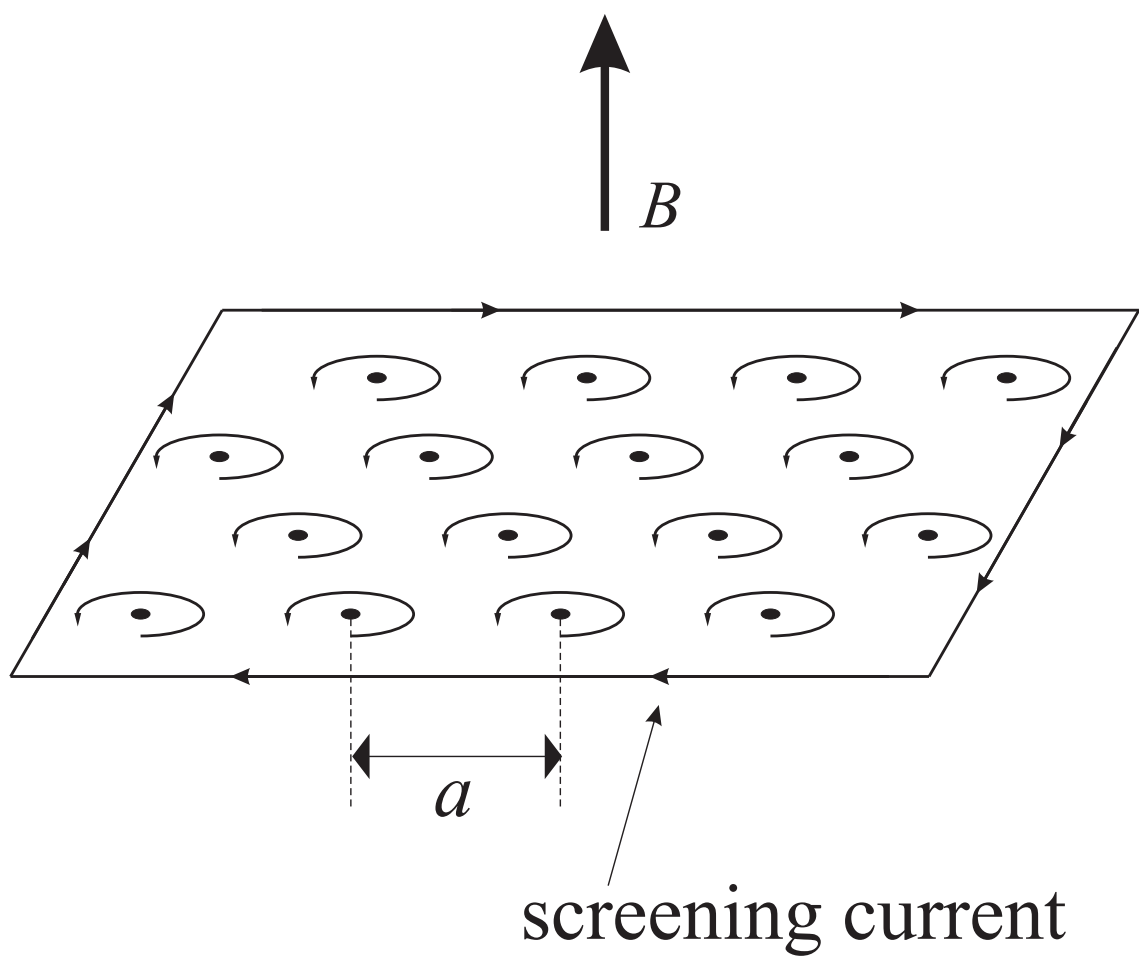
Figure 4.2: **Abrikosov lattice.** Vortices form a triangular lattice within a type II superconductor by their repulsions and the confining force due to the screening current along the edge.

4.3   Vortex Motion: Current as a Driving Source

When a current density of $\vec{J}$ flows through the superconductor, a force per unit length

$$\vec{f_{\mathrm{v}}} = \vec{J} \times \Phi_0 \cdot \hat{n} \, , \tag{4.2}$$

is exerted on a vortex line, where $\hat{n}$ is the unit vector of $\vec{B}$ and $[f_{\mathrm{v}}] = \mathrm{N/m}$. Macroscopically the force per unit volume becomes

$$\vec{f} = \vec{J} \times \vec{B} \, . \tag{4.3}$$

In fact, $\vec{J}$ can be the sum of transport currents and suppercurrents around vortices. Without a transport current, the force due to supercurrents becomes zero, because of the symmetry of the VL. However, if there is a magnetic field gradient in the superconductor, the induced current ($\vec{J} = \nabla \times B$) exerts a non-zero force on the vortices.

In most literature and textbooks of superconductivity, this force is called the Lorentz force. However, this should be distinguished from the Lorentz force which is exerted on a charged particle when it moves in an external magnetic field. Indeed, in superconductivity, the Cooper pair electrons flow, avoiding the normal core region where most of the magnetic field is concentrated. More precisely, this force is analogous to the Bernoulli force of the hydrodynamics of superfluids (Chris Lobb, Private communication, 2006). In this Thesis, I call it a Lorentz-like force.
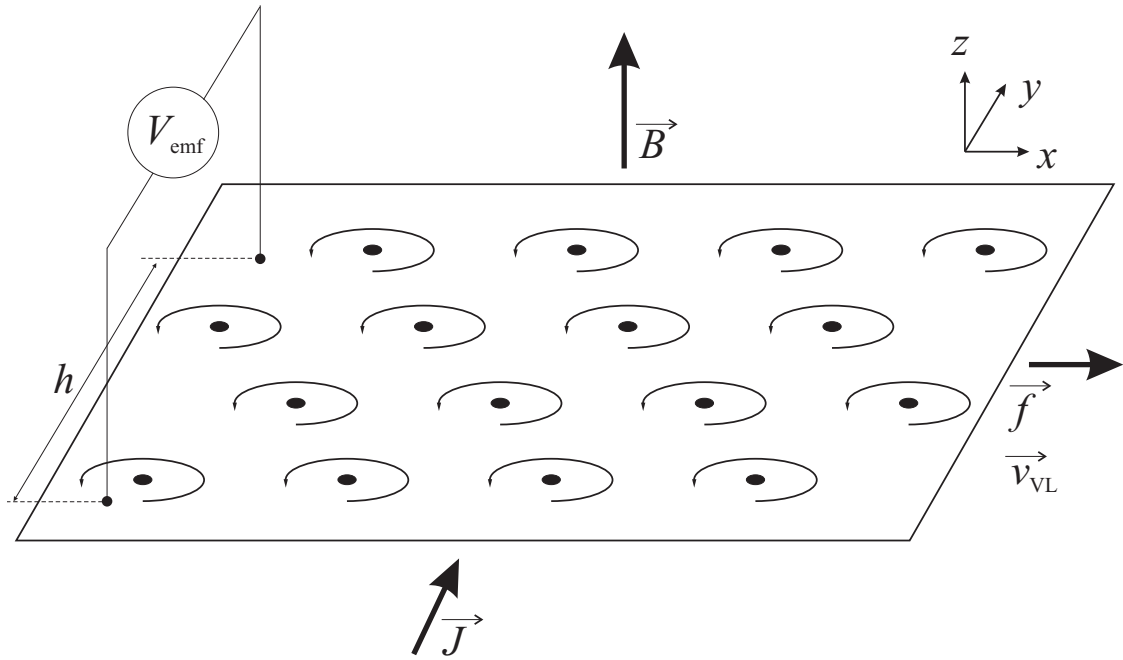
Figure 4.3: **Lorentz-like force.** The current density of $\overrightarrow{J}$ induces a force of $\overrightarrow{f} = J \cdot \hat{y} \times B \cdot \hat{z} = f \cdot \hat{x}$ on the VL, perpendicular to the directions of $\overrightarrow{J}$ and $\overrightarrow{B}$. The motion of the VL at $\overrightarrow{v_{\mathrm{VL}}}$ due to $\overrightarrow{f}$ induces the electromotive force (EMF) of $V_{\mathrm{emf}} = h \cdot \left| \overrightarrow{E} \right|$, parallel to $\overrightarrow{J}$, where $\overrightarrow{E} = \overrightarrow{B} \times \overrightarrow{v_{\mathrm{VL}}}$.

4.4 Pinning in General

When vortices are moving, the motions of vortices are impeded by defects in a non-ideal type II superconductor. The defects are called pinning centers, which cause local variation of critical temperature, coherence length, and the London penetration depth of the superconductor [35]. As a result, pinning centers induce forces on vortices, which are called pinning forces.

Pinning centers can be any imperfection of a superconductor, including vacancies, voids, steps, grain boundaries, dislocations, and precipitates. The theoretical analysis of flux line pinning, as Brandt [36] explained, consists of two problems. One is the calculation of the elementary pinning force between the vortex lines and a given pinning center. The other is the statistical summation of these forces to achieve an average force per unit volume. To solve the first problem, one has to know microscopic information about a given pinning center such as its strength and range. Moreover, the actual size of a defect does not necessarily coincide with that of its pinning range [37]. As for the second problem, one has to know the elastic and plastic properties of the VL [38], which depends on many parameters including temperature, magnetic field, the geometry of the sample, *etc.*

4.5 Critical Current as a Measure of Pinning Force

Experimentally, the critical current density is one measure of the pinning force. When a non-zero external current density flows in the superconductor, the Lorentz-like force (Eq. 4.2) acts on a vortex line. However, because there exist pinning force

which balances the Lorentz-like force, the vortex does not move until the Lorentz-like force exceeds the pinning force such that $\left|\vec{f_L}\right| > \left|\vec{f_p}\right|$. Therefore, the critical density $(\vec{J_c})$ satisfies the condition of

$$\left|\vec{J_c} \times \Phi_0 \cdot \hat{n}\right| = \left|\vec{f_p}\right| . \tag{4.4}$$

Once the vortex starts moving, an additional drag force acts on the vortex. The total force exerted on the vortex line is

$$\vec{f}_{tot} = \vec{f_L} + \vec{f_p} + \vec{f_d} . \tag{4.5}$$

Substituting $\vec{J} = J \cdot \hat{y}$, $\vec{\Phi_0} = \Phi_0 \cdot \hat{z}$, and $\vec{f_p} = -f_p \cdot \hat{x}$ into Eq. 4.5, one finds

$$f_{tot} = J \cdot \Phi_0 - f_p - \eta \cdot v_x , \tag{4.6}$$

where η is the drag coefficient. In the steady state $(f_{tot} = 0)$,

$$v_x = \frac{1}{\eta}(J \cdot \Phi_0 - f_p) \tag{4.7}$$

for $J > J_c$. For $J \le J_c$, the velocity becomes zero. One can rewrite Eq. 4.7 as

$$v_x = \frac{\Phi_0}{\eta}(J - J_c) . \tag{4.8}$$

According to the Faraday's law, the voltage developed along the direction of $\overrightarrow{J}$, induced by the moving vortices, becomes

$$V_{\text{emf}} = \frac{d\Phi}{dt} = \Phi_0 \cdot n \cdot h \cdot v_x, \tag{4.9}$$

where $n = B/\Phi_0$, and h is the length to the current flow (Fig. 4.3). Using the expression of

$$\eta = \frac{\Phi_0^2}{2\pi\xi^2}\sigma_0 \ , \tag{4.10}$$

where σ_0 is the normal conductivity39, Eq. 4.9 becomes

$$V_{\text{emf}} = (i - i_c) \cdot R_{ff} \tag{4.11}$$

$$= (J - J_c) \cdot \rho_{ff} \cdot h, \ , \tag{4.12}$$

where R_{ff} is the flux flow resistance when there is no pinning. Eq. 4.11 and Eq. 4.12 imply that the voltage should remain zero until the current exceeds the critical current (Fig. 4.4a). After a voltage has developed for $i > i_c$ ($J > J_c$), the slope of V vs. i (J) is same as that when there is no pinning. However, the real plot shows a nonlinear, non-zero behavior below i_c (Fig. 4.4b). As i increases from zero, first thermally activated vortex motion comes into play. Then the motion enters the flux creep regime. This thermally activated flux flow (TAFF) and flux creep (FC) regime has drawn new attention, since high temperature superconductors were discovered [40]. Due to its high transition temperature, thermal energy ($\sim$ $k_B T$, where $k_B T$, Boltzmann constant) plays an important role in explaining vortex

dynamics in these systems. In the TAFF and FC framework, the inhomogeneous magnetic field distribution due to imperfections in a real superconductor induces a current flow in the sample ($\nabla \times \vec{B} \approx \vec{J}$). This tilts the potential landscape seen by vortices. Depending on the degree of inhomogeneity and the temperature, either TAFF or FC appears.

I would like to point our that the measurement of i_c (J_c) is not an absolute measure, because different voltage criteria can be chosen. For example, the superconductivity can survive above a certain critical current criteria. In general, the common criteria is 1 μV development across 1 cm of a sample.
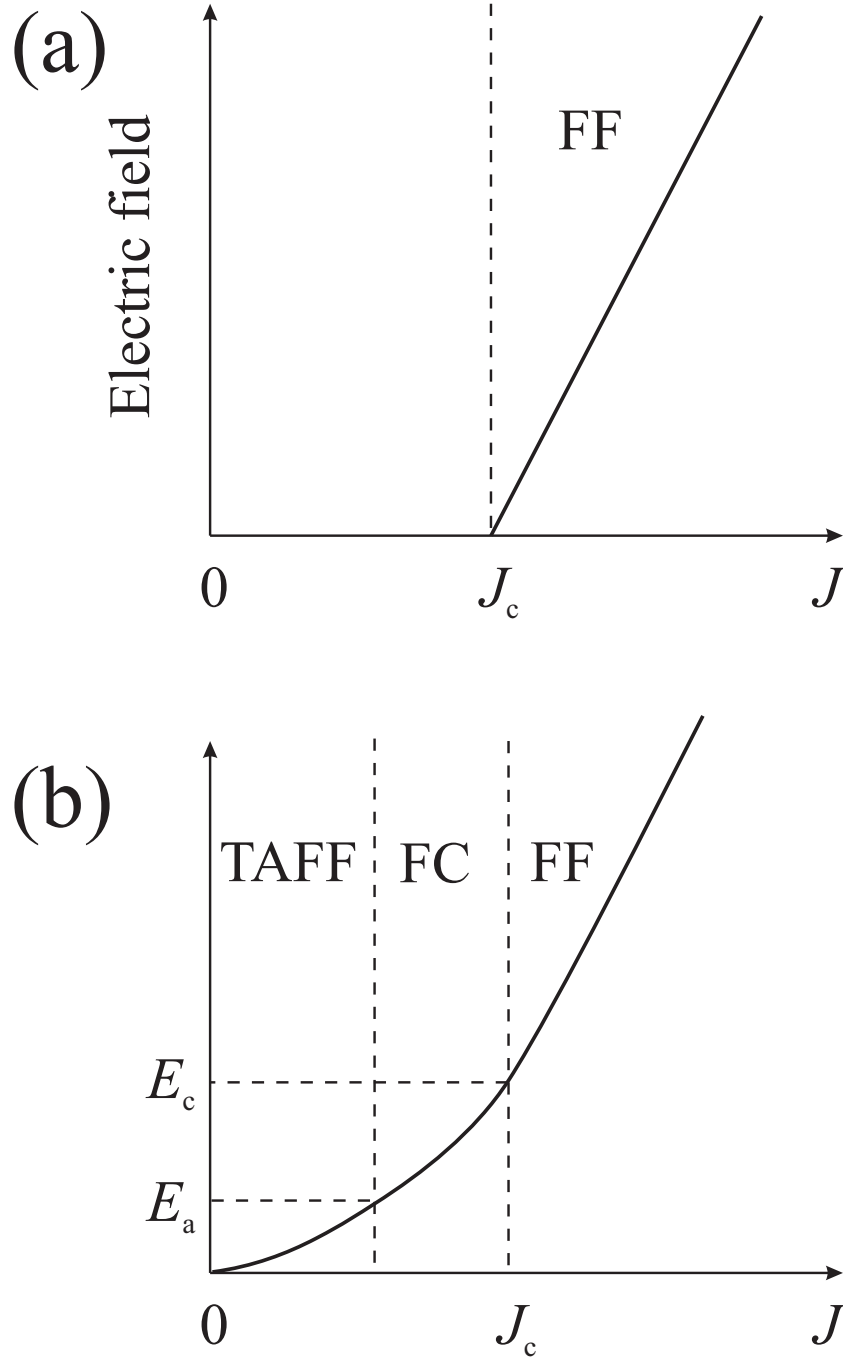
Figure 4.4: **Regimes of flux motion.** The plot of electric field (E) vs. current density (J) is used to categorize the motion of vortices. **a)** Simple flux flow model **b)** E_a and E_c are the onset fields for the flux creep and flux flow regimes, respectively. Adapted from Ref. 35.

4.6 Collective Pinning Theory

The collective pinning theory was proposed by Larkin and Ovchinnikov [41] to explain the anomalous enhancement of the critical current density as a magnetic field approaches close to its critical field (called the peak effect). This theory was founded on two major concepts. One is the elasticity/plasticity of vortex lines, and the other, summation rule of randomly distributed weak pinning centers with equal strength in a superconductor.

Even with a pristine superconductor, one can not expect pinning-free conditions. First, assume that weak pinning centers are randomly distributed in the superconductor. If a vortex line is completely rigid (Fig. 4.5a), the force exerted on the vortex line becomes zero, because the force is summed over the forces by the individual pinning centers with equal strength, which are randomly distributed. In this case, the peak effect is not well explained. In addition, the motion of the rigid vortex lines are not affected by the existence of the randomly distributed pinning centers.

On the other hand, if the vortex line is elastic (Fig. 4.5b), a vortex line distortion occurs such that the restoring force of the elastic vortex line balances the pinning force. In this case, the pinning force is non-zero. Furthermore, as a magnetic field increases, the vortex line becomes softer [41]. This causes the vortex line to be pinned more effectively at nearby pinning centers. As a result, more distortion of the vortex line occurs and the pinning force increases. Therefore, the enhancement of the critical current density is observed close to the critical field.

Another interesting topic about the collective pinning theory is the order of the VL. If it is rigid, the triangular lattice is maintained. If the strength of pinning centers are weak, the long range order breaks while the short range order still exists (Fig. 4.6a). However, if the strength is too strong, no order is found (Fig. 4.6b)
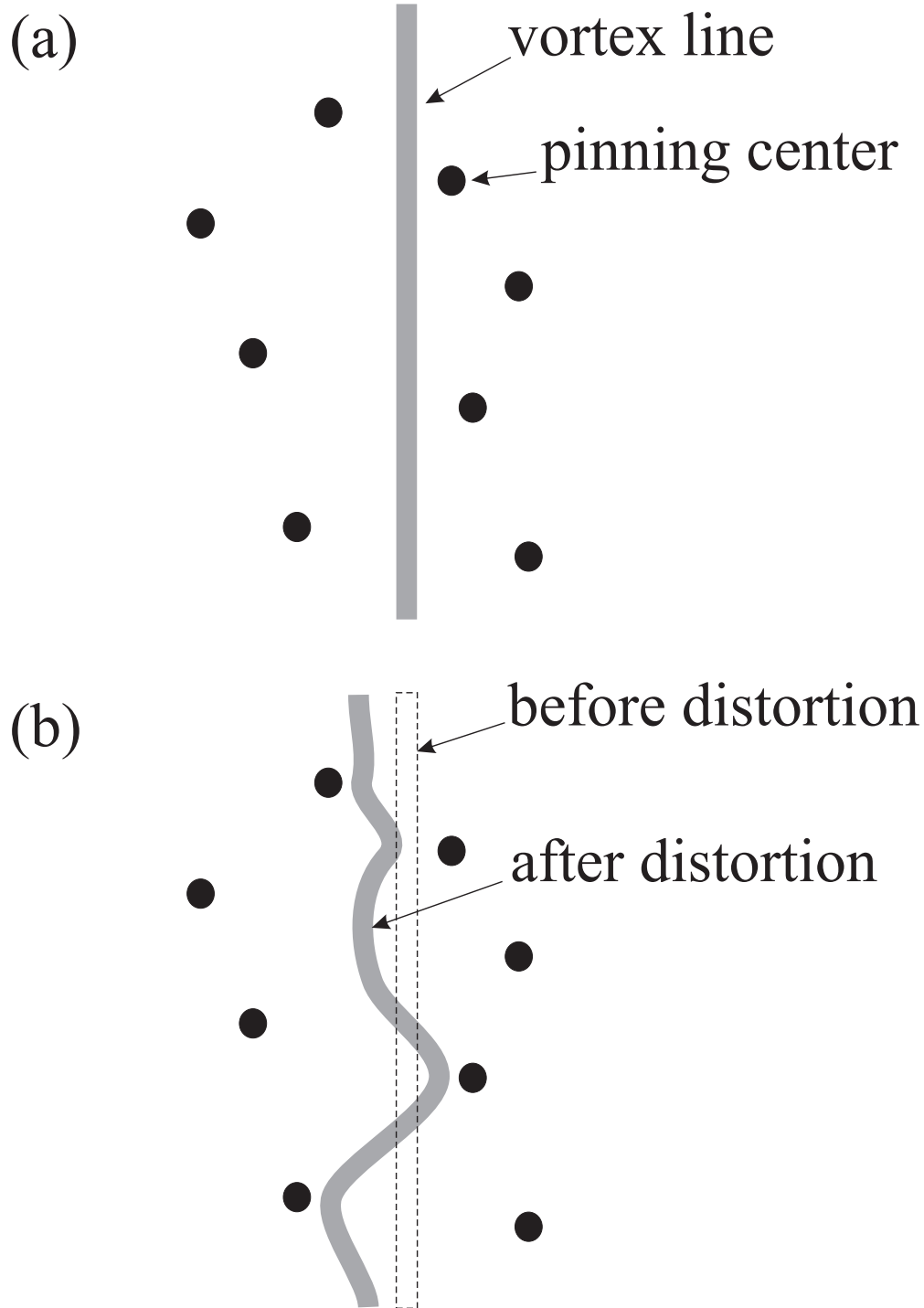
Figure 4.5: **Rigid vs. elastic vortex line.** Black dots represent randomly distributed pinning centers. **a) Rigid vortex line.** The sum of forces exerted on a vortex line by pinning centers becomes zero. **b) Elastic vortex line.** Starting with a straight vortex line (dash line), the vortex line is distorted (gray) due to the individual pinning centers. The sum of pinning forces is non-zero. The pinning forces are balanced by the restoring forces due to the elasticity of the vortex line.
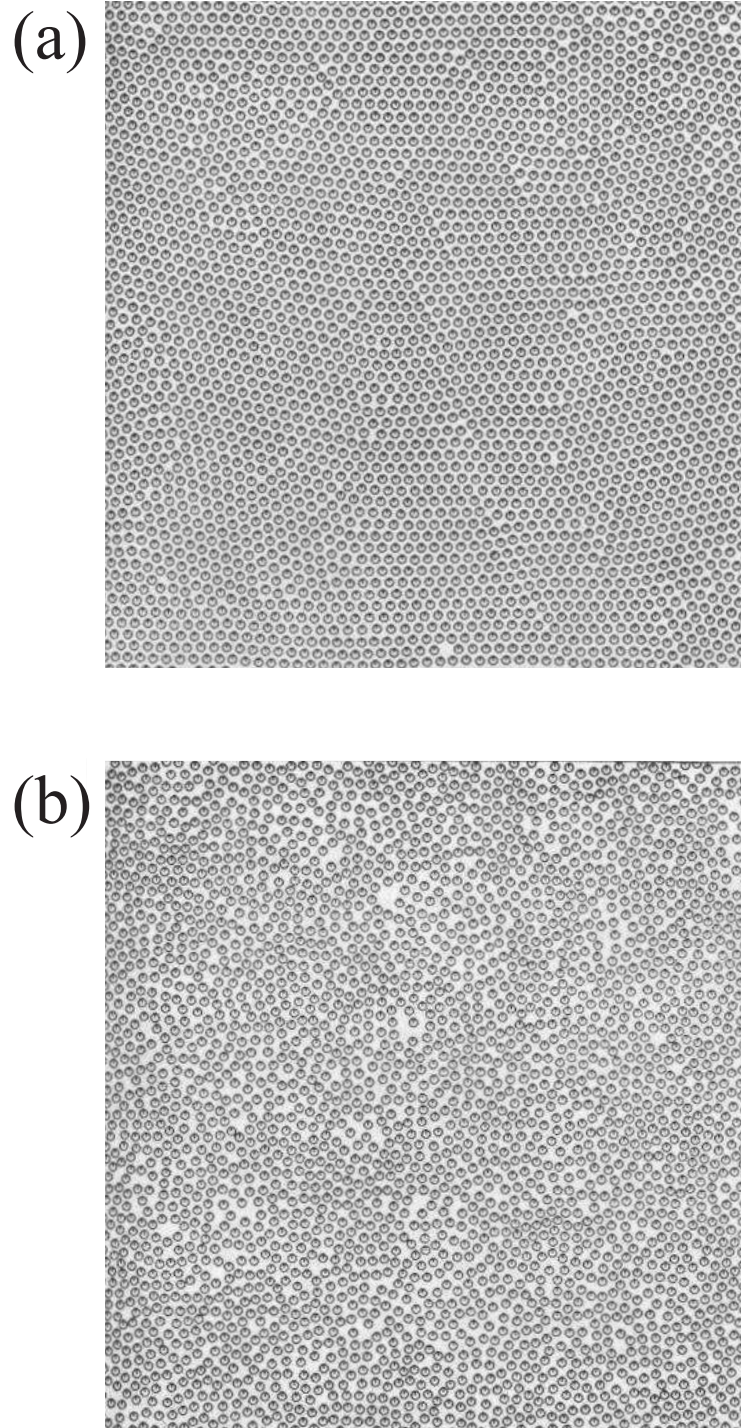
Figure 4.6: **Weak vs. strong random pinning potentials.** Random pinning potential disturbs the arrangement of vortices. **a) Weak pinning.** The long range order of the VL is broken while the short range order still exists. **b) Strong pinning.** No order of the VL is found. Adapted from Ref. 36.

4.7 Surface Barriers

Other than bulk pinning centers, there is another factor to be considered in vortex dynamics. Due to the existence of surface barriers along the edge of a superconductor, the motion of vortices are impeded when they enter or exit the sample. The existence of the surface barriers was initially stimulated by a magnetization measurement done by Livingston [42]. In his report, even well-annealed single crystals of type II superconductors showed a low-field hysteresis. To explain this phenomenon, C. P. Bean and J. D. Livingston proposed a "surface barrier" by using a semi-infinite type II superconductor as a model [43]. Often this barrier is called the Bean-Livingston surface barrier.

The Bean-Livingston surface barrier summarizes two concepts, which are caused by the discontinuity of a type II superconductor. One is the image force of a vortex, which is attractive toward the boundary (Fig. 4.7a). The image of the vortex is required to satisfy the requirement that the current normal to the boundary should be zero. The other is the external field (Fig. 4.7b), which induces the screening current along the boundary of the superconductor. This screening current at the boundary is repulsive to the vortex. The sum of these attractive and repulsive forces results in a repulsive force at a non-zero external field, because the repulsive term dominates over the attractive one [43].

Although the framework of the Bean-Livingston surface barrier deserves credit for first emphasizing the important role of the boundary, the semi-infinite superconductor does not fit with the real geometry of a superconductor. Furthermore, this

framework only deals with a single vortex. Realistically, a superconductor has a finite geometry and the interactions among vortices should be considered to better explain the vortex dynamics.

For realistic samples, several barrier terms must be included. "Edge barrier" [44] is used in low-dimensional superconductors, in which the thickness of a superconductor is less than the London penetration depth. "Surface barrier" [45] is used in bulk superconductors. Sometimes, "geometrical edge barrier" [46] is used to emphasize the origin of the barriers. Often the Bean-Livingston, surface, edge, and geometrical barriers are used in the literature without strict distinctions. Mathematically speaking, this involves a boundary value problem of electromagnetism and the London equation or Ginzburg-Landau equations for a superconductor. A rigorous theoretical discussion of surface barriers is beyond the scope of this Thesis.
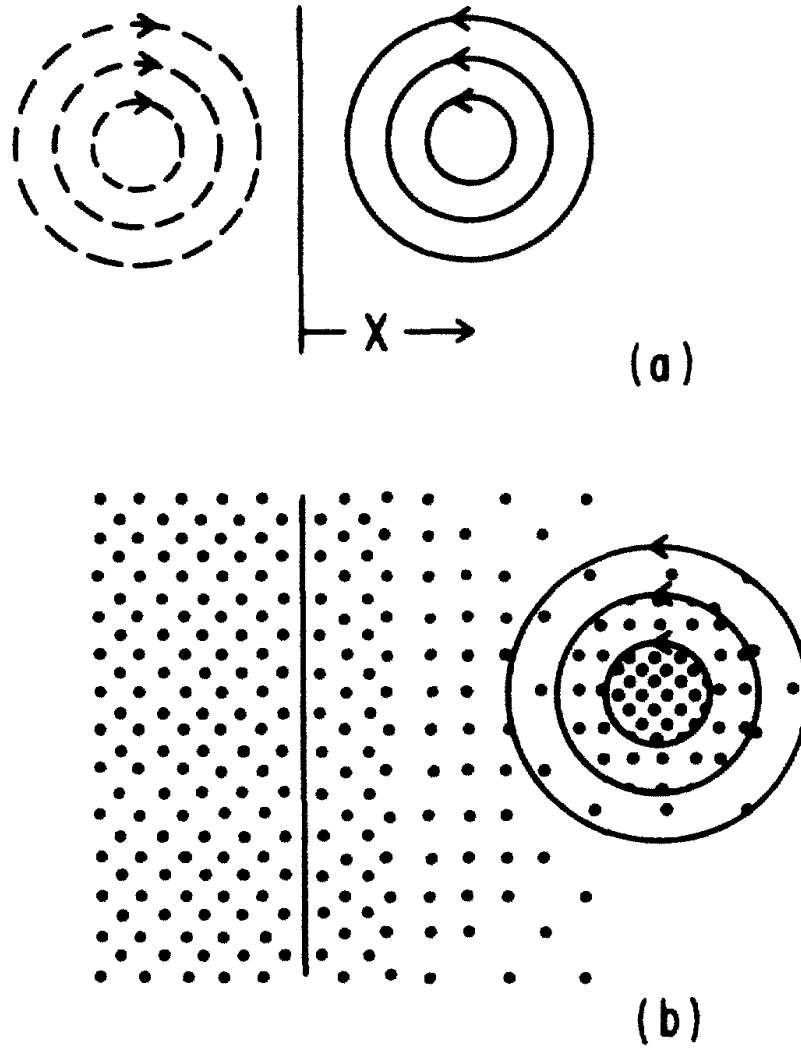
Figure 4.7: **a)** Attractive force due to image to satisfy boundary condition. **b)** Repulsive force due to interaction with surface field. Dots represents the density of local field. Adapted from Ref. 43.

4.8 Conclusion

Since understanding the nature of pinning is directly related to developing a superconductor with high critical current density, extensive theoretical and experimental work has been carried out for the last several decades. However, despite long and extensive efforts made as of today, there are still many unsolved problems in vortex dynamics. Most experimental studies about the interactions between vortices and pinnings were done by transport, magnetization, neutron scattering, *etc.*, which lead to different interpretations of the experimental results. Therefore, detailed studies on the microscopic level are necessary to properly interpret the macroscopic observations.

The basic concept for a microscopic investigation is to study the motion of individual vortices as their motion is externally driven in a controlled manner. However, most imaging techniques are limited by the optical wave length. Although Lorentz microscopy overcomes such limitations, the sample under study should be thin to achieve the visualization of vortices. To implement a driving source with a visualization instrument is also challenging. For example, to my best knowledge, no one has observed the motions of individual vortices on the nano-meter scale while applying the Lorentz-like force (Eq. 4.2 and Eq. 4.3). In other words, the Lorentz-like force has never been tested on this length scale.

In the next chapter, which is the core of this Thesis, I will show the driving mechanism, the visualization technique, and the observation.

Chapter 5

Experiment on Vortex Dynamics in NbSe$_2$

5.1   Introduction

This chapter is about the observation of moving vortices in NbSe$_2$. Moving vortices were observed when I was investigating the LDOS of this material in magnetic fields, as the last performance test of the LT-STM.

In this chapter, I will show that the motion of vortices was driven by the extremely slow decay of the magnetic field in our superconducting magnet. The scan-speed of the STM was fast enough compared to the speed of the motion of the VL. The estimated speeds of the motion were consistent with the prediction of a model based on the magnetic field decay (Fig. 5.2). Highly time-resolved data sets were produced due to the almost rigid structure of the VL during the motion, which revealed the details of the observed vortex dynamics. Furthermore, I will demonstrate that the motion can be stopped by applying an experimental procedure to the imperfect superconducting magnet. In the last of this chapter, I will discuss the possible explanation of the non-uniform motion of vortices and significance of this observation.

5.2   Evidence of Moving Vortices

After investigation of the superconducting and CDW phases without magnetic fields applied (Chapter 3), we continued to test the LT-STM by investigating this material in magnetic fields. The initial goal of this investigation was to see the internal structure of a vortex [47], and to understand how impurities affect the electronic properties, by measuring a conductance map in a given energy range.

Before taking a conductance map, I took a single layer dI/dV map over an area to confirm the existence of Abrikosov lattice in a magnetic field. Fig. 5.1a shows an Abrikosov lattice in 0.25 T at 2 K. The black regions is where normal electrons reside, and blue, where the superconducting electrons exist. However, when I carried out full conductance maps in a magnetic field of 0.25 T, I observed stretched vortices instead of a well-ordered triangular vortex lattice (Fig. 5.1b). Fig. 5.1b is one extracted layer (at $E_{\mathrm{F}} = -0.5$ meV) from many layers of the conductance map ($-5 \leq E_{\mathrm{F}} \leq +5$ meV), showing the stretched vortices in an area of 500×500 nm^2 in a magnetic field of 0.25 T. It took ~ 3 days to complete the entire map. Although I carried out several conductance maps either by moving to another scan-area or by varying the magnetic field, I always observed stretched vortices.

One may ask whether or not the STM has some drift problems, but our STM did not have any problem in taking atomically-resolved conductance maps with high energy resolution previously, which typically requires several-day long measurements. Therefore, the STM drift problem was ruled out. A second possibility is the interaction between a STM tip and vortices such that a tip may drag vortices

while scanning. I used commercial tungsten tips for the measurements. If that is the case, the degree of vortices being stretched in Fig. 5.1a should be more severe than that in Fig. 5.1b, because the scan-speed in the former case was much faster than that in the latter case. Therefore, the cause due to the interaction between a tip and vortices was ruled out too. The big difference between two measurements in Fig. 5.1 was the measurement times. The measurement of a) took ~ 30 minutes to complete, while that in b) required three days. Therefore two different shapes of vortices imply that vortices were moving due to some driving forces, although I did not intend to drive the motion.
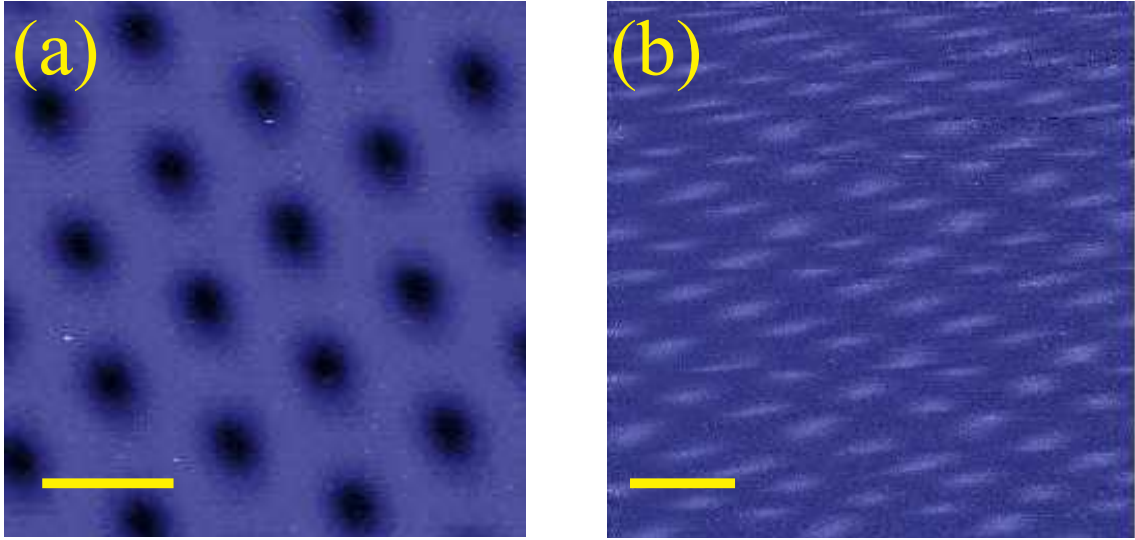
Figure 5.1: **Evidence of moving vortices. a)** A triangular vortex lattice appears in the LDOS at $E_F = 1$ meV in an area of 400×400 nm^2 in 0.25 T at ≈ 2 K. This was measured at a fixed bias voltage of $V = 1$ mV by adding a small *ac* voltage $\Delta V_{mod} = 0.24$ mV to the bias voltage. It took ~ 30 minutes to complete. **b)** Stretched vortices were observed in the LDOS at $E_F = -0.5$ meV in an area of 500×500 nm^2 in 0.25 T at 4.2 K. It was extracted from a conductance map of $-5 \leq E_F \leq +5$ meV with a energy resolution of 0.5 meV/pt, using a tunneling condition of $I = 0.1$ nA, $V = 5$ mV. The total acquisition time of completion of the map over this area was ~ 3 days. The scale bars in **a)** and **b)** correspond 100 nm.

5.3 Imperfection of Superconducting Magnet & Moving Vortex Model

It turned out that the magnetic field stored in our commercial superconducting magnet decayed due to residual resistances at spot-welded joints in the superconducting coils. This manufacturing defect serendipitously led to observations of interesting vortex dynamics in NbSe$_2$. We found that the field decayed from 0.500 to 0.491 T over 21 days and 17 hours, which gave us the average decay rate $\Delta B/\Delta t \approx -4.2$ nT/s (≈ -0.36 mT/day). This measurement was possible because the magnet control unit (consisting of Model 420 and Model 4Q05100PS of American Magnetics, Inc.) is capable of matching a target field to the field stored in the magnet if they mismatch when turning on the heat switch. By using a series inductor-resistor ($L - R$) circuit as a model (Fig. 5.2a), the expressions of the magnetic field and its corresponding current become

$$B(t) \quad = \quad B_0 e^{-t/\tau} \tag{5.1}$$

$$I(t) \quad = \quad I_0 e^{-t/\tau} \;, \tag{5.2}$$

$$\text{where} \quad \tau = L/R \;. \tag{5.3}$$

With the initial and final conditions of magnetic fields, and the inductance of

the superconducting magnet of

$$B(0) = 0.500 \text{ T} \tag{5.4}$$

$$B(21 \text{ d } 17 \text{ h}) = 0.491 \text{ T} \tag{5.5}$$

$$L = 12.4 \text{ H}, \tag{5.6}$$

the decay time constant and the resistance become

$$\tau \approx 3.7 \text{ years} \tag{5.7}$$

$$R = L/\tau \tag{5.8}$$

$$\approx 0.1 \ \mu\Omega . \tag{5.9}$$

This decay will cause the triangular vortex lattice (VL) to expand (Fig. 5.2b), satisfying the relation of $a(B) = \left(2/\sqrt{3}\right)^{1/2} (\Phi_0/B)^{1/2}$ (a, lattice constant and $\Phi_0 = 2.068 \times 10^{-15}$ Tm^2, the flux quantum) [34]. By using the continuity relation of the vortex density and flow of vortices, one can calculate the speed of vortex motion,

$$v_{\text{theory}} = \frac{1}{2} \cdot \frac{r}{B} \cdot \left| \frac{dB}{dt} \right| \tag{5.10}$$

$$= \frac{1}{2} \cdot \frac{r}{\tau} \tag{5.11}$$

$$= \frac{1}{2} \cdot \frac{r \cdot R}{L} \tag{5.12}$$

at a distance r away from the center of the sample. Therefore one expects to observe

motion of the VL at a speed of ~ 4 pm/s at a distance $r = 1$ mm, which is the order of magnitude of the motion I observed. This motion is slow enough compared to the scanning-speed of our STM. However it requires long measurement to resolve the motion.
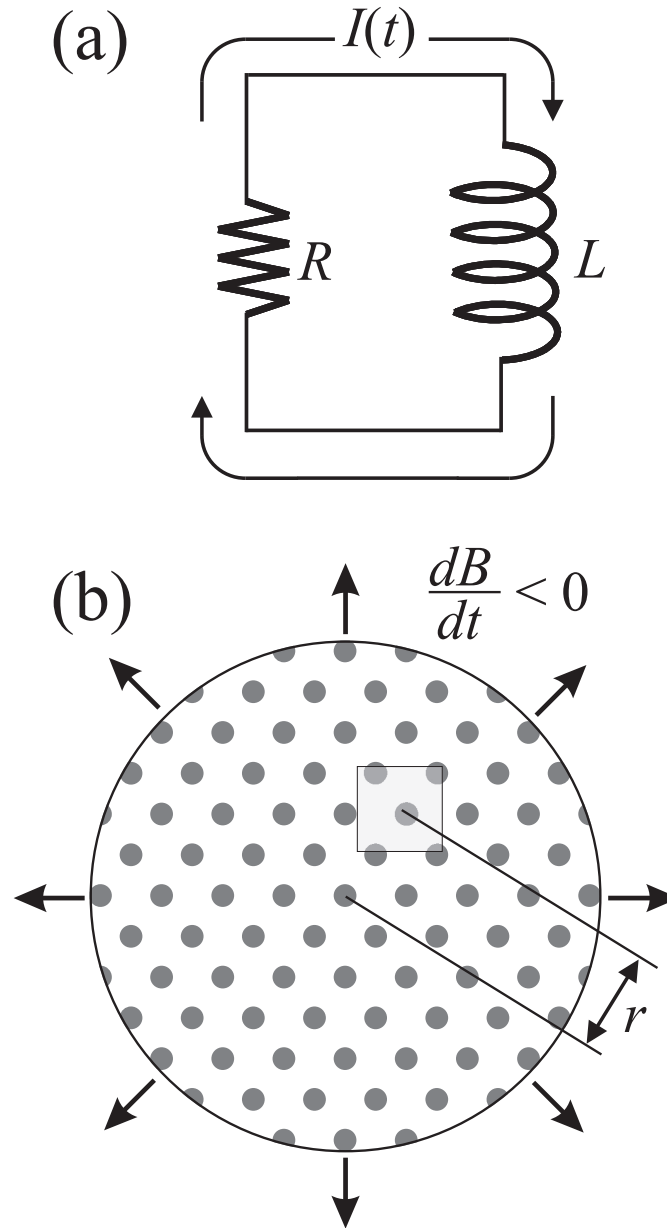
Figure 5.2: **Model of driving source and vortex motion. a)** $L - R$ circuit corresponding to a field-decaying magnet due to non-zero R. $L = 12.4$ H, $R \approx 0.1$ $\mu\Omega$, and $\tau = L/R \approx 4$ years (see text for the detail). **b)** Vortex motion model subject to the decay of a magnetic field. As a field B decays, vortices leave the sample. Observation within a field of view (rectangular area) is made at a distance r away from the center of the sample. The size of the field of view, vortices, and r are drawn for illustration, not to scale.

5.4 Experimental Procedure

Since the estimated motion was extremely small, I carried out measurements with some special care. I waited several hours after a magnetic field was raised to 0.5 T before taking the measurement. All electronics (such as liquid helium level meter, temperature controller, *etc.*) other than the STM controller were turned off during the measurement. The measurement continued over 17 days. There were two interruptions during this measurement. The first was for backing up the recorded data, and the second, for refilling the liquid helium dewar. After refilling the dewar, I took the advantage of the maximum liquid helium holding time of the dewar to produce a 7-day-long data set.

5.4.1 Preparation

I used pristine single crystals of NbSe$_2$ in this study (Berger Helmuth, École Polytechnique Fédérale De Lausanne, Switzerland). The pristine superconductor has less number of pinning centers in the bulk. Therefore the vortex-pinning interactions were minimized in the first place, which allowed us to test the validity of the model (Fig. 5.2). However, because this model does not consider vortex-pinning interactions and the surface barriers at the edge of the sample, non-uniform motion may occur even in a highly pure superconductor, which, indeed, we observed in our experiments.

The STM was operated at liquid helium temperature (4.2 K) throughout the measurement. The sample, roughly a round disk of diameter 5 mm and thickness

0.5 mm, was cleaved under a pressure of $\sim 6 \times 10^{-7}$ mbar in the vacuum chamber, and transferred to the STM in the presence of Earth's magnetic field. When thermal equilibrium was reached, a magnetic field parallel to the c-axis of $NbSe_2$ was raised from 0 to 0.500 T at a rate of 0.100 T/min. The measurement was delayed 4 hours after the initial field was stored in the superconducting magnet, to allow for transient relaxation of materials affecting the magnetic field. I operated the magnet in the persistent current mode during the measurement, subject to the slow decay of the magnetic field discussed previously.

5.4.2 Data Acquisition

Over 17 days, I observed the configuration of vortices in an area of 400×400 nm^2 (128×128 pixels), by recording consecutive spectroscopic images. Due to the difference of the local density of states between superconducting and normal (vortex) regions, individual vortices in the area were visualized in each dI/dV spectroscopic image (gray in Fig. 5.4a), which was achieved by a lock-in method: while scanning over the area with a tunnelling condition of $I = 0.1$ nA and $V = 3$ mV between a STM tip and the sample, I recorded the response of tunnelling current caused by a small ac modulation voltage $V_{mod} = 1$ mV_{rms} with $f = 1973$ Hz. By choosing a scan-speed of 600 nm/s, it took ~ 4 min to complete a scan over the area. I did not observe significant distortions of the VL between adjacent frames, which ensured that this scan-speed was fast enough compared to the motion of the VL. The consecutive spectroscopic images were the basis for our analysis of the

motion of vortices. A vortex core area was determined by choosing the data points that deviated from the standard deviation of dI/dV. Each vortex core consists of ~ 77 pixels, and the center position was determined by the center of masses of the core pixels; each mass corresponds to the scaled value of a pixel. This improved the spatial resolution from 3.125 nm/pixel to 0.356 nm/pixel ($= 3.125/\sqrt{77}$). The time, at which the center of a vortex was detected by the STM tip, was calculated using the scan-speed. The speed v of a vortex in the nth frame was calculated by its displacement and the time difference between $(n-1)^{\text{th}}$ and $(n+1)^{\text{th}}$ frames, which minimized the systematic error caused by the creep of the scanner PZT tube when it moves up and down. To further minimize the systematic errors in locating the centers of vortices, I only considered vortices which had six neighbors within the field of view to avoid the systematic error of locating vortices close to the boundary of the field of view. I also recorded the consecutive topographic images to confirm that no surface modification occurred over 17 days (Fig. 5.3).

Figure 5.3: **Averaged topography of the area the vortex motion was observed.** We observed the motion of vortices in this area of 400×400 nm^2 over 17 days. This image was averaged over 2560 topographies because a topography was not good enough to resolve the features on the surface such as steps and impurities.

5.5 Data Analysis of Vortex Dynamics

5.5.1 Track

In this Thesis, I present and discuss the data taken for the last 7 days because it was the longest observation without any interruption such as refilling the liquid helium dewar. In addition, this data should be least affected by magnetic relaxation of materials used to build the STM, which can affect the motion of vortices.

The gray-scaled image in Fig. 5.4a is the first spectroscopic image in the 7-day data series, showing an almost regular triangular VL with an average lattice constant of about 69 nm. The distorted shapes of vortices, close to the boundaries of the field of view, resulted from Fourier filtering of the raw data. The magnetic field, when the image was taken, can be estimated as 0.496 T using Eq. (5.1). The four time-colored tracks, followed by the vortices 1, 2, 3, and 4 (Fig. 5.4a), indicate how the whole VL moved over days. Vortices 1, 2, 3, and 4 remained within the field of view for 5.1, 5.4, 4.5, and 4.1 days respectively. The tracks look identical, and the distances between the vortices remained almost constant as they moved mostly along one of the principal axes of the VL ($\theta_{VL} = 150°$). Indeed, all vortices moved together while maintaining the ordered structure of the VL. This implies that the strong vortex-vortex interaction overrides the local distortion due to vortex-pinning interaction [48].

While Troyanovski *et al.* [49] reported that the direction of motion of the VL was commensurate with the crystal structure of NbSe$_2$ since the VL and crystal have the same triangular symmetry, we found that the direction of motion was not

commensurate with the atomic lattice of $NbSe_2$.

By overlaying the tracks of all vortices within the field of view, vortices repeatedly visited and stayed longer at certain places than at others, although they arrived there through different paths (color in Fig. 5.4b). By averaging over all images of the VL (2560 in total), I visualized the probability distribution of finding a vortex in space (gray-scaled image in Fig. 5.4b), which manifests the spatial distribution of the minimum in the potential landscape seen by individual vortices. In a constant magnetic field at a fixed temperature, a potential landscape is preserved, which is determined by the vortex-vortex, vortex-pinning interactions, and the influence of the geometry of a sample. However, despite the continuous magnetic field decay in our study, the averaged image shows the specific spatial distribution of a triangular lattice, whose lattice constant matches that of the VL in Fig. 5.4a. This supports the argument that ΔN, the number of vortices which left the sample throughout the measurement was negligible compared to N, the initial number of vortices in the sample. I estimated that $\Delta N/N = \Delta B/B \sim 0.5$ %, where $\Delta B = 4.2$ nT/s $\times$ 7 day ≈ 2.5 mT and $B = 0.496$ T. Indeed, the long observation allowed us to resolve the lattice constant expansion due to the field decay by applying a linear fit to the data of a_θ vs. t (Fig. 5.5 Top), where a_θ is lattice constant along the direction of θ_{VL}. I found that $\Delta a_\theta/\Delta t = (+0.27 \pm 0.03)$ fm/s, which gives $\Delta B/\Delta t = (-4.0 \pm 0.5)$ nT/s, consistent with the field decay we observed.
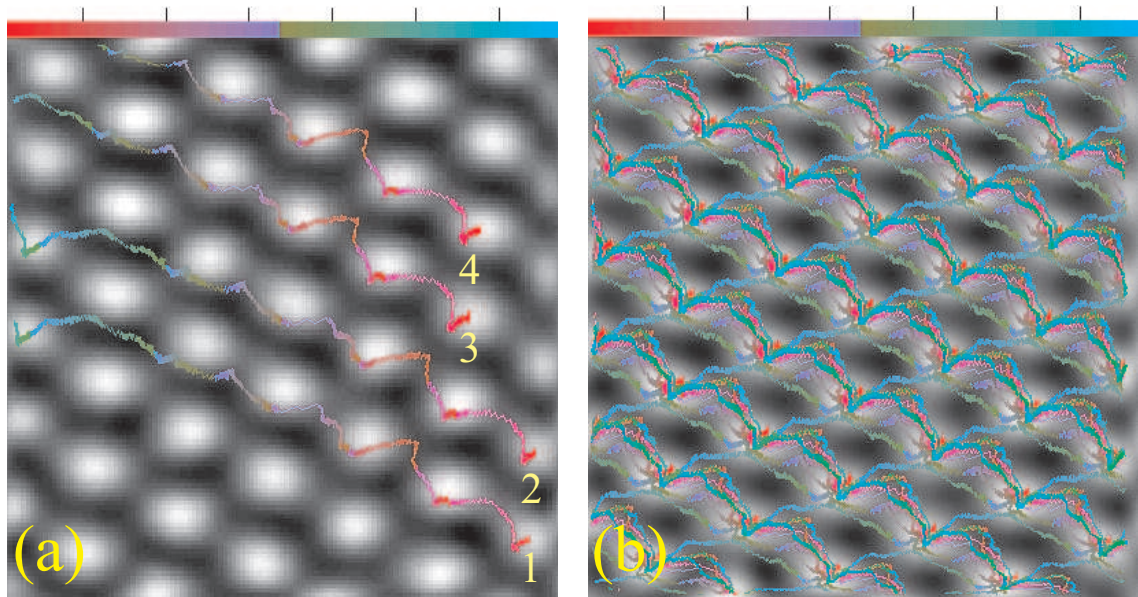
Figure 5.4: **Tracks of vortices in NbSe$_2$. a)** Collective and coherent motion of ordered vortex lattice. The gray-scaled image, the first spectroscopic image of the 7-day observation, shows the configuration of the vortices in an area of 400×400 nm^2 at 0.497 T. Subject to the magnetic field decay, all vortices moved together as the tracks of four vortices (color) indicate. Tracks are color-coded in time. The earliest time starts from red (1st day), and ticks mark every 24 hour on the color bar. **b)** All tracks and the 2560 averaged spectroscopic image over 7 days. Notice that the places, where the vortices more commonly passed by, form a triangular lattice (color).
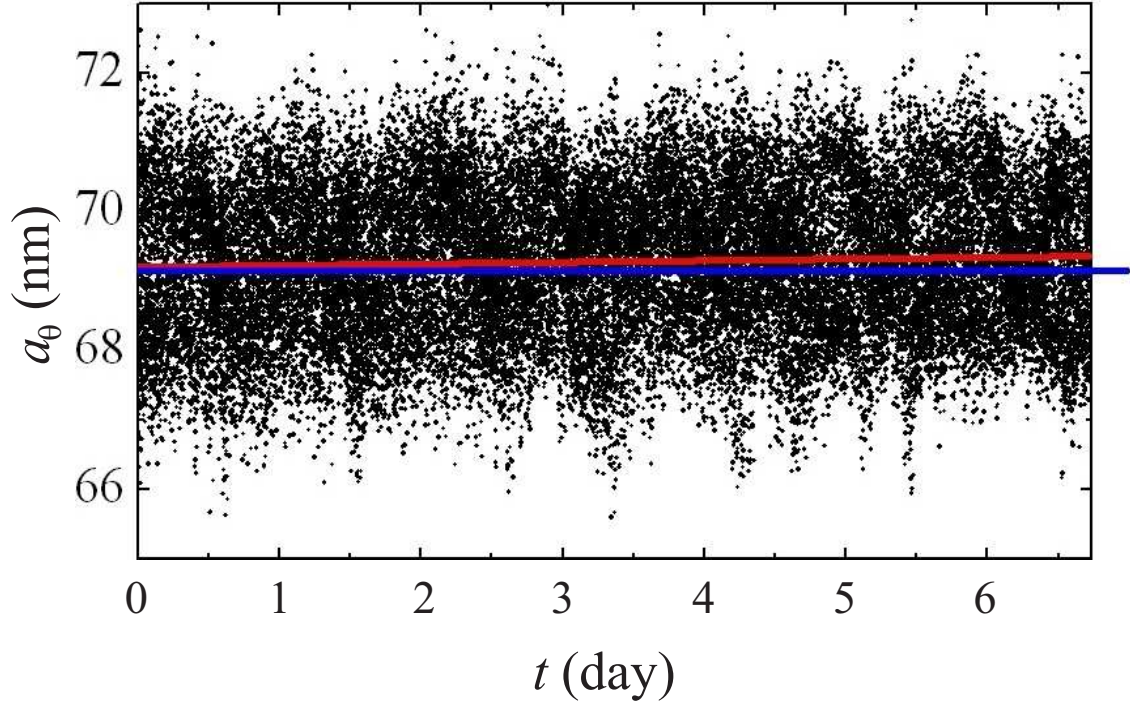
Figure 5.5: **VL expansion due to magnetic field decay.** Lattice constant (a_θ) vs. time (t). I extracted ~ 34000 vortices which have six nearest neighbors from 2560 VL images. I assumed that the six nearest neighbors and the vortex under consideration were detected at the same time. I applied a linear fit (red) to the time series of $a_\theta(t)$ to find the expansion rate of lattice constant. I found that $\Delta a_\theta/\Delta t = (+0.27 \pm 0.03)$ fm/s with the y-intercept of 69.2 nm. A blue line is drawn and extended horizontally at 69.2 nm to clarify $\Delta a_\theta = (+0.16 \pm 0.03)$ nm. By using the data of a_θ, I also found that $\Delta B/\Delta t = (-4.0 \pm 0.5)$ nT/s, comparable to that found by measuring the B directly, $\Delta B/\Delta t \approx -4.2$ nT/s. This field decay rate gives $\Delta B = (-2.3 \pm 0.3)$ mT during the measurement time period.

5.5.2 Speeds vs. Time

Because the VL remained almost rigid during the motion, a single track represents the dynamics of the VL as a whole. This allows us to combine all tracks into a single one by sorting the observed velocities by time and re-integrating the data to form a single track. These procedures led us to the following highly-time-resolved plot of speeds (v, v_{par}, v_{per}) vs. time, where v_{par} and v_{per} are parallel and perpendicular components of v, the speed of the VL, to the direction of θ_{VL} (Fig. 5.6a). For example, the 50 times as fast motion as the averaged one, was clearly resolved in the inset. Contrary to a constant speed predicted by the simple model (Fig. 5.2b), notice that the motion was rather stochastic in time. Nevertheless the magnitudes of the averaged speeds agree well with the prediction of the model; $\langle v \rangle$, $\langle v_{\mathrm{par}} \rangle$, and $\langle v_{\mathrm{per}} \rangle$ are 2.49, 0.95, and 0.13 pm/s respectively. The non-zero motion at $\langle v_{\mathrm{per}} \rangle = 0.13$ pm/s presumably arose from the fact that two directions of the driving force and the θ_{VL} do not necessarily match each other. Indeed, by projecting v to another direction at $\theta = 158°$, the perpendicular motion to θ was further minimized to ~ 2 fm/s from 0.13 pm/s.

I would like to point out that this magnetically driven motion is 3 orders of magnitude slower than the slowest motion without an external force reported by Troyanovski *et al.* [49]. They observed the creep motion of 22 vortices in a pristine NbSe$_2$ at 0.6 T and 4.3 K. In contrast to their observation, we did not observe noticeable creep motion, when a constant magnetic field was maintained via an experimental procedure (see Fig. 5.9 for the details of the procedure and Fig. 5.10

for the stationary vortices at 0.750 T over 2 days in Sec. 5.6). Presumably the difference in observations arise from the following reasons. They waited 20 min after raising a magnetic field from 0 to 0.6 T before taking measurements. In contrast, the 7-day-long data was taken 10 days after the magnetic field was raised to 0.5 T from the Earth field. Even the first measurement among the 17-day-long observation was delayed 4 hours after the field was raised to 0.5 T. We had longer waiting time than Troyanovski *et al.* did before measurements. Our vortex motion was less affected by the magnetic field relaxation right after the initial field was raised. Probably, they observed the motion of vortices affected by this field relaxation in the beginning.

In order to see the influence of earlier magnetic field relaxation, we carried out another experiments. In these measurements, the STM continuously imaged vortices while changing magnetic fields from one value to another. Thus we promptly observed the effect due to early field relaxation. During the change of magnetic field, vortices were not imaged properly because the scan-speed of our STM was slow compared to the motion of vortices. As soon as a magnetic field was set at a target field, the STM clearly resolved individual vortices within a minute or so[1]. This transient motion was $10 - 20$ times faster than the motion after the field relaxed long enough[2]. Typically, within $4 - 8$ min after the target field was set, the speed of vortices became less than 10 pm/s, which is still far slower than the motion Troyanovski *et al.* reported using pristine $NbSe_2$. This implies two possible aspects. One is that pristine $NbSe_2$ between two groups were different. The other

---

[1]This time period corresponds to several line scans out of 128 in total. The completion time per image was about ~ 4 min.

[2]The relaxation typically took about 6 hr.

118

is that there might be unknown driving source involved in their experiment such as decaying magnetic field.
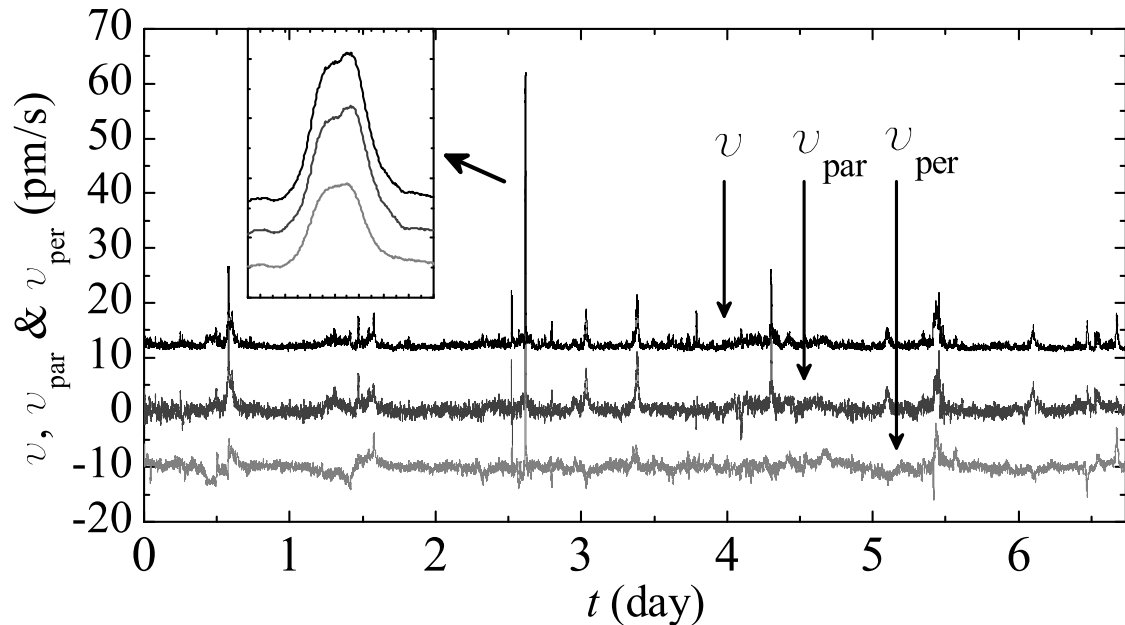
Figure 5.6: **Speeds vs. time.** Speeds (v, v_{par}, and v_{per}) vs. time (t). v_{par} and v_{per} are the decomposed components of the speed v of the VL, parallel and perpendicular to one of principal axes ($\theta_{VL} = 150°$) of the VL. The data of v, v_{par} and, v_{per} were smoothed by averaging over 7 points to reduce noise. v and v_{per} are shifted vertically by ± 10 pm/s respectively for clarity. $\langle v \rangle$, $\langle v_{par} \rangle$, and $\langle v_{per} \rangle$ are 2.49, 0.95, and 0.13 pm/s respectively, where $\langle x \rangle$ denotes the average value of x. Note that $v(t) = \sqrt{v_{par}(t)^2 + v_{per}(t)^2}$. Therefore, $\langle v(t) \rangle^2 > \langle v_{par}(t) \rangle^2 + \langle v_{per}(t) \rangle^2$. No clear temporal periodicity was observed. Inset is the expanded time window over the 25 min., which shows the moment when the fastest motion occurred.

5.5.3 Fourier Analysis of Speeds

Although it is not obvious to find any periodicity in Fig. 5.6 by eye, I found that the temporal periodicity at $f_0 = (1.28 \pm 0.09) \times 10^{-5}$ Hz becomes visible via the Fast Fourier transformations (FFTs) of $v_{\text{par}}(t) - \langle v_{\text{par}} \rangle$ and $v_{\text{per}}(t) - \langle v_{\text{per}} \rangle$ (Fig. 5.7a). The modulations at f_0 are associated with about one-lattice constant movement along θ_{VL} at $\langle v_{\text{par}} \rangle = 0.95$ pm/s. However, the amplitudes at f_0 are comparable to others at higher frequencies, because the random-fashion in which abrupt changes of speeds (Fig. 5.6) appear, and the measurement time of 7 days was not long compared to its corresponding time period, $T_0 = (21.7 \mp 1.5)$ hr. Indeed, I found $1/f$-like broad band noises in both power spectrum of $v_{\text{par}}(t)$ and $v_{\text{per}}(t)$ (Fig. 5.7b).
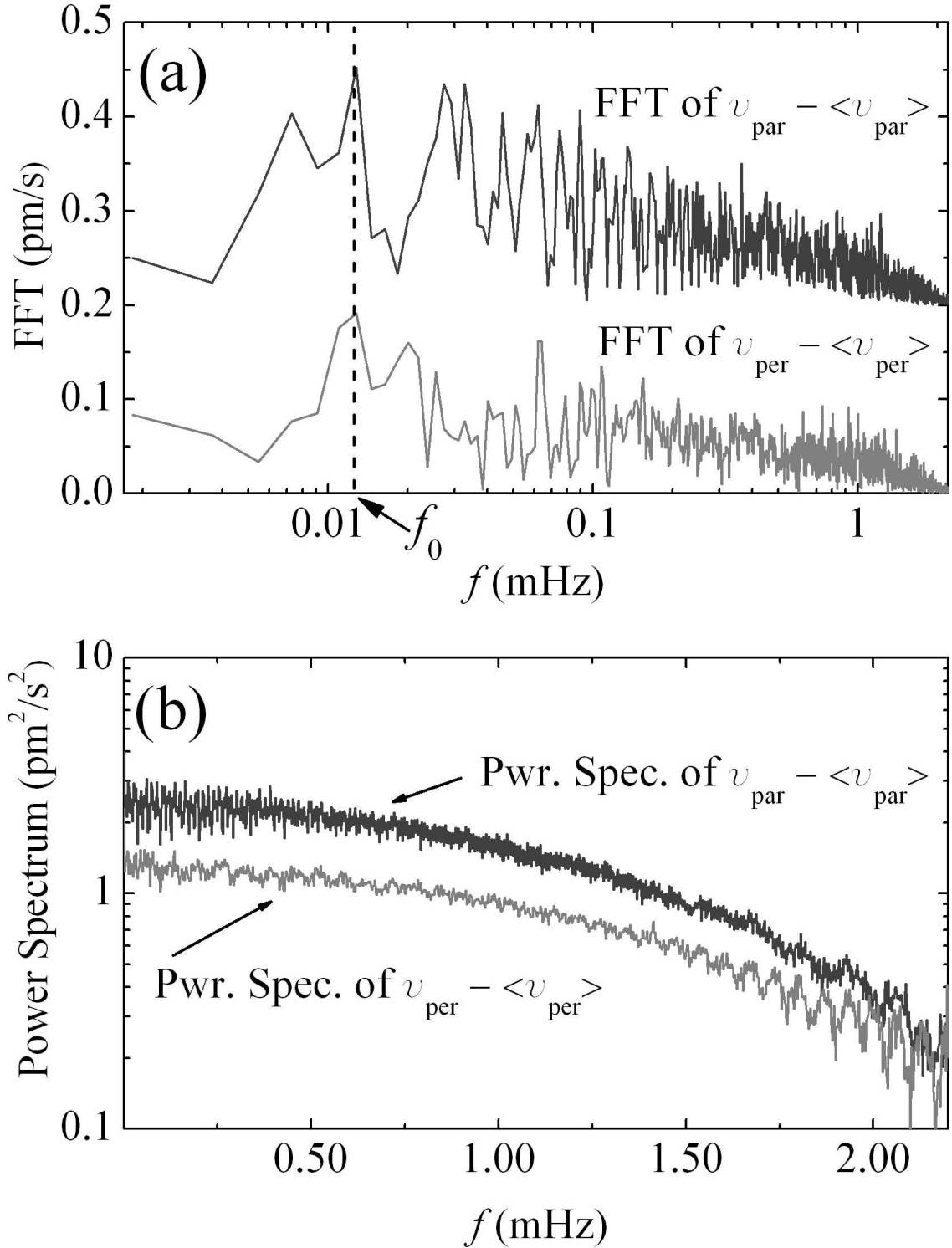
Figure 5.7: **FFTs and Power spectrum of speeds. a)** is the plots of the Fast Fourier transformations (FFTs) of $v_{\mathrm{par}}(t) - \langle v_{\mathrm{par}}\rangle$ and $v_{\mathrm{per}}(t) - \langle v_{\mathrm{per}}\rangle$, and **b)**, their power spectrum respectively. $f_0 = (1.28 \pm 0.09) \times 10^{-5}$ Hz. $T_0 = 1/f_0 = (21.7 \mp 1.5)$ hr. The FFT of $v_{\mathrm{par}}(t) - \langle v_{\mathrm{par}}\rangle$ is sifted up by 0.2 pm/s for clarity.

5.5.4 Speeds vs. Displacement

Introducing the displacements $(X(t), Y(t))$ of the VL, where $X(t) \equiv \int_0^t v_{\text{par}}(t)dt$, and $Y(t) \equiv \int_0^t v_{\text{per}}(t)dt$, I collapsed the multiple tracks of individual vortices (Fig. 5.4b) into one single trace (red-blue in Fig. 5.8). Although the VL moved about one lattice constant every 24 hr along θ_{VL}, its movement also showed one switching event from one row to the next of the VL (see the upward arrow). Along with the displacement, we were able to see the spatial behavior of v_{par} and v_{per} (dark-gray, gray in Fig. 5.8). Notice that the motion of the VL was suppressed when it was close to the minimum of potential landscape (see the magnitudes of v_{par} and v_{per} where arrows point). When the VL was in between two adjacent potential minimum, large changes of both v_{par} and v_{per} occurred.
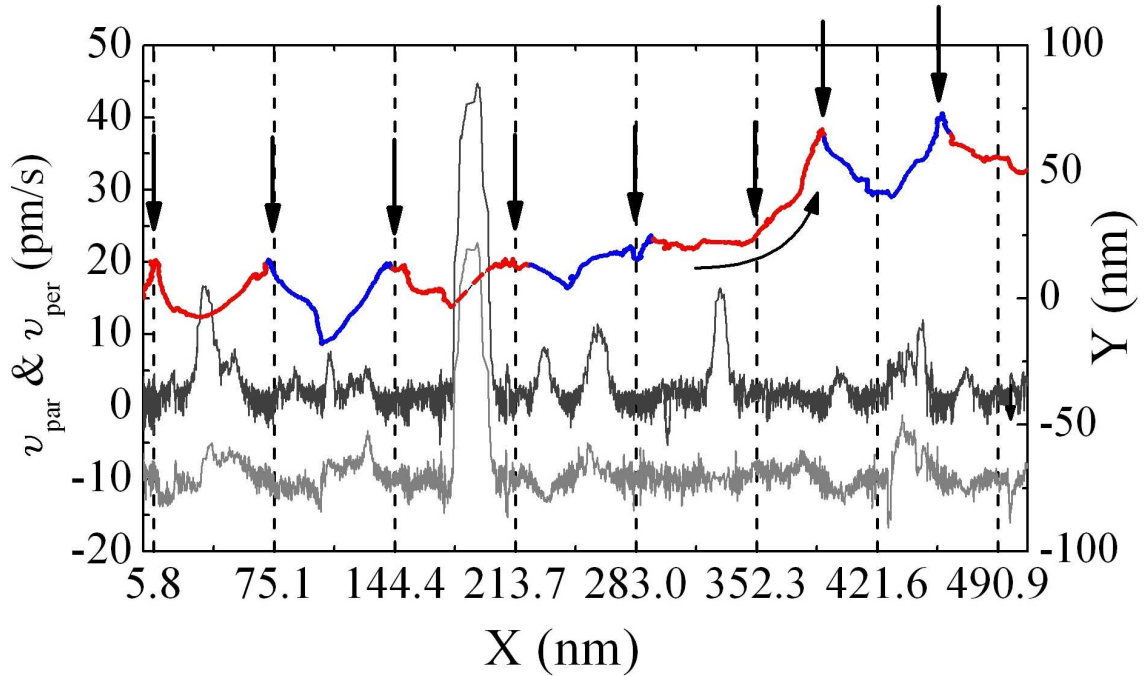
Figure 5.8: **Displacement and speeds (parameterized in** t**).** The displacement $(X(t),\ Y(t))$ of the VL are defined by $X(t) \equiv \int_0^t v_{\mathrm{par}}(t)dt$, and $Y(t) \equiv \int_0^t v_{\mathrm{per}}(t)dt$. The $(X(t),\ Y(t))$ is alternatively color-coded in red-blue for every 24 hour. The arrows indicate when the vortices were close to the minimum of the potential land-scape (Fig. 5.4b). Dotted grid lines are drawn at every 69.3 nm, corresponding to the lattice constant of the VL at 0.496 T. The dark-gray and gray curves are the parametric plots of $(X(t),\ v_{\mathrm{par}}(t))$ and $(X(t),\ v_{\mathrm{per}}(t))$ respectively, where $(X(t),\ v_{\mathrm{per}}(t))$ is shifted vertically by -10 pm/s for clarity.

5.5.5 Why not Uniform Motion?

The most intriguing question is what caused the motion of the VL to be non-uniform, which cannot be explained by using the simple model (Fig. 5.2b in Sec. 5.3). Based on the fact that I used pristine crystals of $NbSe_2$, there are three possible factors to impede the motion. One is the randomly distributed weak pinning centers I discussed in Section 4.6. Second is surface barriers due to the finite size of the sample (Sec. 4.7). Third is step bunch on the surface. These three are unavoidable in sample preparations.

I have shown that the elasticity of the VL together with the random distribution of weak pinning centers breaks the long range order of VL, and introduces a short range order when the pinning strength of a pinning center is weak (Fig. 4.6a in Sec. 4.6). However, using our current STM setup, we did not observe different domains of VLs within a field of view, up to 600×600 nm^2, in a magnetic field, $0.25 - 0.75$ T. Due to strong vortex-vortex interaction and weak pinning in pristine $NbSe_2$, the size of a domain becomes larger than the maximum field of view we used. Interestingly, after further analysis of the 7-day-long data, we found that there occurred local distortions of the VL on the order of ~ 2 nm at one location in the field of view, 400×400 nm^2. Probably, this local distortion was caused by one of weak pinning centers in the bulk. This observation implies that randomly distributed weak pinning centers cause local distortions of VL around each pinning center, and do not impede the entire VL as a whole.

The effects of surface barriers have been well known in macroscopic measure-

ments. Several macroscopic studies experimentally proved that the critical current density as a measure of the pinning strength were significantly influenced by the edges of the samples [50–52]. Paltiel *et al.* [51] found that the transport current was dominant at the edges of a strip of pristine $NbSe_2$, not in bulk. The circulating vortices in a disk (Corbino geometry) of $NbSe_2$ showed the distinct first order phase transition from Bragg glass phase into a disordered phase, in contrast to a strip case, which proved the edge contamination played the key role of the phase transition despite the inhomogeneities of $NbSe_2$ [52]. Shaw *et al.* observed a factor of 2 increase of the depinning currents of 99.5% pure Nb and $In_{0.6}Pb_{0.4}$ by introducing a radial cut, or a radial groove in the Corbino geometry, proving that such structural irregularities significantly enhanced the pinning strength.

Lastly, I always observed many steps running across a cleaved surface of $NbSe_2$ using a optical microscope. In addition, when we carried out computer simulations of 2-dimensional vortex system with steps crossing over a surface as extracting random number of vortices from the sample in random manner[3], we found that the characteristics of the simulated vortex dynamics were similar to that of the vortex dynamics observed in our experiments. This supports that the combination of step bunch (a kind of correlated pinning centers) and surface barriers can explain the non-uniform motions of vortices. However, we do not know which one is more influential on the vortex dynamics than the other. One way of suppressing the effects due to surface barriers is to observe the motions of vortices in a Corbino geometry

---

[3]When vortices exit (enter) a superconductor, they exit (enter) the superconductor in a random manner [53, 54] due to surface barriers.

so that vortices circulate inside the superconductor, which minimize surface barrier effect. In this way, one can discriminate the effects of surface barriers from those of step bunches. Currently, we are planning to carry out more measurements of vortex dynamics together with 2-dimensional vortex dynamics simulations to better understand experimental data.

5.6   How to Stop the Motion

By using different sizes (diameters ≤ 5 mm, thicknesses ≤ 0.5 mm) of pristine $NbSe_2$ with initial magnetic fields of $\sim 0.25 - 0.75$ T in other measurements subject to the magnetic field decay, I found similar vortex speeds of $\sim 1 - 10$ pm/s, consistent with the prediction from the model (in Fig. 5.2). But it is an intriguing question whether the field decay of $\sim$ nT/s was the main cause of the motion of the VL or something else also contributed.

To prevent the magnetic field $B(I_0)$ stored in our magnet from decaying, we used the following procedure described in Fig. 5.9 (Douglas Osheroff, Private communication, 2006); First, while the heat switch is turned on (R_{on} becomes ~ 20 Ω), a current I_0 flows through L because R becomes effectively open ($\tau_{on} = L/R_{on} = 12.4$ H/20 $\Omega \sim 0.5$ s). Second, as soon as the heat switch is turned off to store $B(I_0)$ in the magnet, R_{off} becomes ~ 0.1 $\mu\Omega$, I_0 from the external current source flows through R_{off} instead of L ($\tau_{off} = L/R_{off} = 12.4$ H/0.1 $\mu\Omega \approx 4$ years). Lastly, we continue supplying I_0 from the external current source to the magnet even after the heat switch is off and $B(I_0)$ is stored. Then two currents, one from the external

current source and the other in the magnet, flow in opposite direction with same magnitude I_0 at R_off, which leads to a quite reduced power dissipation at R_off compared to the field decaying case. Using this procedure, we observed the motion of the VL over 2 days in a magnetic field of 0.750 T (Fig. 5.10). We found the average speed of the VL was 0.083 pm/s, which is $1 - 2$ orders of magnitude smaller than those of the moving vortices subject to the field decay. One can clearly see almost stationary vortices in Fig. 5.10 compared to the tracks in Fig. 5.4. Finally, we confirmed that the motion of the VL was caused mainly by the magnetic field decay of $\sim$ nT/s, not by a transport current, thermal activation, the relaxation of material after sudden change of magnetic fields, *etc.*
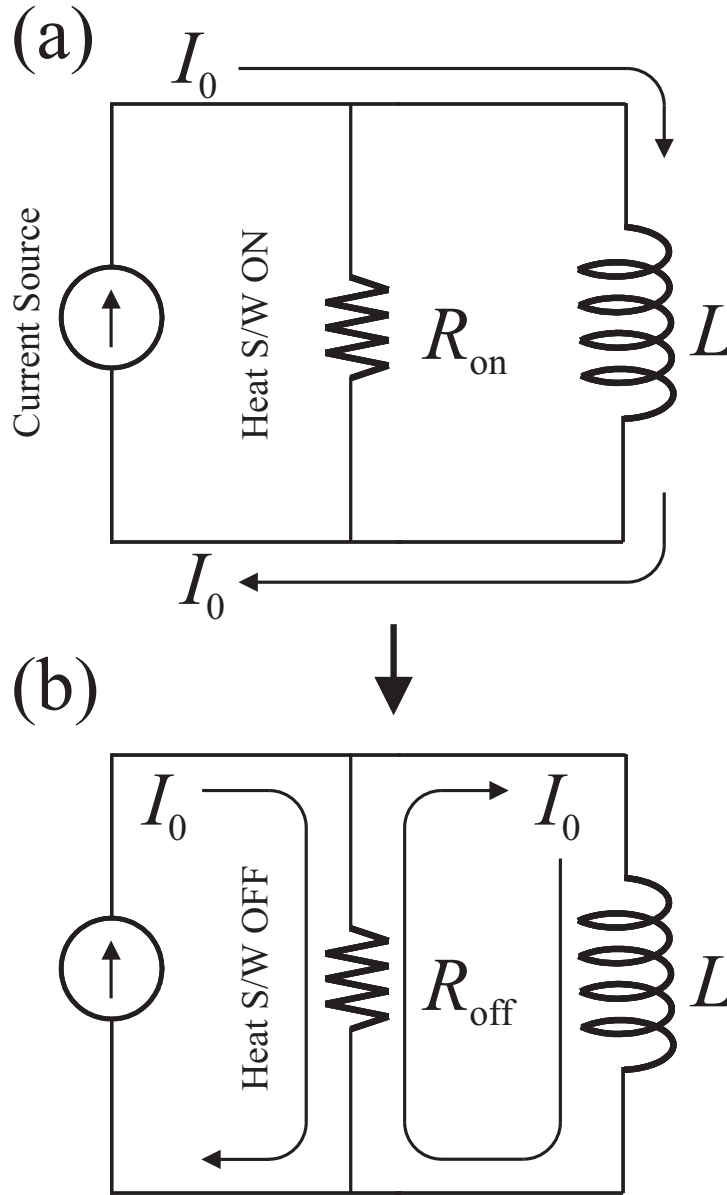
Figure 5.9: **Experimental scheme to maintain a constant magnetic field in a field-decaying superconducting magnet.** See text for detail.
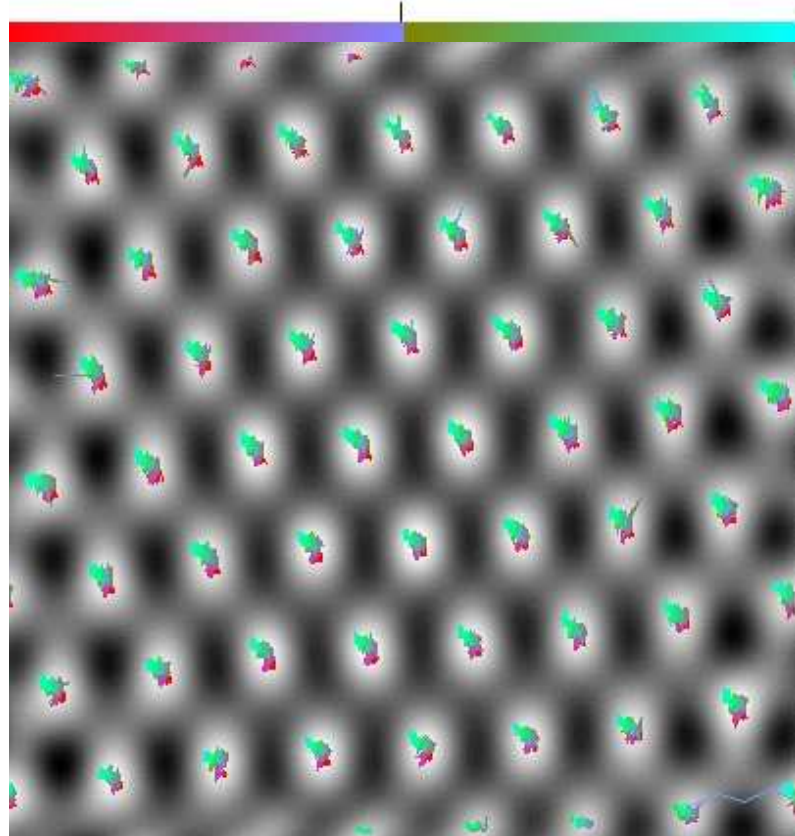
Figure 5.10: **Stationary vortices.** Tracks of vortices when the scheme in Fig. 5.9 was employed. After a field 0.75 T was stored, we observed almost stationary vortices in an area of 400×400 nm^2 for two days. The tunnelling was achieved using $I = 0.1$ nA and $V = 3$ mV, while scanning over with a scan speed of 551 nm/s.

5.7 Significance of Our Observation

As nanotechnology advances, scientists are trying to understand microscopic phenomena on the nano-meter scale, which connect to corresponding macroscopic observations. Vortex dynamics in superconductivity is one topic to be explored on such length scale. Since the vortices in a type II superconductor were first imaged by using the Bitter technique (ferromagnetic particle decoration) in the 1960s (Ref. 55), various vortex-imaging techniques, including improved Bitter decoraton [56, 57], Lorentz microscopy [58], magneto-optics [59], scanning Hall probe microscopy [60], and STM [49, 61] have been implemented to study the dynamic properties of vortex matter on the μm-scale or even less, complementing the macroscopic methods such as neutron scattering [62], transport [51, 52, 63], and magnetization [64] measurements. However, as the inter-vortex spacing approaches less than 100 nm, when vortices are strongly interacting with one another, most imaging methods fail in resolving individual vortices in such regime, while a STM can still resolve them.

Despite its unbeatable spatial resolution, studies of vortex dynamics by STM have been limited due to several factors. First, a STM usually scans slowly, unless it is designed and built to scan fast [49]. In general, STM is not particularly suitable to study dynamics. Second, it is difficult to implement a driving current source in a STM setup. Third, STM needs a clean surface of the sample to achieve spatial resolution on the nano-meter scale or less. In our STM experiments, by utilizing the extremely slow decay of a magnetic field ($\sim$ nT/s) in the superconducting magnet, the first and second obstacles were solved. The typical scan-speed of our STM was

fast compared to the speed of the VL at $\sim$ pm/s, which we observed. The vortices were driven to move by the induced current as a magnetic field decayed in time $(\nabla \times \overrightarrow{E} = -\partial \overrightarrow{B}/\partial t$, where $\overrightarrow{E}$ is the induced electric field), not by a transport current. The third obstacle was solved by cleaving NbSe$_2$ in high vacuum.

Although future investigation is needed to identify which causes the non-uniform motion of vortices in pristine NbSe$_2$, I demonstrated that even a typical STM can overcome the slow-scan speed by having a slow decay of a magnetic field as a driving source to study vortex dynamics. This method can be used to micro-scopically explore vortex dynamics in STM experiments.

Chapter 6

Summary and Perspective

I built a LT-STM (STM II) and a 4 K probe, which meet low temperature, magnetic field, and UHV needs. During the time period of testing its performance, I investigated thin films of Au(111) (deposited on mica, 150 nm thick), and pristine NbSe$_2$ at low temperatures.

The coarse approach of the home-built LT-STM showed a walking step size of $\sim$ 85 nm/step at 4.2 K (Table 1.1) when a voltage of 250 V was applied to the six stacks of PZT. This step size is about 1/3 of the z scan range of the PZT tube scanner, which was optimized together with the z scan range of the PZT tube scanner. If the walking step size is larger than the z scan range, the tip is likely to crash into the surface of a sample when the coarse approach to the surface is in progress. On the other hand, if the step size is too small, the approach time takes too long.

The LT-STM showed high lateral spatial resolution at LT, by which I achieved atomically resolved topography of two materials. At 4.2 K, the XYZ ranges shows 1.0×1.0 μm^2 and 270 nm when the voltage varies from -220 to $+220$ V ($\delta V_x, \delta V_y, \delta V_z = 440$ V). Since each high voltage output is controlled by their corresponding 16-bit digital-analog-converters (DACs) of the STM control unit, one can find that the lateral (XY) and vertical (Z) resolutions are 0.15 Å/bit (= 1.0 μm/($2^{16} - 1$) bit)

and 0.04 Å/bit ($= 270$ nm$/(2^{16}-1)$ bit), respectively, without considering the noise in the high voltage amplifiers. The topographies of Au(111) (Fig. 2.2b) and NbSe$_2$ (Fig. 3.3) showed that the lateral resolution of the STM was sufficient to resolve individual atoms. However, the z-resolution showed ~ 0.1 Å due to high voltage amplifier noise. For example, the corrugations of herringbone reconstruction[1] of Au(111) were not sufficiently resolved in the height image in topography (Fig. 2.2a). This z-resolution can be improved either by replacing the present PZT tube scanner (0.5 in long, 0.02 in thick, $\varnothing$ 0.210 in) with a shorter (or thicker) one (Eq. 1.22) or by implementing a voltage divider[2] between a DAC converter and the high voltage amplifier input. The drift of the STM due to creep of the PZT tube scanner appeared to be ~ 2 nm/day at 4.2 K, based on two topographies before and after the conductance map of Au(111) in the area of 38×38 nm^2 over two days (Fig. 2.6). This can be further reduced by continuous scanning over the same area for a long time before taking a measurement. Indeed, we successfully took atomically resolved conductance maps of NbSe$_2$[3] after allowing the PZT tube scanner to relax enough via continuous scanning over several hours before the real measurements.

The implemented *in situ* sample exchange mechanism performed reliably from RT to 4.2 K. This sample exchange mechanism allowed us to exchange samples within ≈ 1 hr without disturbing the cold environment. After a new sample was installed to the STM, the surface of the sample was approached within $5-8$ hr via the coarse approach process. The *in situ* tip exchange mechanism was also implemented

---

[1] Typical corrugation of herringbone reconstruction of Au(111) is ~ 2 Å [14].

[2] Simply, a 1-to-N divider will improve the z-resolution by a factor of N.

[3] These data are not shown in this Thesis.

in the STM. This will be tested at low temperatures in the near future.

The 4 K probe with the STM mounted showed a $7-8$ hr cool-down time from RT to 4.2 K without using an exchange gas. The precooling with liquid nitrogen takes ~ 6 hr (from RT to 77 K), and the cooling with liquid helium takes ~ 1.5 hr (from 77 to 4.2 K). During the sample exchange procedure, the temperatures (at the bottom of the STM and on the top of the precooling/electrical stage) rise up to $20-30$ K due to precooling of the new sample at the precooling/electrical stage. The elevated temperatures go back to 4.2 K after ~ 30 min. When the bath space of the dewar is fully filled with liquid helium, the measurement can continue over 7 days with the superconducting magnet in operation. This holding time corresponds to the helium boil-off rate of 0.50 L/hr according to the helium bath volume above the magnet[4]. This long liquid helium holding time allowed us to take a continuous measurement of vortex motion of $NbSe_2$ over 7 days. As for magnetic field performance test of the LT-STM system, a field of ≤ 1 T was applied as of now. However, because The top plate of the vacuum can turned out to be quite magnetic so we could not operate at high magnetic fields. We are currently planning to replace the current probe with a new one for higher magnetic field test.

In Au(111) measurements, I observed the motion of steps at 4.2 K using typical scan parameters of $I = 0.05$ nA and $V = 800$ mV, which is not a common phenomena at this temperature. These surface dynamics were induced by the tip-sample interaction. As steps were moving, irregular patterns of herringbone reconstructions changed in a complex way while continuous scanning over the same area, which im-

---

[4]The liquid helium boil-off rate without the 4 K probe is 0.27 L/hr.

plies that large stress was present in the material in the first place. This stress presumably originated from the lattice mismatch between Au atoms and mica (substrate) and the enhanced thermal expansion difference between two materials at low temperatures. We did not observe step motion in measurements of single crystals (1 mm thick) at the same temperature, using similar scan parameters. This implies that there is a threshold value of thickness below which the tip-induced surface dynamics can occur. Investigations of Au film deposited on various substrates in UHV conditions will allow us to better understand this tip-induced surface dynamics in a quantitative way.

In NbSe$_2$ measurements, I demonstrated that the *in situ* surface modification by changing a bias voltage from $10 - 500$ mV to $2 - 10$ V introduced two additional phases: the $\sqrt{13} \times \sqrt{13}$ CDW-like and amorphous phases. At present, we do not know the origin of formation of these phases. Presumably, the top layers slip from the original position due to bias voltage change. This structural change of layer slipping might have introduced new phases. To better predict this phenomena, theoretical approach such as density functional theory [65] would be useful. This surface modification method can be utilized to experimentally explore the competition between superconductivity and CDW sates [26–30] on the nano-meter scale in STM experiments.

Finally, I showed that the motion of vortices in NbSe$_2$ can be triggered by turning on and off the decay of magnetic field of our superconducting magnet (Fig. 5.2, Fig. 5.9). The slow speed at $\sim$ pm/s and the maintained rigidity (Fig. 5.4) of the VL during the motion over 7 days allowed us to overcome the slow sampling rate of our

STM measurement and generate highly-time resolved data set (Fig. 5.6, Fig. 5.8). This magnetically driven motion at slow speeds demonstrates that the control of magnetic field decay rate can be utilized in typical LT-STM experiments to study slow vortex dynamics on the nano-meter scale. Furthermore, when vortices were moving, the non-uniform motions of moving vortices at $1 - 10$ pm/s in pristine $NbSe_2$ driven by the decay of magnetic field at $\sim$ nT/s revealed the influence of surface barriers or step bunches, which was not reported previously at this speed on this length scale.

Appendix A

Capacitive Motion Sensor

We used the capacitance between the inner conductor (attached to the scanner assembly) and the outer conductor (attached to the base) to measure the size of the walking steps (Fig. A.1). As the scanner travels up (down) by the slip-stick motion of the six stacks of shear PZT plates, the capacitance between the two conductors decreases (increases), because the overlapped area between the outer surface of the inner conductor and the inner surface of the outer one decreases (increases). Therefore the size of a walking step can be measured by the change of the capacitance.

When two electrodes of an area of A are parallel and separated by a distance of d in vacuum, the capacitance is

$$C = \varepsilon_0 \frac{A}{d} \ , \tag{A.1}$$

where $\varepsilon_0 = 8.85 \times 10^{-12}$ F/m. As for two concentric cylinders with diameters of $2r_{\text{out}}$ and $2r_{\text{in}}$ overlapped by a length of l, the area is

$$
\begin{aligned}
A &= 2\pi r_{\text{avg}} \cdot l \\
&= 2\pi r_{\text{avg}} \cdot (l_0 - z) \ ,
\end{aligned}
\tag{A.2}
$$

where

$$2r_{\text{avg}} = \frac{2r_{\text{out}} + 2r_{\text{in}}}{2} \ . \tag{A.3}$$

The gap between two cylinders is

$$d = r_{\text{out}} - r_{\text{in}} \ . \tag{A.4}$$

Therefore the capacitance of two concentric cylinders as a function of z is

$$C(z) = \varepsilon_0 \frac{2\pi r_{\text{avg}} \cdot (l_0 - z)}{d} \ . \tag{A.5}$$

By differentiating Eq. A.5 with respect to z,

$$\frac{dC}{dz} = \varepsilon_0 \frac{2\pi r_{\text{avg}}}{d} \ . \tag{A.6}$$

In addition, the maximum change of the capacitance (when the scanner travels from the bottom to the top),

$$\Delta C_{\text{max}} = \frac{dC}{dz} \times \Delta z_{\text{max}} \ , \tag{A.7}$$

where Δz_{max} is the maximum travel distance of the scanner assembly.

Substituting $2r_{\text{out}} = 0.593$ in, $2r_{\text{in}} = 0.563$ in, and $z_{\text{max}} = 0.160$ in into Eq. A.6 and Eq. A.7,

$$\left| \frac{dC}{dz} \right| = 1.07 \ \text{fF}/\mu\text{m} \tag{A.8}$$

$$\Delta C_{\text{max}} = 4.34 \ \text{pF} \ . \tag{A.9}$$
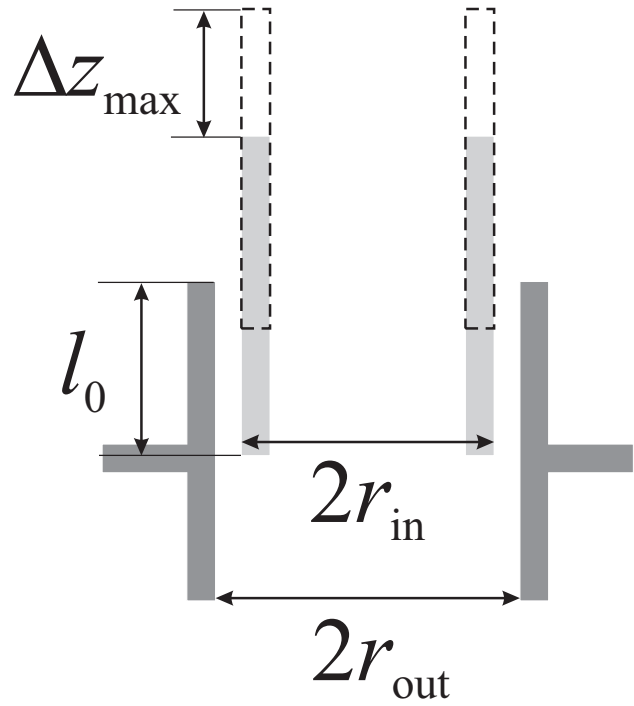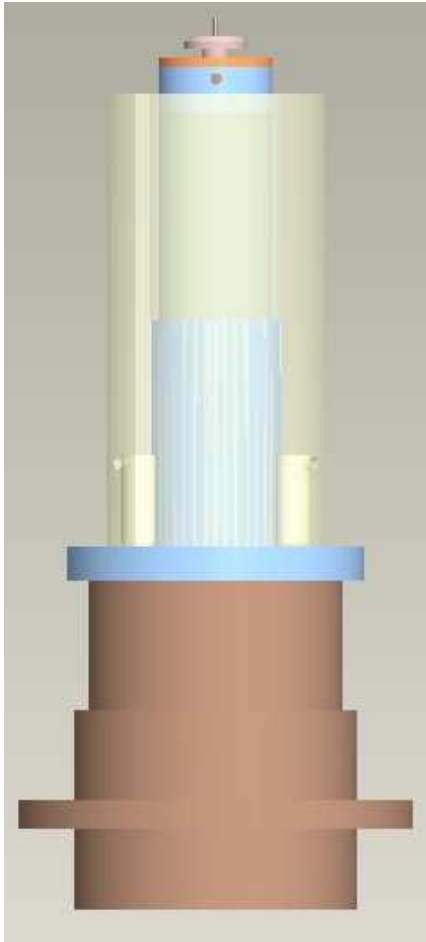
Figure A.1: Capacitance change vs. distance.

Appendix B

Pin Layout at STM & Feedthru Assignment at 4 K Probe

Fig. B.1 shows the electrical wring pin layout seen from the top of the STM. The wires for tip and sample bias are kept away from the rest of electrical components to avoid electrical cross talk. Five wires for the scanner tube PZT are located at sides of the STM body together with a pair of wires for the inner and outer conductors. Seven wires for the six stacks of PZT walkers are located at the front side of the STM. I used miniature coax cables for all wires other than the walker PZT. As for walker PZT stacks, manganin wires were used.

Fig. B.2 shows which feedthru wires access to. Exclusively, a port was dedicated for tip wires to avoid the crosstalk. Notice that the signal from the tip is amplified at room temperature. Therefore long section of wire is very susceptible to any kind of electrical noise and coupling apart from mechanical vibration. To prevent the mechanical vibration of wires, I put pieces of stainless steel shim stocks were put inside tubing. As for the wires of tip, sample, inner/outer conductors, and the scanner tube PZT, I used SMA pin connection feedthrus. For other components, I used military type pin connection feedthrus.

Tip
Bias/Sample

Thermal Link

Scanners
Capacitor Sens.

Walkers
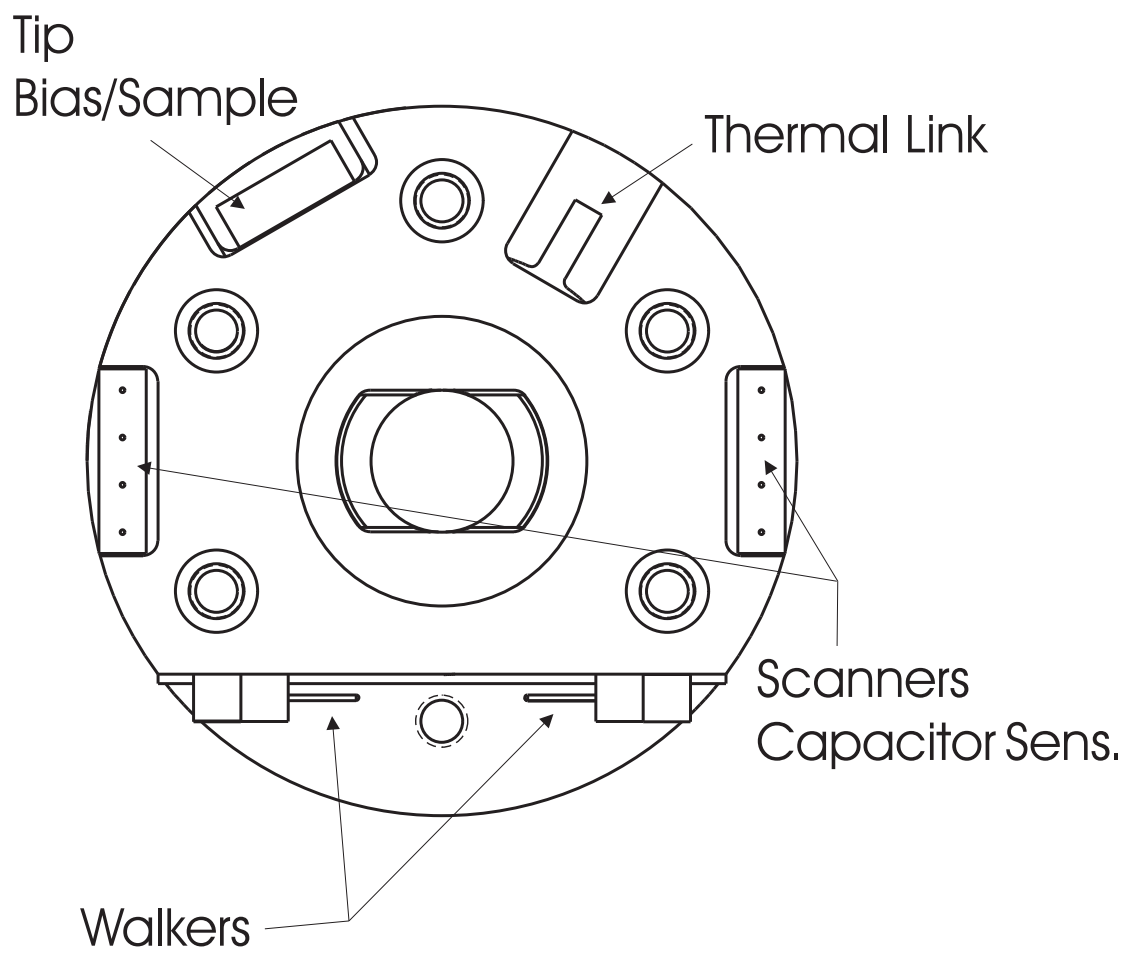
Figure B.1: **Wiring pin layout at the STM.**

Func.	Wire(Type/#)	Con. Type	Min. # Pins
Thermo.	Twisted / 4	19 pins	8
Touch detec.	Single / 1	19pins	1

Func.	Wire(Type/#)	Con. Type	Min. # Pins
Scanner	Coax / 5	SMA	5

Func.	Wire(Type/#)	Con. Type	Min. # Pins
Tip	Coax / 2	SMA	2

Func.	Wire(Type/#)	Con. Type	Min. # Pins
Bias	Coax / 2	SMA	2
Cap. Sens.	Coax / 3	SMA	3

Func.	Wire(Type/#)	Con. Type	Min. # Pins
Walkers	Grouped /	19pins	7
Test PZT	Twisted / 1	19pins	2
Heater	Single / 1	19pins	1
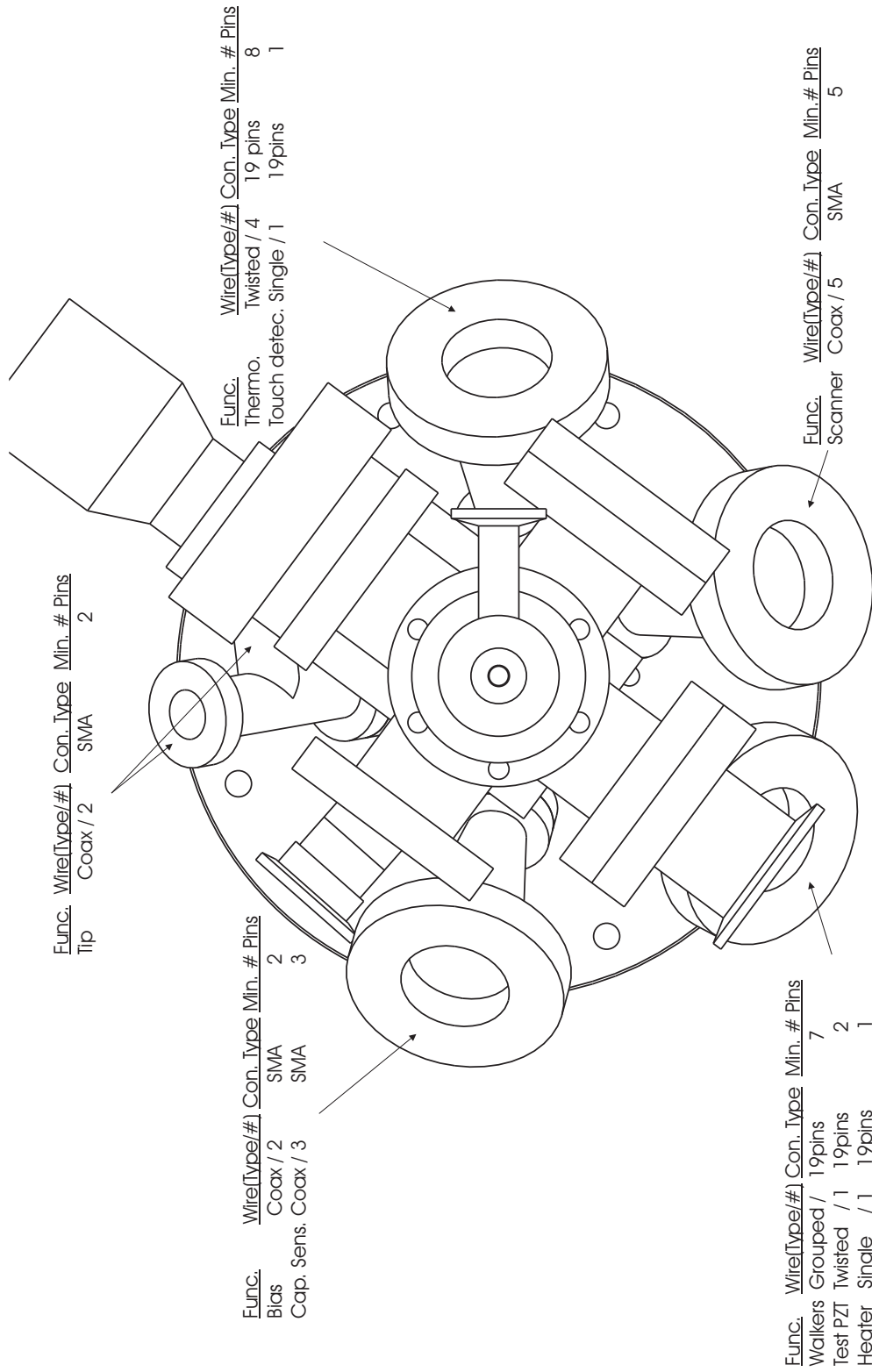
Figure B.2: Electrical feedthru assignment at the 4 K probe (top view).

Appendix C

Relaxation vs. Reconstruction

Consider a semi-infinite crystal. This is achieved by breaking bonds between two crystallographic planes with a certain orientation. Breaking bonds modifies the force acting on atoms [66]. Therefore, the arrangement of atoms on the surface will change compared to that in a infinite crystal. As a result, relaxation or relaxation occur (Fig. C.1).

In relaxation (a), the top layer of surface is displaced rigidly relative to its bulk position. Therefore, the unit cell do not change in this case. However, in case that the displacements of atoms modify the unit cell, this is reconstruction (b).
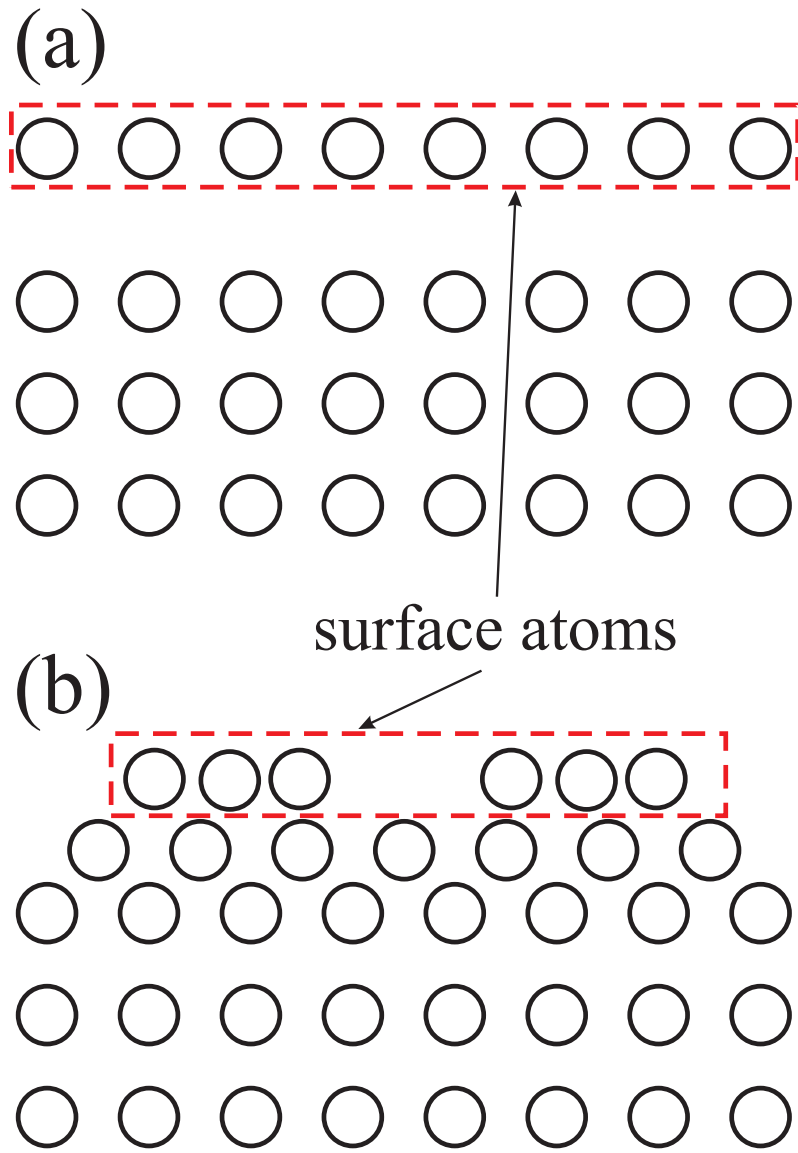
Figure C.1: **Relaxation vs. reconstruction.** Adapted from Ref. 66.

BIBLIOGRAPHY

[1] G. Binnig, H. Rohrer, C. Gerber, and E. Weibel, Phys. Rev. Lett. **50**, 120 (1983).

[2] D. Eigler and E. Schweizer, Nature **344**, 524 (1990).

[3] S. H. Pan et al., Nature **413**, 282 (2001).

[4] S.-W. Hla, J. Vac. Sci. Technol. B **23**, 1351 (2005).

[5] B. C. Stipe, M. A. Rezaei, and W. Ho, Phys. Rev. Lett. **82**, 1724 (1999).

[6] C. J. Chen, *Introduction to Scanning Tunneling Microscopy*, Oxford University Press, New York, 1st edition, 1993.

[7] G. Binning, H. Rohrer, C. Gerber, and E. Weibel, Phys. Rev. Lett. **49**, 57 (1982).

[8] R. Wiesendanger, *Scanning Probe Microscopy and Spectroscopy: Methods and Application*, Cambridge University Press, 1st edition, 1994.

[9] J. Bardeen, Phys. Rev. Lett. **6**, 57 (1961).

[10] S. H. Pan, E. W. Hudson, and J. C. Davis, Rev. Sci. Instrum. **70**, 1459 (1999).

[11] M. Okano et al., J. Vac. Sci. Technol. A **5**, 3313 (1987).

[12] Veeco Metrology Inc., Santa Barbara, CA, USA.

[13] Molecular Imaging Inc., Tempe, AZ, USA.

[14] J. V. Barth, H. Brune, G. Ertl, and R. J. Behm, Phys. Rev. B **42**, 9307 (1990).

[15] C. Wöll, S. Chiang, R. J. Wilson, and P. H. Lippel, Phys. Rev. B **39**, 7988 (1989).

[16] Y. Hasegawa and P. Avouris, Phys. Rev. Lett. **71**, 1071 (1993).

[17] S. D. Kevan and R. H. Gaylord, Phys. Rev. B **36**, 5809 (1987).

[18] M. Böhringer, K. Morgenstern, W.-D. Schneider, and R. Berndt, Surf. Sci. **457**, 37 (2000).

[19] F. Yin, R. Palmer, and Q. Guo, Phys. Rev. B **73**, 073405 (2006).

[20] H. F. Hess, R. B. Robinson, R. C. Dynes, J. M. Valles, and J. V. Waszczak, Phys. Rev. Lett. **62**, 214 (1989).

[21] G. Grüner, Rev. Mod. Phys. **60**, 1129 (1988).

[22] A. A. Abrikosov, Sov. Phys. JETP. **5**, 1174 (1957).

[23] R. E. Peierls, *Quantum Theory of Solids*, Oxford University Press, New York/London, 1955.

[24] B. Koslowski, W. Xu, B. Blackford, and M. H. Jericho, Phys. Rev. B **54**, 11706 (1996).

[25] F. Komori, T. Iwaki, K. Hattori, O. Shiino, and T. Hasegawa, J. Phys. Soc. Jpn. **66**, 298 (1997).

[26] K. Levin, D. L. Mills, and S. L. Cunningham, Phys. Rev. B **10**, 3821 (1974).

[27] K. Levin, S. L. Cunningham, and D. L. Mills, Phys. Rev. B **10**, 3832 (1974).

[28] R. C. Morris, Phys. Rev. Lett. **34**, 1164 (1975).

[29] C. A. Balseiro and L. M. Falicov, Phys. Rev. B **20**, 4457 (1979).

[30] L. L. Daemen and A. W. Overhauser, Phys. Rev. B **40**, 124 (1989).

[31] P. Le Doussal and T. Giamarchi, Phys. Rev. B **57**, 11356 (1998).

[32] T. Klein et al., Nature **413**, 404 (2001).

[33] T. Giamarchi and S. Bhattacharya, Vortex phases, 2002.

[34] M. Tinkham, *Introduction to Superconductivity*, McGraw-Hill, New York, 2nd edition, 1996.

[35] J. B. Ketterson and S. N. Song, *Superconductivity*, Cambridge University Press, 1999.

[36] E. H. Brandt and U. Essmann, Phys. Stat. Sol. **144**, 13 (1987).

[37] E. H. Brandt, Phys. Rev. Lett. **57**, 1347 (1986).

[38] E. H. Brandt, Phys. Rev. B **34**, 6514 (1986).

[39] T. P. Orlando and K. A. Delin, *Foundations of Applied Superconductivity*, Addison Wesley, New York, reprinted edition, 1991.

[40] J. G. Bednorz and K. A. Müller, Z. Physik, B **64**, 189 (1986).

[41] A. I. Larkin and Y. N. Ovchinnikov, J. Low Temp. Phys. **34**, 409 (1979).

[42] J. D. Livingston, in *International Conference on the Science of Superconductivity*, Hamilton, New York, USA, 1963, Colgate University.

[43] C. P. Bean and J. D. Livingston, Phys. Rev. Lett. **12**, 14 (1964).

[44] M. Benkraouda and J. R. Clem, Phys. Rev. B **53**, 5716 (1996).

[45] J. R. Clem, J. Appl. Phys. **50**, 3518 (1979).

[46] A. A. Elistratov, D. Y. Vodolazov, I. L. Maksimov, and J. R. Clem, Phys. Rev. B **66**, 220506 (2002).

[47] H. F. Hess, R. B. Robinson, and J. V. Waszczak, Phys. Rev. Lett. **64**, 2711 (1990).

[48] G. Karapetrov, J. Fedor, M. Iavarone, D. Rosenmann, and W. K. Kwok, Phys. Rev. Lett. **95**, 167002 (2005).

[49] A. M. Troyanovski, J. Aarts, and P. H. Kes, Nature **399**, 665 (1999).

[50] M. P. Shaw and P. R. Solomon, Phys. Rev. **164**, 535 (1967).

[51] Y. Paltiel et al., Phys. Rev. B **58**, R14763 (1998).

[52] Y. Paltiel et al., Phys. Rev. Lett. **85**, 3712 (2000).

[53] S. Field, J. Witt, F. Nori, and X. Ling, Phys. Rev. Lett. **74**, 1206 (1995).

[54] E. Altshuler and T. H. Johansen, Rev. Mod. Phys. **76**, 471 (2004).

[55] U. Essmanna and H. Träuble, Phys. Lett. A **24**, 526 (1967).

[56] F. Pardo et al., Phys. Rev. Lett. **79**, 1369 (1997).

[57] F. Pardo, F. de la Cruz, P. L. Gammel, E. Bucher, and D. J. Bishop, Nature **396**, 348 (1998).

[58] K. Harada et al., Nature **360**, 51 (1992).

[59] P. E. Goa et al., Supercond. Sci. Technol. **14**, 729 (2001).

[60] A. Grigorenko, S. Bending, T. Tamegai, S. Ooi, and M. Henini, Nature **414**, 728 (2001).

[61] A. M. Troyanovski, M. van Hecke, N. Saha, J. Aarts, and P. H. Kes, Phys. Rev. Lett. **89**, 147006 (2002).

[62] U. Yaron et al., Phys. Rev. Lett. **73**, 2748 (1994).

[63] Y. Paltiel et al., Nature **403**, 398 (2000).

[64] S. S. Banerjee et al., Appl. Phys. Lett. **74**, 126 (1999).

[65] P. Hohenberg and W. Kohn, Phys. Rev. **136**, B864 (1964).

[66] S. Gauthier and C. Joachim, editors, *Scanning Probe Microscopy: Beyond the Images*, Les éditions de physique, 1992.